Electrophysiological Characterization of the human Two-Pore Channel 2

Andy K M Lam

Department of Pharmacology

University of Oxford

A thesis submitted for the degree of DPhil in Pharmacology

Trinity term 2015

Publications

Lam AK & Galione A (2015) Title to be confirmed, consisting of material from Chapter 3 (manuscript in preparation)

Lam AK & Galione A (2015) Extracellular H^+-activated Na^+-selective ion conduction through plasma membrane-targeted human TPC2 (manuscript in preparation)

Pitt S, **Lam AK**, Rietdorf K, Galione A & Sitsapesan R (2014) TPC1 is a proton permeable endolysosomal channel that is activated by NAADP and cytosolic Ca^{2+}, Sci. Signal., 20 May 2014; Vol. 7, Issue 326, p.ra46. doi:10.1126/scisignal.2004854

Lam AK & Galione A (2013) The endoplasmic reticulum and junctional membrane during calcium signalling, Biochim Biophys Acta. 2013 Nov;1833(11):2542-59. doi: 10.1016/j.bbamcr.2013.06.004

Conference abstracts

Lam AK & Galione A (2015) Equilibrium selectivity of hTPC2 studied using a plasma membrane-targeted hTPC2 and spermine block (abstract, 59th Biophysical meeting)

Lam AK & Galione A (2014) Na^+ selectivity ensures negligible Ca^{2+} leakage and the formation of a defective Ca^{2+} nanodomain at the pore of plasma membrane-targeted HsTPC2 (abstract, 58th Biophysical meeting)

Awards

Clarendon-New College joint scholarship (2011-2014)

Acknowledgement

I would like to thank my supervisor Professor Antony Galione for general support and helpful comments on this thesis; Professor Trevor Powell for guidance on the initial setup and checkup of the electrophysiology rig; Dr Anthony Morgan for introducing me to fluorescence microscopy and general imaging techniques; and Clive Garnham for general laboratory assistance. I would also like to thank my examiners Associate Professor Paolo Tammaro and Professor Colin Taylor for helpful comments and their desire to improve this thesis.

Abstract

The Two-pore channel (TPC1-3) family represents a recently identified class of endolysosomal ion channels. TPCs were originally proposed to be promising candidate channels for NAADP-induced Ca^{2+} release. However, subsequent studies have emerged to propose an alternative view where TPCs may be Na^{+}-selective channels regulated by the lysosome-specific phosphoinositide $PI(3,5)P_2$ or voltage in an isoform-dependent manner. This thesis asks the question of whether pharmacological and ion permeation properties of TPCs, in particular the human TPC2, may satisfy or may be consistent with the requirement of a potential NAADP-sensitive Ca^{2+}-release channel. These fundamental properties of hTPC2 were approached using patch-clamp electrophysiology and confocal fluorescence microscopy, and were analyzed quantitatively to extract relevant physical parameters important to our understanding of their physiological and functional significance.

Chapter 2 presents the basic electrophysiological characterization of hTPC2. It follows a logical way by first determining the ion permeation properties, followed by the investigation of its physical relation with fractional Ca^{2+} current and Ca^{2+} nanodomains to rigorously prove that this Na^{+} selectivity is sufficient to ensure negligible Ca^{2+} leakage both experimentally and theoretically. This follows the logic that matter must not be created nor destroyed so that a Na^{+}-selective channel that poses a physiologically significant energy barrier to Ca^{2+} permeation from one side would not lead to the creation of Ca^{2+} on the other side.

Chapter 3 represents a natural progression from Chapter 2 and is aimed at investigating the underlying mechanisms responsible for the electrophysiological ion selectivity observed. This chapter also follows a logical way by first identifying spermine as a high valence intracellular blocker, its mutual antagonism with different external ionic species that allows the determination of ion-binding affinity, followed by the determination of the concentration dependence of ion conduction to identify possible lower affinity binding. By considering all the above qualities, the outcome is a coherent description and connection of ion binding selectivity, kinetic selectivity and ion binding configuration with the observed electrophysiological selectivity.

Chapter 4 discusses the missing puzzles and how these questions might be addressed.

Content

List of abbreviations

aa	amino acid
a.u.	arbitrary unit
ACh	acetylcholine
ADP	adenosine 5'-diphosphate
-AM	acetoxyl methyl ester
AMP	adenosine 5′-monophosphate
ANG-2	asante natrium green-2
ATP	adenosine 5'-triphosphate
BAPTA	1,2-bis(o-aminophenoxy)ethane-N,N,N',N'-tetraacetic acid
BK_{Ca}	large conductance Ca^{2+}-activated potassium channel
cADPR	cyclic ADP ribose
Ca_V	voltage-gated calcium channel
cAMP	cyclic AMP
CAX	Ca^{2+}/H^+ exchanger
CCK	cholecystokinin
CHAPS	3-[(3-Cholamidopropyl)dimethylammonio]-1-propanesulfonate
CICR	Ca^{2+}-induced Ca^{2+} release
CMV	cytomegalovirus
CNG	cyclic nucleotide-gated
Cyro-EM	cryo electron microscopy
DAG	diacylglycerol
DMEM	Dulbecco's modified Eagle's medium
EC_{50}	concentration at which 50% of maximal activation is observed
EDTA	ethylenediaminetetraacetic acid
EGFR	epidermal growth factor receptor
EGTA	ethylene glycol tetraacetic acid
Epac	exchange protein directly activated by cAMP
ER	endoplasmic reticulum
E_{rev}	reversal potential
FBS	fetal bovine serum
FKBP12.6	FK506-binding protein of 12.6kDa
fps	frame per second
F-V	fluorescence-voltage

GHK	Goldman-Hodgkin-Katz
GPCR	G protein-coupled receptor
GPN	glycyl-L-phenylalanine-beta-naphthylamide
GTP	guanosine 5'-triphosphate
GTPase	GTP hydrolase
HA	haemagglutanin
Hax-1	HCLS1-associated protein X-1
HCLS1	haematopoietic lineage cell-specific protein
HCN	hyperpolarization and cyclic nucleotide-gated
HEK293	human embryonic kidney 293
HEPES	4-(2-hydroxyethyl)-1-piperazineethanesulfonic acid
H_V	voltage-gated proton channel
iGluR	ionotropic glutamate receptor
IBC	IP_3 binding core
IC_{50}	concentration at which 50% maximal inhibition is observed
IP	immunoprecipitation
IP_3	inositol-1,4,5-trisphosphate
ITC	isothermic titration calorimetry
I-V	current-voltage
JNK	c-Jun N-terminal kinase
LRRK2	leucine-rich repeat kinase 2
K_{2P}	two-pore domain potassium channel
KcsA	pH-gated K^+ channel from *Streptomyces lividans*
K_{ir}	inwardly rectifying potassium channel
K_V	voltage-gated potassium channel
KO	knockout
MEF	mouse embryonic fibroblast
MES	2-(N-morpholino)ethanesulfonic acid
$MeSO_3$	methanesulfonate
ML1	mucolipin1
mTOR	mammalian target of rapamycin
NAAD	nicotinic acid adenine dinucleotide
NAADP	nicotinic acid adenine dinucleotide phosphate
NAD	nicotinamide adenine dinucleotide
NADase	NAD nucleosidase
NADP	nicotinamide adenine dinucleotide phosphate

Na_V	voltage-gated sodium channel
Na_VAb	voltage-gated sodium channel from *Arcobacter butzleri*
NCX	Na^+/Ca^{2+} exchanger
NMDA	N-methyl D-aspartate
NMDG	N-methyl D-glucamine
MWC	Monad-Wyman-Changeux
ORAI	store-operated Ca^{2+} channels
PAGE	polyacrylamide gel electrophoresis
PEI	poly(ethylenimine)
P_f	fractional Ca^{2+} current
$PI(3,5)P_2$	phosphoinositide-3,5-bisphosphate
$PI(4,5)P_2$	phosphoinositide-4,5-bisphosphate
PLC	phospholipase C
PM	plasma membrane
PMCA	plasma membrane Ca^{2+}-ATPase
PMT	photomultiplier tube
PPADS	pyridoxalphosphate-6-azophenyl-2',4'-disulfonic acid
P_O	open probability
RMSD	root mean square difference
RT-PCR	reverse transcription-polymerase chain reaction
RTK	receptor tyrosine kinase
RyR	Ryanodine receptor/SR Ca^{2+} release channel
SDS	sodium dodecyl sulphate
S.E.M.	standard error of mean
SERCA	sarcoplasmic/endoplasmic reticulum Ca^{2+}-ATPase
SF	selectivity filter
spm	spermine
SUEH	sea urchin egg homogenate
TM	transmembrane
TPC	two-pore domain channel
TRP	transient receptor potential
TS	transition state
VEGF	vascular endothelial growth factor
VGCC	voltage-gated calcium channel

1 Introduction

1.1 Ca^{2+} signaling

Ca^{2+} is a ubiquitous intracellular signal that regulates a plethora of cellular processes [1]. Resting [Ca^{2+}] in the cytosol is typically kept at ~100nM. Upon stimulation by extracellular signals, Ca^{2+} in the cytosol increases in a time- and space-dependent manner. This increase in cytosolic [Ca^{2+}] triggers a plethora of downstream cellular processes that are eventually manifested as physiological responses such as muscle contraction.

In order to use Ca^{2+} for signal transduction, every compartment in the cell possess protein machinery that either bind or transport Ca^{2+}. Specialized Ca^{2+}-sensing proteins are present in the cytosol, which change conformation upon binding Ca^{2+}, and act as molecular switches to trigger downstream processes [2-5]. To maintain the appropriate gradient for Ca^{2+} to diffuse, the energy-dependent Ca^{2+} pump SERCA on the ER membrane and buffering proteins in the ER lumen serve to concentrate Ca^{2+} in the ER [6, 7]. The plasma membrane also possesses Ca^{2+} extrusion mechanisms including the PMCA Ca^{2+} pump and Na^{+}/Ca^{2+}-exchanger (NCX) [8]. Ca^{2+}-permeable channels in the membrane of ER or SR including the IP_3 receptors and ryanodine receptors [9, 10] and plasma membrane including voltage-gated Ca^{2+} channels (VGCC) [11], ORAI channels [12], and some Ca^{2+}-permeable transient receptor potential (TRP) channels [13] provide pathways for Ca^{2+} to diffuse down its concentration gradient into the cytoplasm (provided that voltage permits). Upon cell stimulation, these so-called Ca^{2+} release channels open, cytosolic Ca^{2+} level increases which then returns to resting level through the action of Ca^{2+} pumps.

Finally, to prevent excessive increase in cytosolic [Ca^{2+}] and to fine-tune the spatiotemporal characteristic of the Ca^{2+} transient, there are also Ca^{2+}-buffering proteins in the cytosol that bind Ca^{2+} but have minimal sensor function [14].

1.2 Ca^{2+}-mobilizing second messengers

Receptor activation at the plasma membrane is signaled to intracellular effectors through the use of small molecules termed second messengers. Several second messenger systems exist to mediate distinct receptor signals but the general working of these systems is homologous. Activation of G protein-coupled receptors (GPCRs) activates trimeric G proteins, which enables the alpha subunit to dissociate and activate second messenger-generating enzymes at the plasma membrane [15]. Receptor tyrosine kinases (RTKs) can also lead to the generation of second messengers by recruiting second messenger-generating enzymes through phosphorylated tyrosine residues in the signaling complex [16]. Membrane-bound messengers can diffuse laterally to activate membrane-bound targets while soluble ones can diffuse into the cytosol to activate their protein targets.

Various soluble second messengers have been identified. cAMP and IP_3 are the most established second messengers as the individual steps that lead to their synthesis and degradation following receptor activation are well-established [17]. Work has also been done on identifying novel molecules that may function as second messengers. These include cADPR and NAADP [18]. Nevertheless, the step-by-step mechanisms of their generation and degradation following receptor activation remain poorly understood despite more than 25 years of research. While cAMP activates protein kinase A and Epac [19], IP_3 activates an ER Ca^{2+}-permeable channel known as the IP_3 receptor channel (IP_3R) and causes a rise in cytosolic Ca^{2+} [10]. cADPR and NAADP may also function as Ca^{2+}-mobilizing messengers although their action is less-well known as their receptor targets are not well-established.

cADPR probably acts in part through the ryanodine receptor channel (RyR) [20] while the putative NAADP-sensitive channel may be located on acidic vesicles such as the endolysosomes rather than the ER [21].

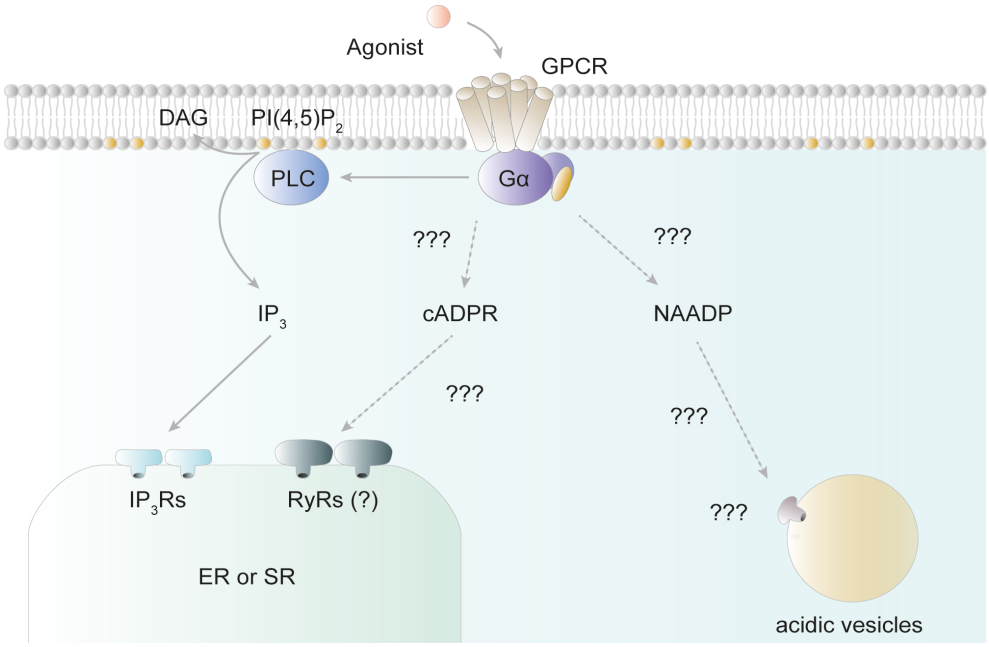

Figure 1.1 Second messenger systems for Ca^{2+}-mobilization

Possible mechanisms activated downstream of GPCR activation that leads to intracellular Ca^{2+} mobilization. IP_3 is generated via a mechanistically established pathway, while the equivalent signal transduction mechanisms for cADPR and NAADP are not well understood and controversial. IP_3 and cADPR target the neutral Ca^{2+} store ER or SR, while NAADP seems to act on acidic Ca^{2+} store that is physically separated from the ER or SR, but may functionally interact with the ER/SR during CICR.

1.3 IP_3

IP_3 was the first Ca^{2+}-mobilizing second messenger identified to mediate agonist-induced Ca^{2+} transients [22]. IP_3 is generated by hydrolysis of the plasma membrane phosphoinositide $PI(4,5)P_2$, which is mediated by the enzyme phospholipase C (PLC) [23]. PLCβ is activated by the G_q alpha subunit following GPCR activation [23] while PLCγ is recruited to the plasma membrane by binding to phosphorylated tyrosine residues upon RTK activation in the receptor protein complex [16]. IP_3 is

rapidly metabolized by either IP_3 3-kinase or inositol polyphosphate 5-phosphatase [24].

The IP_3 receptor (IP_3R1) was first identified from cerebellar fraction and was shown to bind IP_3 and mediate IP_3-induced Ca^{2+} release from microsomes [25-27]. Two isoforms designated IP_3R2 and IP_3R3 were subsequently identified [28]. IP_3Rs are homo- or hetero-meric tetramers of ~1000kDa [29]. Cryo-EM studies have shown that IP_3Rs, like the RyRs, have a 'mushroom' shape consisting of the large cytosolic N-terminal domain and a narrower channel domain [30]. This large cytosolic domain contains the IP_3 binding domain, the so-called suppressor domain, and various binding sites for other modulatory proteins and/or anchors for protein kinases/phosphatases [31]. IP_3Rs function as Ca^{2+}-permeable channels in the ER membrane and have a very high unitary conductance, both of which are consistent with their role in Ca^{2+} release [10].

IP_3Rs are Ca^{2+}-sensitive on the luminal and cytosolic side [10]. There is evidence showing that IP_3 activates IP_3 receptors by modulating this inherent cytosolic Ca^{2+} sensitivity. In the absence of IP_3, cytosolic Ca^{2+} sensitivity is biphasic where activation occurs within 100-500nM and inhibition occurs within 500nM-1uM [10, 32, 33]. IP_3 appears to relieve this inhibition by raising the IC_{50} of this inhibition thereby broadening the activation window [10, 33]. Some have proposed that IP_3 also stimulates cytosolic Ca^{2+} binding as well as relieving Ca^{2+} inhibition [29]. Nonetheless, these mechanisms are likely to allow higher open probability of IP_3Rs when cytosolic IP_3 level increases. This increase in 'leakiness' may allow Ca^{2+} release from distant clusters of IP_3Rs to coalesce into a global Ca^{2+} transient via a processed known as Ca^{2+}-induced Ca^{2+} release (CICR) [10].

How IP_3 binding leads to the activation of the IP_3Rs is not known in detail. IP_3 binding is mediated by the IP_3 binding core (IBC) in the large N-terminal domain

[34]. The affinity of IP_3 binding appears to be regulated by the suppressor domain and is increased when the suppressor domain is truncated [35]. Nevertheless, the suppressor domain, although it inhibits IP_3 binding, seems to be required for channel activation [36]. A mechanism has thus been proposed [29] where IP_3 binding to the IBC brings together the two IBC subdomains. This conformational change may then be propagated through the suppressor domain to open the channel.

1.4 cADPR

cADPR, along with NAADP, was subsequently identified to mobilize Ca^{2+} from Ca^{2+} stores in sea urchin egg homogenate (SUEH) [37, 38]. cADPR can be produced *in vitro* from NAD by ADP-ribosyl cyclases including CD38 (a mammalian homologue) [39, 40]. Endogenous level of cADPR has also been observed to increase upon agonist stimulation [41, 42]. There is some evidence that CD38 may be responsible for cADPR synthesis *in vivo* [43], although the exact enzymatic pathway that leads to its synthesis and degradation is poorly known. Moreover, CD38 is an ectoenzyme, which poses a topological problem for substrate access and regulation [43, 44]. Thus, how it may perform its proposed function is still poorly understood. cADPR antagonists such as 8-NH_2-cADPR and the cell-permeant 8-Br-cADPR have been developed to investigate the potential role of cADPR in various cell types [45].

cADPR activates an IP_3 receptor-independent mechanism probably involving the RyR. Nonetheless, like how it is synthesized *in vivo*, the exact mechanism is also not precisely known. It was initially observed that cADPR might modulate a CICR-like mechanism, which suggested the likely involvement of the RyR [46, 47]. It was later recognized that this may be more complex than a direct action on the RyR and may involve RyR-binding proteins such as FKBP12.6, which was shown to possess a high affinity cADPR binding site [48] and may be dissociated from the RyR thus

potentiating RyR activity upon binding cADPR [49]. However, the RyR proposal as a whole remains controversial due to conflicting reports [20]. Aside from its potential effect on the RyR, cADPR has also been shown to accelerate Ca^{2+} uptake into the SR and ER, probably involving SERCA [50, 51], but see [49, 52]. This may have an impact on Ca^{2+} release by the RyR as luminal Ca^{2+} is a known positive regulator of the RyR [53, 54] and some positive regulators of the RyR, for example caffeine, have been shown to sensitize the RyR to luminal Ca^{2+} [55].

1.5 NAADP

1.5.1 Discovery of NAADP as a Ca^{2+}-mobilizing molecule

NAADP is an emerging putative intracellular second messenger that activates intracellular Ca^{2+} release mechanisms. NAADP was discovered in 1987 [37] as a by-product in alkaline-treated NADP and was found to potently stimulate Ca^{2+} release from SUEH vesicles via a unique mechanism independent of the then emerging second messenger IP_3 and the other NAD metabolite cADPR. Notably, NAADP, cADPR and IP_3 all produce homologous desensitization, a unique mechanism in sea urchin egg, but show no cross-desensitization, indicating that each of these molecules probably acts at their own receptors.

The chemical identity of NAADP was first determined in 1995 [56] and was found to differ from its parent metabolite NADP by a single base-to-acid substitution at the nicotinamide group of NADP. Purified NAADP was shown to have the highest potency amongst the known Ca^{2+}-mobilizing second messengers and its half-maximal concentration was shown to be 30nM in this seminal study. Consistent with the first study, the activity of purified NAADP was also found to be insensitive to inhibitors of the cADPR and IP_3 pathways and shows homologous

desensitization. At the whole-egg level, microinjection of purified NAADP also evokes Ca^{2+} transients, although it is more complex in nature than in SUEH.

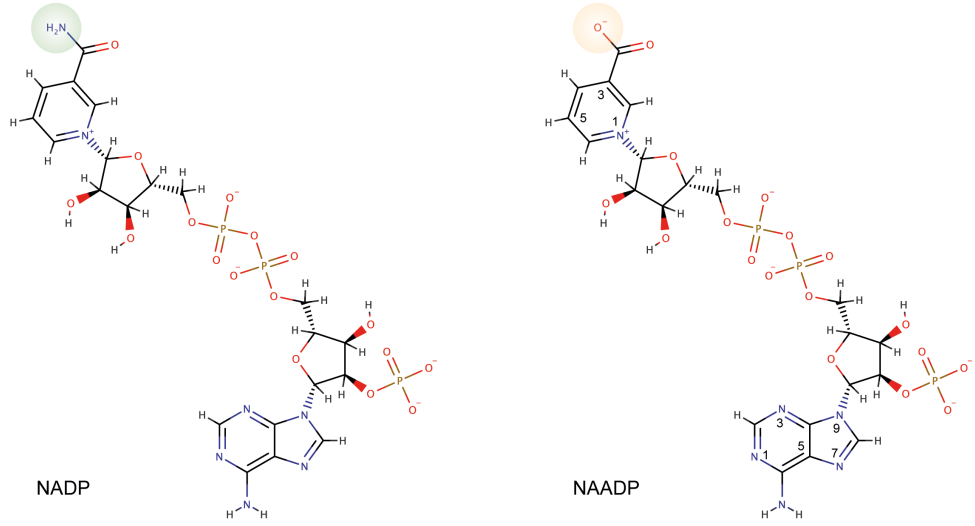

Figure 1.2 Chemical structure of NADP and NAADP

NAADP differs from NADP by a nicotinamide-to-nicotinic acid substitution (highlighted in green and orange circles respectively). Shown is the protonation state at pH 7.4 as predicted from chemicalize.org. Ring numbering of the adenine and nicotinic acid group is also shown for NAADP.

1.5.2 Pharmacology of NAADP binding and function

1.5.2.1 Sea urchin eggs

NAADP binding was first observed in SUEH [57-59] and has an IC_{50} of 0.1-10nM in homologous displacement experiments, comparable to its EC_{50} observed in Ca^{2+} release assays. Notably, in addition to the use-dependent desensitization described earlier, NAADP responses also show desensitization towards pre-activating concentrations of NAADP [57, 60]. Although this high affinity desensitization is relatively well documented, the mechanism is still unclear and no corresponding

binding activity has been observed within the concentration range where this desensitization occurs [57-59].

The pharmacology of the NAADP receptor is poorly understood despite its relatively well-characterized homologous properties. NAADP activity in Ca^{2+} release assays can be inhibited by drugs that antagonize mammalian voltage-gated Ca^{2+} channels [60, 61], purinoreceptor antagonists PPADS, and some well-known low affinity blockers of K^+ channels [61], whereas not much has been reported for drugs that compete with NAADP binding, except for low affinity competition by NADP, cADPR and PPADS [58, 59, 62]. While this list may be useful to distinguish the action of NAADP from that of cADPR and IP_3, the non-specific nature of these drugs makes them less useful chemical probes.

1.5.2.2 Mammalian cells

NAADP binding in mammalian tissues was first observed in brain [63] and has since been observed in various tissues including heart [64], liver [65], pancreas [66], smooth muscle [67, 68], platelets [69], T-lymphocytes [70] and some cultured cell lines [66, 71]. In some but not all systems, mammalian membranes show a two-phase binding profile, which consists of two displacement affinities with varying ratios of the B_{max}'s and IC_{50}'s. The IC_{50} of the higher-affinity displacement varies considerably across different tissues and studies in the range of 5nM to 1μM (but see [68]). In general, this is 100- to 1000-fold lower affinity than NAADP binding observed in SUEH membranes.

The pharmacology of NAADP binding in mammalian cells is similarly poorly characterized but is also displaced at low affinity by NADP and cADPR [64-67], although in some cases the selectivity between NAADP and NADP can be as low as 10-fold [66] to less than 100-fold [64]. It is therefore not known how NAADP-

binding proteins may bind NAADP selectively in the cytoplasm where NADP concentration is typically 1-10μM [72-74], a concentration that is enough to completely displace high affinity NAADP binding in some systems [64-67].

NAADP has been demonstrated in some mammalian systems [71, 75-77] to trigger Ca^{2+} transients, although this has remained dubious in some cases where experiments are not well controlled [78-80]. This is in part due to the considerable difficulty in delivering NAADP into the cytoplasm, although this has not been an issue for the universally accepted Ca^{2+}-mobilizing second messenger IP_3, which is similarly highly charged and require similar delivery methods. Nevertheless, there are cases where the delivery method is verified with IP_3 and/or cADPR, effect of NAADP is not observed in the same cell types [81, 82] reported to possess NAADP-sensitive Ca^{2+} release mechanisms [71, 76, 78].

Where full concentration-response profile is constructed, NAADP activity is generally biphasic, showing low-affinity activation (<1-10μM) and high-affinity inhibition (>10-100μM) [69, 71, 75, 76, 83-88]. The Hill slopes of the EC_{50} and IC_{50} however lack consistency across studies and can vary from ~0.5 to ~2 [69, 71, 75, 76, 83-87, 89, 90], making even simple mechanistic description impossible (see [90] for a non-realistic complete bell-shaped profile within 10-100nM). This bell-shaped profile is different from the behavior of NAADP receptors in sea urchin egg, suggesting intrinsic differences in the mode of action despite that both systems exhibit a Hill slope of ~1 for NAADP binding. Although this low affinity inhibition is relatively well documented, the mechanism is unclear and, like in sea urchin eggs, no corresponding specific binding activity has been observed within the concentration range where this inhibition occurs.

1.5.3 Structure-activity relationship of NAADP

Basic insights into the structure-function relationship of NAADP can be revealed by comparing NAADP with its low affinity analogues. Readers can refer to Figure 1.2 for the structure and numbering of NAADP. The 1000-fold NAADP/NADP selectivity of binding and Ca^{2+} release in SUEH immediately suggests the importance of a negatively charged group in the 3'-position of the pyridine ring. That NAAD does not compete for binding also suggests that a phosphate group on the adenine ribose ring at the 2'-position is an important determinant of NAADP binding.

Chemical substitutions focusing on these moieties and the adenine ring have further revealed the details of the above requirement in SUEH. For example, substitution of the 3'-carboxylic acid of the pyridine ring with other moiety with slightly larger sizes still yields NAADP-like activity with lower affinities, suggesting that the interaction with the NAADP-binding protein can tolerate slightly larger negatively charged group at this position [91, 92]. Changing the position of the 2'-phosphate to 2'-3'-cyclic phosphate to 3'-phosphate gradually decreases affinity to 10- and 100-fold respectively, which reveals that the proximity to the 2'-position on the adenine ribose ring is required for the high affinity of NAADP [91]. The amino group at the 6'-posisiton on the adenine ring is also critical to the high affinity of binding as substitution to a chemically similar hydroxyl group yielded approximately 1000-fold lower affinity [91].

Recently, it has been shown that the 5'-position of the pyridine ring is relatively tolerable to substitution with small chemical groups such as methyl, ethyl and azido groups with only minimal changes in both binding and functional affinities [93]. Taking advantage of this knowledge and its photoreactivity, 5'-azido-NAADP has

subsequently been used as a photoaffinity-labeling probe to aid the search of the elusive NAADP-binding protein (see below).

1.5.4 Pharmacological tools to study NAADP

1.5.4.1 Ned-19

In light of the poor pharmacology of the NAADP receptor, virtual screening, an *in silico* screen that ranks compounds according to chemical, geometrical and electrostatics similarity with NAADP, has recently been performed as a rational and inexpensive approach to identify high affinity and selective compounds aimed at competitively displacing NAADP [94]. Ned-19 was identified as the most effective compound that appeared to antagonize both NAADP activity in SUEH in both Ca^{2+} release and binding assays in the nanomolar range in its *trans* form. Ned-19 is probably a competitive antagonist as it can completely abolish NAADP binding [94]. Its low off rate probably explains why Ned-19 only decreased the efficacy of NAADP while it had no effect on the EC_{50} of NAADP in Ca^{2+} release assays [94]. Nevertheless, a recent study has failed to reproduce the effect of Ned-19 in similar experiments using SUEH [95].

Ned-19 has since been used as a probe for NAADP involvement in mammalian cells. However, Ned-19 binding has only recently been tested in mammalian cells and displays only low affinity displacement of NAADP binding in platelets with an IC_{50} of 100μM [69]. Its antagonist activity has been characterized against physiological stimuli such as glucose and VEGF with functional IC_{50}'s of 10-20μM in beta [94] and endothelial cells [96] respectively. However, it would be interesting to assess its antagonist activity directly against NAADP for comparison. Because Ned-

19 is fluorescent, Ned-19 has also been used in an attempt to label NAADP receptors in live cells [84, 86, 90, 94, 97], although before the demonstration of Ned-19 binding in mammalian preparations. However, this approach has yielded mixed results depending on the individual studies' perspective.

A slightly worrying issue is that the effective concentration of Ned-19 varies considerably across studies [83, 84, 86, 89, 90, 96, 98] and has been reported to be effective at concentrations as low as 100nM [83, 90], ~100- to 1000-fold lower than the IC_{50}'s determined to date. Some have suggested, although without any evidence, that Ned-19 may be transported into the cell via an unknown transporter. An additional confounding issue, as has been reported in some studies (though not investigated systematically), is that Ned-19 itself could trigger spurious Ca^{2+} transients [90, 99], but again the concentration at which Ned-19 reported to induce Ca^{2+} transients is also inconsistent [90, 99].

1.5.4.2 BZ194

BZ194 was developed through chemical optimization based on the low affinity inhibitory effect of nicotinic acid on NAADP-induced Ca^{2+} transients [100]. BZ194 has been characterized directly against NAADP-induced Ca^{2+} transients in T-lymphocytes and SKBR3 cells and has a functional IC_{50} of 1-10μM [95, 100], although so far it has not been tested in binding displacement assay in mammalian cells. As BZ194 has only been used in IC_{50} characterization (titrated against one concentration of the agonist) and not tested in binding experiments, it is unclear how this drug acts. Also, despite its activity in mammalian systems, BZ194 however shows no inhibitory activity on NAADP-induced Ca^{2+} release in SUEH and does not compete for NAADP binding, showing species dependence [95].

1.5.5 NAADP targets acidic Ca^{2+} stores

1.5.5.1 Sea urchin eggs

NAADP was first shown to target a non-ER Ca^{2+} store in SUEH where it induced Ca^{2+} release in the presence of the SERCA inhibitor thapsigargin, a condition that completely abolished cADPR and IP_3-induced Ca^{2+} release [101]. This feature was elegantly demonstrated in whole sea urchin egg where the Ca^{2+} stores targeted by NAADP and cADPR or IP_3 can be physically separated via gentle centrifugation [102]. This NAADP-sensitive region is enriched with lysotracker staining [103], suggesting the involvement of acidic organelles. Indeed, it was subsequently shown that GPN, an osmolytic agent that specifically disrupts lysosomes, specifically abolished NAADP- but not cADPR- or IP_3-induced Ca^{2+} transients in whole sea urchin egg [103]. The specificity of GPN towards cathepsin-rich lysosomes demonstrates for the first time that NAADP-induced Ca^{2+} release in sea urchin eggs is likely of lysosomal origin.

In addition to Ca^{2+} events, it has been discovered that NAADP is also able to induce alkalinization of the lumen of a subpopulation of acidic vesicles in sea urchin eggs [104, 105]. In whole-egg, this effect was completely abolished by BAPTA and was also dampened by EGTA [105], suggesting possible requirement of a highly localized Ca^{2+} increase. This nanometer spatial proximity is therefore also consistent with that the NAADP effector is located on the acidic vesicles themselves. In contrast to the case in sea urchin egg, this alkalinization phenomenon has however not been readily observed in mammalian cells.

1.5.5.2 Mammalian cells

Similar to sea urchin eggs, NAADP mainly targets acidic Ca^{2+} stores in mammalian cells. In the majority of studies, NAADP-induced Ca^{2+} release can be completely abolished by either bafilomycin or nigericin, agents that selectively abolish lysosomal Ca^{2+} loading, or GPN, suggesting a strong lysosomal component [67, 77, 106]. In some studies, NAADP has also been observed to mobilize Ca^{2+} from isolated nuclei and can be abolished by the SERCA inhibitor thapsigargin, suggesting direct involvement of the ER [107, 108]. While the above demonstrate some extreme cases of store utilization, there are also cases where bafilomycin/nigericin/GPN or thapsigargin/ryanodine/heparin alone partially inhibit NAADP responses [89, 98, 108], showing dual store utilization. The interpretation of this latter phenomenon is more difficult as, in addition to the confounding Ca^{2+}-induced Ca^{2+} release (CICR) property of the ER, arguments would generally have to rely on the completeness of inhibition, which to some extent is uncertain in most cases.

1.5.6 Functional interactions between acidic and ER Ca^{2+} stores

Although NAADP and cADPR/IP_3 appear to activate independent receptors in SUEH, NAADP-induced Ca^{2+} transients or fluctuations in whole egg exhibits a considerable ER component, reflecting a complex interplay between the different Ca^{2+} stores. This difference may be attributed to the loss of the organellar architecture normally found in whole egg but is lost in SUEH.

In whole sea urchin egg, NAADP induces a fast Ca^{2+} transient or wave, which can be inhibited by either cADPR or IP_3 antagonists [109]. The rate of Ca^{2+} release and the amplitude of the Ca^{2+} transient appears to be decreased, which is more profound when both antagonists are present at the same time [109]. Therefore, the kinetics of the NAADP Ca^{2+} release mechanism is inherently much slower and the releasable Ca^{2+} of this store is likely to be lower, requiring amplification using ER Ca^{2+} for the

robust Ca^{2+} waves seen normally when NAADP is applied alone. Recently, it has been suggested that this amplification may also involve feed-forward Ca^{2+} signals from the ER to amplify NAADP levels [105]. This idea is intriguing as this suggests that ER Ca^{2+} signals are in turn required to amplify the highly localized Ca^{2+} increase induced by NAADP to produce luminal alkalinization of cortical acidic vesicles in response to sperm entry [105].

At a longer time scale, NAADP is also associated with the tendency of sea urchin egg to produce low amplitude Ca^{2+} fluctuations [110]. This has also been shown to be dependent on the ER Ca^{2+} stores, while the longer-term mechanism seems to in part involve an enhancement of the ER Ca^{2+} load [110].

Similar phenomena have since been observed in mammalian cells where cADPR or IP_3 antagonists or SERCA inhibitors were observed to partially or to great extent inhibit NAADP-induced Ca^{2+} transients or responses [77, 87, 98, 106]. These investigations are generally less detailed than those studied in sea urchin eggs, but similarly suggest either an increase in ER store loading or CICR for an amplified signal, depending on cell types. However, although compelling, direct evidence for a direct CICR-type cross-talk seems to be lacking. For example, one would quantify the difference in activity readouts of the respective organelles in the presence of cellular BAPTA or EGTA and perform quantitative kinetic analysis.

1.5.7 NAADP as an emerging putative intracellular second messenger

NAADP production and acidic Ca^{2+} store usage have been relatively well documented in the literature, which support the notion that NAADP may be a putative second messenger as discussed below. However, the molecular components including enzymes or G protein-like components involved in this

pathway are virtually unknown. Thus, although there is evidence that NAADP may play a role in signal transduction, unlike its counterpart IP_3 whose signal transduction pathway is well established and well accepted, this, in addition to its variable properties and unknown receptors, remains another missing link to concretely including NAADP as a second messenger.

1.5.7.1 Agonist-specific utilization of acidic Ca^{2+} stores

One emerging theme in this area is that agonists known to evoke Ca^{2+} transients seem to be able to utilize different Ca^{2+} stores to different extent. This was first demonstrated in pancreatic acinar cells where GPN selectively abolishes CCK but not ACh responses while thapsigargin abolishes ACh but not CCK responses, suggesting that CCK may be preferentially coupled to acidic Ca^{2+} store usage while ACh primarily uses ER Ca^{2+} stores [77]. Similar observations had been observed with high inhibitory concentration of NAADP, which selectively abolished CCK- but not bombesin-induced Ca^{2+} oscillations [111]. Given the acidic store usage by NAADP and ER store usage by IP_3 [77], this implicates NAADP as a potential second messenger involved in receptor signal transduction. Similar agonist-specific phenomena have since been observed to varying extent in other cell types including pancreatic beta cells [77], neurons [112], astrocytes [84], endothelial cells [113, 114] and smooth muscle cells [67]. Ned-19, despite its own uncertainties, also appears to selectively inhibit agonist responses in an agonist-specific manner [84, 96], providing support to this view.

In addition to the more extreme case of store utilization, there are cases where thapsigargin inhibits the Ca^{2+} transient to great extent, GPN or bafilomycin alone does not completely abolish the Ca^{2+} transient [84, 113, 114], making it difficult to suggest a triggering role for acidic Ca^{2+} stores but may suggest parallel usage of

both acidic and ER Ca^{2+} stores with minimal cross-talk. This appears to be typical for some agonists, which show combined store usage.

1.5.7.2 Agonist-specific production of NAADP

NAADP levels in cells have been measured by either a radioligand binding assay [115] or an enzymatic cycling assay [116], both of which have the potential to detect specifically NAADP but not NADP. The enzymatic cycling assay requires NADase treatment to selectively remove NADP and NAD [116], while in the radioligand binding assay, it was reasoned that through sample dilution it is possible to selectively detect NAADP based on its high affinity [115], although NADase treatment should be helpful.

Like agonist-specific usage of acidic Ca^{2+} stores, it has been shown in many cell types that, in an agonist-specific manner, agonist stimulation can lead to an increase in NAADP level in the sample, although considerable variability is often encountered between samples [41, 83, 84, 112, 117, 118]. Consistent with the above, NAADP production seems to be linked with agonists that are coupled to acidic stores, while not observed in those that target the ER [41, 77, 112]. Most studies demonstrate an NAADP transient upon agonist stimulation, which typically rises to its peak in 30-60s followed by a slower decay, corresponding somewhat to the kinetics of the agonist-induced Ca^{2+} transients [41, 68, 84, 112]. However, although this phenomenon is relatively well documented, few studies have shown the concentration-dependence of NAADP production in response to agonist stimulation, an example of which can be found in [41].

1.5.8 NAADP-binding proteins

Despite more than two decades of effort, the identity of the NAADP-binding protein remains unknown. Interest in identifying the NAADP-binding protein has been re-ignited due to the recently available photo-cross-linkable NAADP analogue ^{32}P-5N$_3$-NAADP, which can be cross-linked to the binding protein upon UV illumination [66, 119]. This probe retains its high binding affinity towards the sea urchin NAADP-binding protein (IC_{50} ~ 18nM in displacement assay) with 100- to 1000-fold selectivity compared to NADP [119], although its affinity towards the mammalian NAADP-binding protein has not been determined in a displacement assay with 5N$_3$-NAADP being the cold ligand [66, 119].

The use of this probe has revealed that the sea urchin and mammalian NAADP-binding protein(s) exhibit considerable biochemical differences. While the sea urchin NAADP-binding protein appears to be tightly membrane-associated (or maybe an integral membrane protein), its mammalian counterpart can be recovered in both the soluble and whole-membrane fractions [66, 70], indicating that it can exist as a soluble protein. Also, by analyzing the selectivity for NAADP against NADP using densitometry on an SDS-PAGE gel, it was found that the sea urchin NAADP-binding protein is ~40 and ~45kD [119], while its mammalian counterpart is ~22-23kD [66, 70]. Its use also confirms the low NAADP/NADP selectivity in some, but not all, mammalian NAADP binding activity reported previously (see above) as this 22-23kD band also has low NAADP/NADP selectivity (8-15-fold) in mouse pancreas and some cell lines including HEK293 cells [66, 70].

Consistent with previous findings that TPC2 overexpression in HEK293 cells only increased binding by ~3-fold [65], these new studies also found no alteration in the B_{max} and IC_{50} of this 22-23kD putative NAADP-binding proteins upon overexpression and knockout of TPC1 or TPC2 individually [66]. The low molecular

weight of this putative NAADP-binding protein also confirms the notion that TPCs (816aa and 752aa respectively) are unlikely to be the NAADP-binding protein. This result also indicates that the presence of TPCs should not alter the EC_{50} of NAADP activity and thus appears to challenge the claim that TPC1 overexpression increases NAADP sensitivity in SKBR3 cells by shifting the NAADP EC_{50} [99].

1.5.9 Ca^{2+} uptake mechanisms of the lysosome

Lysosomes store a considerably amount of Ca^{2+}, with free Ca^{2+} concentration estimated to be ~500μM [120, 121]. This is consistent with the observations where osmotic disruption of lysosomes by GPN leads to cytosolic Ca^{2+} increases that are eventually removed via non-lysosomal pumps [122].

Lysosomal Ca^{2+} uptake depends critically on the sizable pH gradient across the lysosomal membrane. Careful experiments by Christensen et al have shown that, in macrophages, dissipation of lysosomal pH with bafilomycin is correlated with a decrease in lysosomal [Ca^{2+}] and clamping lysosomal pH to >6 with NH_4Cl results in lysosomal Ca^{2+} release into the cytosol [120]. Similar experiments, although without luminal pH calibration and in a different species, have shown that clamping extravesicular Ca^{2+} at increasing concentrations alkalinizes acidic vesicles to a new steady-state pH in SUEH [123]. The reciprocity of these phenomena suggests that Ca^{2+} uptake into the lysosomes may be mediated via a H^+-Ca^{2+} exchange-like mechanism.

Based on these observations, a recent review by Morgan et al have explored a range of potential H^+-Ca^{2+} exchange stoichiometric ratios and showed that an electroneutral exchange ($2H^+$ for $1Ca^{2+}$) is likely to reproduce semi-quantitatively the Ca^{2+} gradient so far observed across the lysosomal membrane [124]. Indeed, H^+-Ca^{2+}

exchange mechanisms of different stoichiometric ratios can also recapitulate the qualitative features of the time-lapse data in pH clamp experiments from Christensen et al. These predictions therefore suggest that a H^+-Ca^{2+} exchange mechanism may be a major determinant of Ca^{2+} uptake in lysosomes. Although H^+-Ca^{2+} exchangers (CAX) have been identified in lower organisms such as yeast, they are absent from higher vertebrates [125, 126]. Thus, the molecular identity of the putative transporter involved in lysosomal Ca^{2+} uptake has yet to be identified to validate these predictions.

1.6 Two-pore channels (TPCs)

Two-pore channels (TPCs) were first cloned in 2000 in an attempt to identify novel voltage-gated ion channels [127]. Sequence analysis has indicated that TPCs likely belong to the tetrameric ion channel superfamily which includes channels with diverse function including K_V, Na_V, Ca_V channels, two-pore domain K^+ channels (K_{2P}), ligand-gated/regulated CNG/HCN channels, K_{Ca} channels, K_{ir} channels and TRP channels [128]. As now revealed by a growing number of experimental structures, common to all channels in this superfamily is a tetrameric pore-forming domain formed by the S5-6 helices (or S1-2 in K_{2P} & K_{ir}). Each pore-forming monomer, except K_{2P} and K_{ir}, is covalently connected to its own membrane-spanning regulatory domain formed by the S1-4 helices. In K_V, Na_V and Ca_V channels, the regulatory domains, primarily the S4 helix, act as voltage sensors that trigger the opening of the pore-forming domain in response to changes in transmembrane voltage, allowing ion conduction. In addition to S1-4, channel function is also regulated by cytosolic domains, which are typically involved in ligand sensing in ligand-gated ion channel and inactivation properties in voltage-gated ion channels.

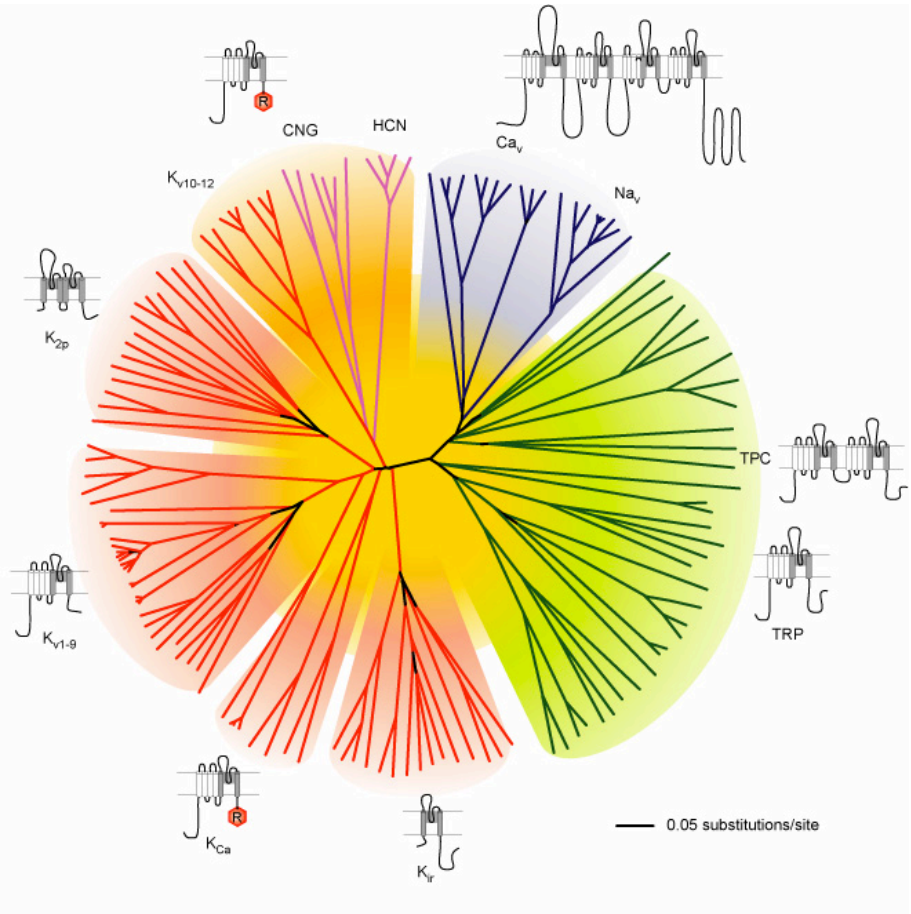

Figure 1.3 The voltage/ligand-gated tetrameric channel superfamily
Adapted from [128]

1.6.1 Isoforms

The TPC family consists of four isoforms (TPC1-3 and plant TPC, see below). TPC genes are represented in most eukaryotes but so far no prokaryotic homologue has been found. Nevertheless, not all three isoforms are present in every genus [65, 129, 130]. In plants, only one TPC isoform is present, which appears to have very different ligand sensitivity and permeation properties [131] compared with vertebrate TPCs (see below). Most vertebrates have all three isoforms but the TPC3

gene exists as a pseudogene in human and closely related rodents and primates and is thus not expressed [65, 129, 130].

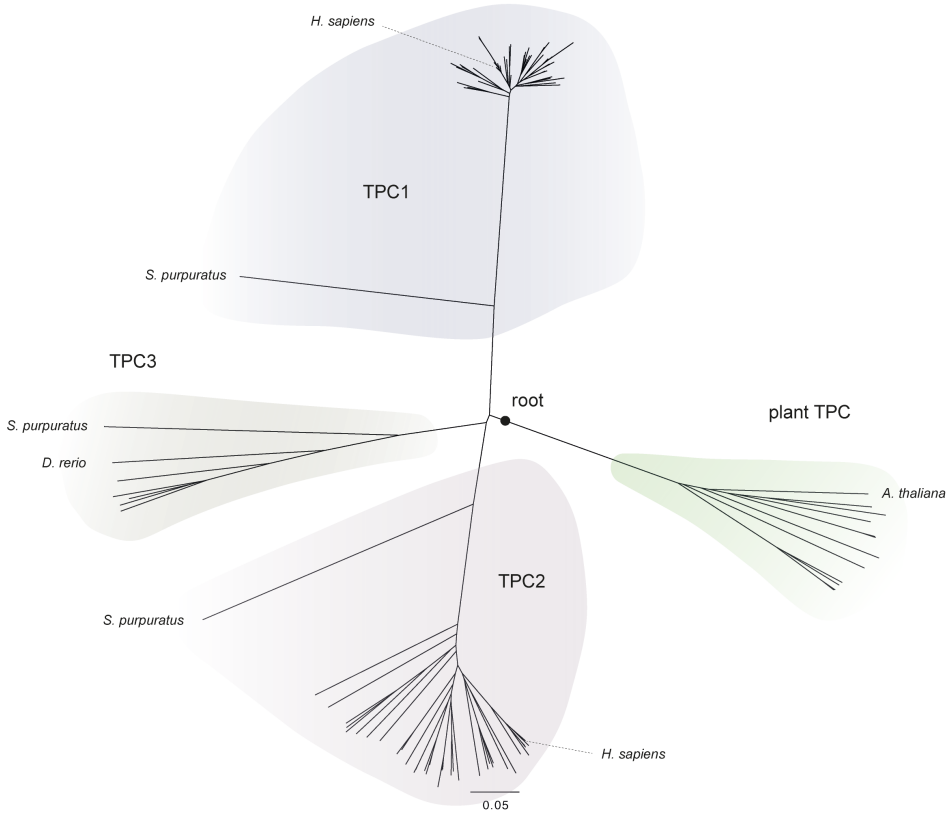

Figure 1.4 Phylogenetic relationship between TPC isoforms

Phylogram of TPCs. The 4 isoforms are highlighted as indicated. The root is shown as black dot, which shows the split between plant and animal TPCs. Model organisms are labeled to show their evolutionary relationships. This tree was generated according to multiple alignment of >100 TPC-like protein sequences (ClustalW) using the Neighbour-Joining algorithm in ClustalX and was displayed using FigTree (http://tree.bio.ed.ac.uk/software/figtree/). Scale bar indicates substitution per residue.

More detailed evolutionary relationship and classification of TPCs can be inferred from phylogenetic tree. We have performed an extensive phylogenetic analysis on >100 TPC-like protein sequences, which shows that the TPC family can be classified into two main groups – TPC1-3 and plant TPC (Figure 1.4). As shown in Figure 1.4, the putative common ancestor of TPCs diverged to become TPC1-3 and plant TPC at an evolutionarily early stage. Indeed, all non-plant TPCs have lost the two Ca^{2+}-

binding EF hand domains commonly found in plant TPCs [131]. The putative common ancestor of TPC1-3 then diverged to form the TPC1 clade and TPC2/3 clade, which were later separated into the TPC2 and TPC3 clades. From this tree, all TPC isoforms from the model organism *S. purpuratus* (sea urchin) appears to be an outgroup compared to most other TPCs in their respective groups (Figure 1.4). This suggests that TPCs from *S. purpuratus* are more distantly related to most other TPCs and might have diverged substantially since a considerably early stage. Other phylogenetic analysis on TPCs can be found in [65, 130].

1.6.2 Expression pattern

TPC1 transcripts appear to have restricted expression pattern in the initial report [127] while appear to be uniformly present in most tissues in [132]. Recent western blot analysis on mouse tissues has shown that TPC1 is expressed most prominently in kidney, liver, lung, spleen and adipose tissues, moderately in heart but are undetectable in brain and pancreas [133]. This expression pattern agrees considerably with the expression pattern in northern blots reported in [127] but seems to disagree with [132]. A splice variant of TPC1, named TPC1B, due to the presence of a downstream intronic alternative promoter, has recently been detected by RT-PCR at the transcript level in tissues including kidney, liver, brain and spleen [133].

TPC2 transcripts have less restricted expression pattern but are most prominently expressed in kidney and liver, considerably low in other tissues, marginally detectable in brain and testis but not in skeletal muscles [65, 132]. Western blot analysis has not been possible due to the lack of specific antibodies and thus the relative expression of TPC2 amongst different tissues has not been systematically investigated at the protein level.

1.6.3 Structure and channel assembly

Before introducing the channel topology, it is useful to examine the terminology used to define the two sides of the membrane. The lysosomal or luminal side is geometrically equivalent to the extracellular space and will be used synonymously with the external side. Because of this geometric equivalence, we will adhere to the conventional polarity of membrane potential. It is perhaps easier to recognize that the cytosolic side of the lysosomal membrane is equivalent to the cytosolic side of the plasma membrane and will be used synonymously with the internal side.

Hydropathy analysis [65, 127] and secondary structure prediction (JPred3 [134]) have indicated the likely existence of 12 transmembrane helices in TPCs, corresponding to two sets of conserved ion transport domains (Figure 1.5). Each ion-transport domain consists of an extra-pore domain (S1-S4) and a pore-forming domain (S5-S6). This 'two-pore' feature is 'intermediate' amongst other channels in this superfamily, which typically have one set (K_V channels) or four sets (Na_V and Ca_V channels) of ion transport domains, and may represent an evolutionary transition (Figure 1.3). Therefore, TPCs likely function as dimers (akin to symmetrical heterotetramers) with a stoichiometric order similar to that of K_{2P} channels, whose crystal structure has been recently determined [135, 136]. Similar to other voltage-gated ion channels, the S4 helices of TPCs have alternate sequence of the positively charged arginine and the potentially positively charged lysine, which may act as a voltage sensor in TPC1 and TPC3 (see below).

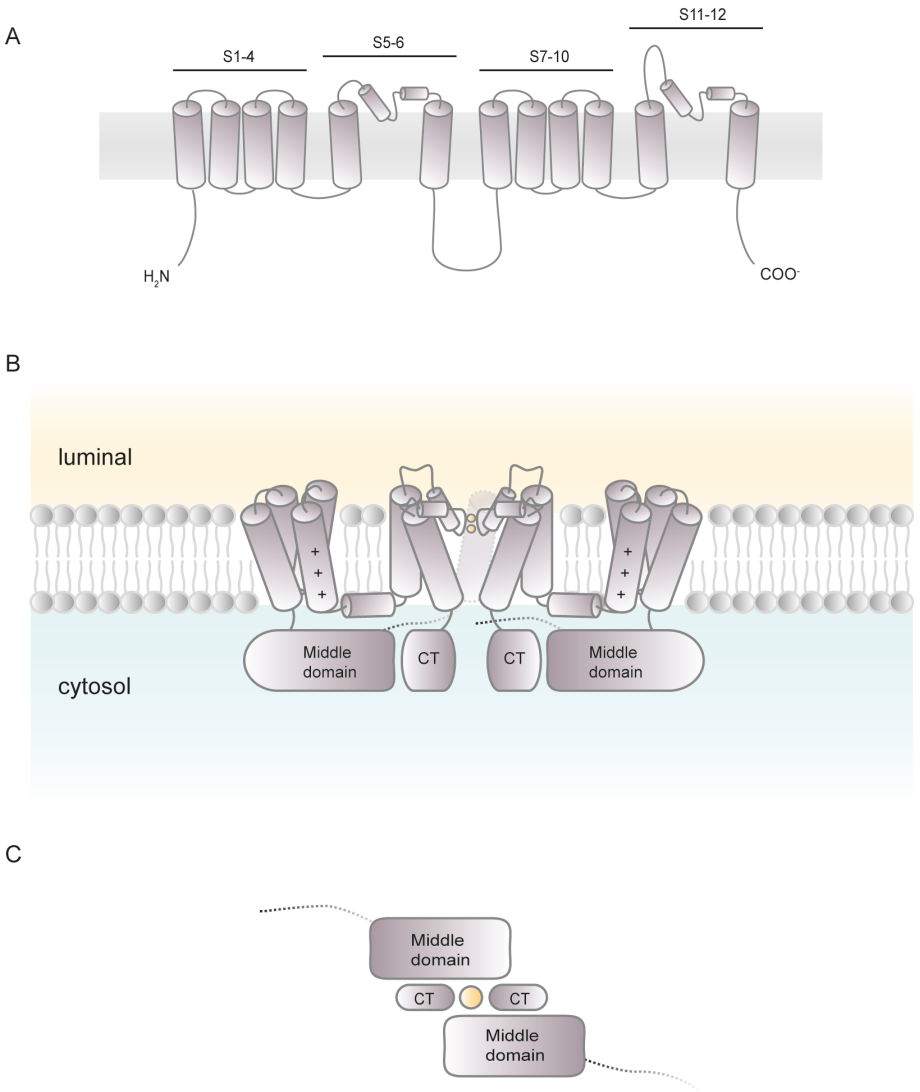

Figure 1.5 Putative structure of TPCs

A. Cartoon of topology inferred from hydropathy analysis and secondary structure prediction.
B. Cartoon of putative quaternary structure depicting how the secondary structure may be organized in space. Shown are the S7-12 of two opposite subunits with the middle and C-terminal domain. This prediction is based on the evolutionary relationship between TPCs and voltage-gated channels and on the available experimental structures of voltage-gated channels. Orange spheres represent putative Na^+ ions in the selectivity filter but the exact configuration and the extent of ion occupancy are unknown. CT, C-terminal domain.
C. Potential organization of the cytosolic domains of TPCs (bottom view). Both the middle domain and the C-terminal domain immediately follow the putative pore helices (S6 and S12 respectively) and may thus be organized as a cytoplasmic tunnel as inferred from the crystal structure of the cytosolic domains of K_{ir} channels [137-140]. Orange sphere depicts a Na^+ ion to show how the potential cytoplasmic tunnel may form.

Similar to other channels in this superfamily, the pore domain (S5-6) of TPC1 has been shown to be capable of assembling into a tetramer [141]. This is consistent with the non-interacting nature of the non-pore helices (S1-4) observed in experimental structures of channels within this superfamily where the pore helices form the main contact points of tetramerization [135, 142-148] (although some channels have contributions from cytosolic domains). A rather surprising observation is that when each S1-6 from the 1st and 2nd ion transport domains are expressed individually, these monomeric units fail to form tetramers [141]. This may suggest that subsequent evolutionarily events might have rendered concatenation of two homologous but non-identical subunits a requirement for proper channel assembly.

The two TPC isoforms (TPC1 and 2) have been shown to co-immunoprecipitate (co-IP) upon overexpression [149]. Interaction between homologous channel subunits however needs to be treated with caution, as co-IP and functional evidence alone or combined do not indicate the formation of a heteromer between TPC1 and TPC2 subunits. Comparison of cross-linking pattern of either TPCs from wild-type and single knockout animals will be required to formally address this question, as has been exemplified elegantly in the interaction between homotrimeric P2X4 and P2X7 channels [150], which were previously thought to heteromerise based on co-IP and functional evidence [151].

1.6.4 Localization

TPCs are localized almost exclusively to the endolysosomal system. Recombinant TPC1 tends to have a wider distribution across functionally distinct endolysosomal compartments and can be found in early, recycling, late endosomes and sometimes

lysosomes [65, 96, 112]. The distribution of recombinant TPC2, however, seems to be more restricted to the lysosomes [65]. The lysosomal distribution of TPC2 is dependent on a conserved di-leucine motif that is contained in its N-terminus and mutation of which leads to plasma membrane localization [152] consistent with that this motif is recognized by the endocytic machinery [153]. The interpretation of the distribution of heterologously expressed TPC3 in common cell lines is more difficult as it is not normally present as functional proteins in human and closely related rodents and primates [65]. For example, recombinant expression of various TPC3 from different species has yielded mixed localization patterns [65, 154, 155]. Therefore, proper analysis of the localization of these channels will require immunocytochemistry experiments on endogenous proteins when specific antibodies are available. Recombinant TPC1 and TPC2 are both heavily glycosylated [65, 83, 132], which may afford protection from the harsh proteolytic environment in the lysosomal lumen.

1.6.5 Permeation and gating properties of vertebrate TPCs

In this section, we will focus mainly on studies examining macroscopic current with channel expression verified with fluorescence. It is perhaps not as confident to discuss in detail studies that characterize novel ion channels using mixed organelle/protein preparations, but these are summarized in Table 1.2 and are discussed where appropriate. On examination of these tables, one can notice that studies reporting macroscopic current of TPCs have yielded consistent results (Table 1.1), while heterogeneous results have been obtained in studies using organelle/bilayer/single channel studies (Table 1.2). More specific discussion on this matter can be found in Chapter 2.

Table 1.1 Permeation and gating properties of TPCs from macroscopic current recordings using traditional patch-clamp with expression verified by fluorescence

Isoform	Species	Configuration	P_X/P_{Na}	Ligand	Voltage	Ref.
TPC1	Human	Whole-lyso	Na^+ (1) >>> K^+ (0.01) ~ Ca^{2+} (0.005)	-	depolarization	[156]
TPC2	Human	Whole-cell/lyso	Na^+ (1) ≥ Li^+ (0.9) >>> Ca^{2+} (0.1) ≥ K^+ ~ Cs^+ (0.03)	$PI(3,5)P_2$	-	[157]
TPC2	Human	Whole-lyso	Na^+ (1) >>> K^+ (~0.01)	$PI(3,5)P_2$	-	[158]
TPC2	Human	Whole-cell/lyso	Na^+ (1) >>> K^+ (~0.1)	$PI(3,5)P_2$	-	[159]
TPC2	Human	Whole-vacuole	Na^+ (1) >>> K^+ (0.05) ~ Ca^{2+} (0.05)	$PI(3,5)P_2$	-	[160]
TPC2	Human	Whole-cell	Na^+ (1) ≥ Li^+ (0.94) >>> Ca^{2+} ~ Ba^{2+} (0.04) ≥ K^+ (0.03) ≥ Cs^+ (0.02) ≥ Mg^{2+} (<0.02)	External H^+	-	This thesis
TPC3	Zebra fish	Whole-cell	Na^+ (1) >>> K^+ ~ Cs^+ (0.01) ~ Ca^{2+} (nd, but gave no current)	-	depolarization	[155]

- Only ligands showing statistical significance or with a full concentration-response profile determined are shown.

Table 1.2 Permeation and gating properties ascribed to TPCs recorded from mixed organelle/protein preparations

Isoform	Species	Configuration	P_X/P_Y or unitary conductance (γ)	Ligand	Voltage	Ref.
TPC1	Human	Bilayer	P_K/P_{Ba} ~ 2.2, γ not applicable (asymmetrical ionic conditions)	NAADP, pH, Ca^{2+}	hyperpolarization	[161]
TPC1	Human	Bilayer	P_X/P_{Na}: H^+ (67) >> K^+ (1.6) ~ Na^+ (1) ≥ Ca^{2+} (0.9) P_X/P_{Ca}: H^+ (503) >>> K^+ (9) > Na^+ (1.1) ≥ Ca^{2+} (1) γ_{Na} ~ 68pS, γ_K ~ 87pS, γ_{Ca} ~ 19pS	NAADP, Ca^{2+}	-	[162]
TPC2	Mouse	Port-a-patch whole-lyso	P_{Ca}/P_K ~ 1000, γ not applicable (macroscopic current)	NAADP	-	[163]
TPC2	Human	Bilayer	P_K/P_{Ca} ~ 0.4, γ_K ~ 300pS, γ_{Ca} ~ 15pS	NAADP	-	[164]
TPC2	Human	Inside-out	P_X/P_Y not determined, γ_{Cs} ~ 128pS, γ_{Ca} ~ 40pS	NAADP	-	[152]
TPC2	Human	Inside-out	P_X/P_Y not determined, γ_{Cs} ~ 12pS	NAADP	-	[165]

- P_X/P_y were converted into P_X/P_{Na} when possible.
- Note in [162], the two sequences of P_X/P_{Na} reported are somewhat non-equivalent.
- Unitary conductance values are not readily comparable since no studies have attempted to determine γ-[ion] relationship. Nevertheless, since these values are obtained typically at 100-200mM [ion], these values in fact do vary considerably across studies.
- Unitary conductance should not be confused with relative permeability. Nevertheless, in the classical case, unitary conductance is a linear function of absolute permeability under symmetrical ionic condition. Therefore, in cases where P_X/P_{Na} hence absolute permeability is low, γ should not be readily detectable.
- Because of the uncertainty in this group of studies, one should be cautious on the interpretation of pore mutants or any mutagenic effects.

1.6.5.1 Classical ion selectivity of TPCs

Whole-cell/lyso patch-clamp studies have shown that recombinant TPCs are Na^+-selective channels with an electrophysiological selectivity sequence quantitatively similar to that of Na_V channels (Table 1.1). On the other hand, studies recording from biochemically isolated proteins or lysosomes have yielded heterogeneous results with no clear permeability sequence identified (Table 1.2). This is difficult to reconcile, but the currents from these studies show no resemblance to the reported macroscopic TPC current. It is possible that additional biochemical procedures and/or different experimental conditions may have contributed to this discrepancy. Nonetheless, in the future, the purity of these preparations will need to be assessed more fully to exclude the possibility that additional channels and/or organelles might have contributed.

Whole-cell/lyso patch-clamp studies demonstrated that, amongst biologically relevant ions, recombinant TPCs are 50-fold and at least 10-fold more selective for Na^+ than K^+ (P_K/P_{Na} = 0.02) and Ca^{2+} (P_{Ca}/P_{Na} = 0.04-0.1) respectively [155-157, 160]. This selectivity has been shown to be both experimentally and theoretically sufficient to ensure negligible leakage of Ca^{2+} through the channel at external [Ca^{2+}] that occurs physiologically (see Chapter 2). Therefore, this property alone suggests that TPCs cannot directly support Ca^{2+} signaling as a Ca^{2+}-release channel, in contrary to what has been assumed previously based on indirect evidence. Importantly, this selectivity sequence appears to be quantitatively reproducible across different expression systems, membrane environment and the presence of either $PI(3,5)P_2$ or external protons as stimuli [155-160] (Table 1.1), suggesting that, like other ion-selective channels within this superfamily (K_V, Na_V and Ca_V channels), selectivity is a robust signature of the channel.

1.6.5.2 Gating regulation of TPCs

1.6.5.2.1 TPC1

Recombinant human TPC1 (hTPC1) has been shown to give rise to non-inactivating voltage-gated currents upon membrane depolarization in voltage-clamp experiments [156]. Activation of hTPC1 is slow and the activation time constant is on the order of 500ms [156], which is ~100-fold slower than Na_V channels, while the deactivation time constant is ~100ms. The lack of inactivation mechanism in hTPC1 is also different from the rapidly inactivating property seen in Na_V channels upon depolarization [156]. Voltage-dependent activation is lost when the arginine residues in S4 are neutralized through conserved mutagenesis, suggesting that, like other voltage-gated ion channels, the S4 also serves as a voltage sensor in hTPC1.

Unlike Na_V channels, the voltage threshold for activation in hTPC1 is very high. At external pH 4.6, V_{50} is approx. +90mV [156], suggesting activation is likely to be minimal at physiological voltages at this pH. However, the V_{50} of hTPC1 can be lowered by alkalinizing the external pH, approaching ~0mV at pH 6.6 [156]. This is likely to have important physiological implications as the wide distribution of hTPC1 in the endolysosomal system (see above) suggests that hTPC1 is likely to experience different pH ranging from 4 to 7 in its lifetime. Given this pH dependency, the contribution of hTPC1 to membrane potential is likely to be highest in early and recycling endosomes where the pH is ~5.5-6.5, and may remain minimally activatable in the lysosome given the ultra high voltage threshold at pH 4.6.

Native TPC1-like Na^+ current has been observed in endolysosomes in various cell types including macrophages, cardiac myocytes and kidney cells with matching V_{50} and voltage sensitivity [156]. Current-clamp experiments have revealed that these

endolysosomes undergo depolarization upon injection of a depolarizing current, which correspond somewhat to the magnitude of the TPC1-like current on the same endolysosome [156]. Indeed, the sustained feature of the depolarization seems to be consistent with the non-inactivating characteristics of voltage gating in both hTPC1 and the native TPC1-like current. These experiments have therefore revealed a novel type of membrane potential regulation in the endolysosomal system, distinct from the pulsatic nature of action potentials at the plasma membrane.

1.6.5.2.2 TPC2

Unlike TPC1 and TPC3 (below), recombinant TPC2 is not gated by voltage, although TPC2 shows increasing inactivation at increasingly hyperpolarizing voltage in voltage-clamp experiments. Recombinant human TPC2 (hTPC2) has been shown to be activated by the lysosome-specific phosphoinositide $PI(3,5)P_2$ from the intracellular side [157-160] with an EC_{50} of 100nM-1μM and a Hill slope of ~1 [157, 160]. From our experiments, hTPC2 activity can also be potentiated by external protons with an EC_{50} of ~pH 6.4 and a Hill slope of ~1 (Ch.2). Although whether these ligands may act on hTPC2 directly and how they exert their co-stimulatory effects are not yet known, they are rational candidates for physiological regulation as both ligands are native to the lysosome where TPC2 resides.

There is a debate on whether TPC2 may be regulated by the putative second messenger NAADP. It has been proposed [65, 98, 112, 132, 166, 167] that TPCs in general may be important to the generation of NAADP-induced Ca^{2+} release, which appeared to show positive correlation, although mild in some cases, with the expression level of these channels. This is intriguing as the pharmacology of NAADP-induced Ca^{2+} release also correlates well with the endolysosomal localization of these channels (see above). However, although this hypothesis is

appealing, the underlying evidence does not indicate whether TPCs may function as a Ca^{2+} release channel, neither do these results suggest direct regulation by NAADP.

So far, traditional patch-clamp studies recording macroscopic currents including ours have failed to detect or detected statistically insignificant activity changes in TPC2 when the previously proposed agonist NAADP is applied [156-160]. Several single-channel studies and studies using isolated lysosomes, however, reported that TPCs in general may be NAADP-sensitive [83, 161-165]. Nonetheless, on closer examination, these single-channel currents generally display different permeation properties than the reported macroscopic current, which, on the other hand, are very consistent (compare Table 1.1 and Table 1.2). It is possible that, in addition to the elusive NAADP-binding protein, other co-factors might be important for NAADP sensitivity for example Rab-GTPase interaction with the N-terminus of TPC2 [168] (see below). How these proteins work together is not clearly known as a study reported that TPC2 lacking the N-terminus remained capable of conferring NAADP-induced Ca^{2+} transients [152].

There is evidence that TPC2 may be regulated by serine/threonine kinases including JNK, p38 and mTOR, which seem to be required for the suppressive effect of cytosolic Mg-ATP [158, 159]. However, with the exception of mTOR, which is in part retained at the periphery of the lysosome via interaction with the lysosomal Rag-GTPase complex [169], how JNK and p38 kinase activity may regulate TPC2 is less clear as these experiments were performed on isolated membranes excised away from the cytoplasm [159]. Whether these observations are due to direct phosphorylation of TPC2 has also yet to be determined although the results so far are consistent with the requirement of kinase activity.

1.6.5.2.3 TPC3

Recombinant *Danio rerio* TPC3 (drTPC3) has been shown also to give rise to non-inactivating voltage-gated currents upon membrane depolarization in voltage-clamp experiments [155]. Activation of drTPC3 is only slightly faster than hTPC1 and both the activation and deactivation time constants are ~250ms [155]. The difference in symmetry of activation and deactivation in hTPC1 and drTPC3 suggests that although both channels appear to have slow kinetics and lack inactivation mechanisms, gating transitions in these channels are probably quite different.

Similar to hTPC1, the voltage threshold of drTPC3 is also high and the V_{50} is approx. +75mV [155], thus activation is also likely to be minimal at physiological voltages at this pH (7.4). Nevertheless, HEK293T cells expressing drTPC3 were able to generate ultra-long action potentials upon the injection of a brief depolarizing current [155], owing to the self-regenerative nature of its voltage gating properties. Therefore, the membrane potential remains stabilized near E_{Na} despite the return to a basal holding current and the membrane only repolarizes upon injection of a large hyperpolarizing current that deactivates drTPC3 [155].

Xenopus laevis TPC3 (xlTPC3) has been suggested to be the channel responsible for the depolarization-induced non-inactivating voltage-gated Na^+ current in *Xenopus* oocyte [155]. This is based primarily on the somewhat similar kinetics and the requirement of induction, although recombinant xlTPC3 has a lower voltage threshold and the kinetics do not match completely [155]. Morpholino knockdown experiments will be needed to confirm this proposal, which have been unsuccessful probably due to the confounding issue where genes with two differing sequences may code for the same protein [155].

1.6.6 Protein-protein interactions with TPCs

Protein-protein interactions play key roles in modulating ion channel functions. Through unbiased approaches such as transcriptome-wide screens and co-immunoprecipitation (co-IP)-mass spectrometry or rational predictions, recent studies have identified a growing list of previously unknown TPC-interacting proteins including Rab GTPases [168], mTOR [158], LRRK2 [170], syntaxin-7 [171], TRPML1 [165] and Hax-1 [172]. Some of these proteins are indeed localized to the endolysosomes and appear to have modulatory effects and may confer ligand sensitivity in some cases.

1.6.6.1 mTORC1

Recent studies have shown that the mTORC1 complex translocates to the lysosomes in response to amino acid repletion [169]. mTOR interaction with TPC2 has been observed in co-IP experiments and found to be required for the suppressive effect of ATP on TPC2, which critically depends on a lysosomal localization of mTORC1 [158]. TPC2 knockout mice have normal lysosomal pH, but appear to have lost the ability to sustain lysosome acidification upon nutrient depletion and thus protein catabolism is impaired [158]. It has been proposed that in the fed state TPC2 activity is partially suppressed and is increased in response to nutrient starvation as mTORC1 translocates to the cytoplasm and cellular ATP level decreases. This may then allow for the lysosomal membrane potential to be dragged towards E_{Na} to oppose the self-abortive hyperpolarizing effect of proton pumping [158]. This model therefore requires that E_{Na} is more positive than E_{proton}, although the Na^+ gradient across the lysosomal membrane is poorly known [124, 157, 173].

1.6.6.2 Rab-GTPases

Rab-GTPases have been identified to interact with TPC1 and TPC2 through co-IP-mass spectrometry and was subsequent verified in overexpression systems [168]. It was observed that TPC2 but not TPC1 overexpression induces pigmentation defects in *Xenopus* oocyte, which could be corrected by a Rab7 inhibitor [168]. However, rather inconsistently, this study also claims that Rab interaction with TPC2 at the N-terminus is required for NAADP-induced Ca^{2+} release [168], despite that the same authors previously demonstrated that a TPC2 lacking the N-terminus (ΔN-TPC2) remains capable of supporting NAADP-induced Ca^{2+} transients [152].

1.6.6.3 LRRK2

LRRK2, a kinase overexpressed in Parkinson's disease, has also been shown to co-IP with TPC2 when overexpressed in HEK293T cells [170]. The LRRK2 effect on autophagosome number upon overexpression was found to be decreased by co-expressing a putative pore mutant of TPC2 [170], although caution should be made when interpreting some of these mutants (see notes under Table 1.2). Nevertheless, a recent study found that TPC2 but not TPC1 silencing reverted some of the lysosomal morphologies in fibroblasts from a LRRK2 mutant Parkinson's disease patient [174]. Further investigations should provide better insights into the potential role of TPC2 in Parkinson's disease.

1.6.7 Cellular functions of TPCs

So far, the role of TPC1 and TPC2 in the general functioning of the endolysosomal system is not clear. Endocytic receptor trafficking such as EGFR trafficking was

shown to be impaired in mouse embryonic fibroblast [171] while appeared to be normal in another study using the same cell type [133]. Similarly, toxin trafficking was shown to be impaired [154] while appeared to be normal in another study [133]. Lysosomal pH is also unaffected in most studies upon overexpression or knockout of TPC2 [133, 158, 166, 171] except that TPC2 knockout cells were unable to retain an acidic lysosomal pH upon starvation [158]. Cathepsin processing also appears to be normal upon experimental manipulation of TPC2 [166, 171]. Nevertheless, fusion processes involving the late endosomes/lysosomes with other organelles may be partially impaired in cellular processes such as autophagy.

1.6.7.1 NAADP-induced Ca^{2+} release

As discussed above, TPCs are Na^{+}-selective channels (Table 1.1 and refs therein) shown to be experimentally and theoretically sufficient to ensure negligible Ca^{2+} leakage (Ch.2) and show no concentration-dependent regulation by NAADP in HEK293 cells (see above) where the NAADP-binding protein is present [65, 66]. Nevertheless, based on the seminal study [65] and studies alike [99, 132], many efforts have followed this perspective that TPCs may be the gate for NAADP-induced Ca^{2+} release. This hypothesis has now been tested in several native preparations and rather coincidently, TPC silencing or knockout cells from native preparations indeed appeared to almost abolish or at least partially reduce NAADP-induced Ca^{2+} release [87, 98, 167]. Some studies have also shown that expression of TPC may correlate positively with the effect of NAADP or negatively with the effect of Ned-19 [96, 114, 166, 174], but see [90]. Given the now better characterized electrophysiological properties, these results may suggest that TPCs may be required to support NAADP-induced Ca^{2+} release, but likely via an indirect, supportive role in native preparations where additional factors are concomitantly present. Nevertheless, as minimal endolysosomal perturbations are observed upon

changes in TPC expression (see above), how this is accomplished will require further investigation.

1.6.7.2 Autophagy

In the context of autophagy, it was originally observed that TPC2 overexpression in astrocytes leads to increase in the number of autophagosomes in response to NAADP-AM and was thus concluded that NAADP and TPC2 may promotes autophagy [175]. An independent study has however shown that TPC2 overexpression alone without NAADP is sufficient to increase in the number of autophagosomes [166]. Indeed, more in depth investigation by the latter study has shown that TPC2 overexpression impairs autophagy progression most likely by inhibiting fusion of autophagosome with late endosomes/lysosomes without concomitantly impairing cargo degradation in the lysosomes and minimal alteration in lysosomal pH [166]. In both cases, the increase in autophagosome number could be reverted by BAPTA-AM [166, 175], suggesting an inhibitory role for cytosolic Ca^{2+} in the TPC2 effect on autophagy progression.

1.6.7.3 Cellular differentiation

TPCs have also been implicated in cellular differentiation process in myoblasts and embryonic stem cells. Knockdown of TPC1 or TPC2 reduced the expression of skeletal muscle markers and the number of multi-nucleated cells upon induction of differentiation [86], suggesting a role of TPCs in this process. In embryonic stem cells conditioned to undergo neural differentiation, TPC2 but not TPC1 has been shown to suppress the differentiation into neural progenitor cells while is required in subsequent differentiation into post-mitotic neurons [167]. Interestingly, both studies showed a dramatic reduction of TPC2 but not TPC1 RNA levels within 1-2

days after induction, which remain low throughout the later stages of differentiation [86, 167]. These studies therefore demonstrate the isoform-specific role of TPCs in cellular differentiation, although the underlying mechanism is less clear since only subtle endolysosomal changes is observed upon TPC knockdown or overexpression.

1.6.8 Whole-animal studies on TPCs

The generation of TPC knockout (*Tpcn2*$^{-/-}$) mice has allowed the investigation of the role of individual TPCs in whole-animal studies. So far, only permanent knockout animals have been reported and the generation of tissue-specific and/or the combined use of an inducible promoter should prove useful to circumvent potential compensatory mechanisms in permanent knockout animals.

1.6.8.1 Susceptibility to hepatosteatosis

In a recent whole-animal study, *Tpcn2*$^{-/-}$ mice have been shown to be more susceptible to the development of fatty liver and liver damage than wild-type mice when fed with high cholesterol diet [171]. At the cellular level, BODIPY fluorescence from LDL-BODIPY was found to accumulate in late endosome/lysosome in *Tpcn2*$^{-/-}$ MEFs [171], probably retained due to a non-dissipating lipophilic environment that causes dye retention, but could be induced by BAPTA-AM in wild-type MEFs which suggests a role for cytosolic Ca^{2+} [171]. However, how these observations connect mechanistically is unclear, although exaggerated accumulation of cholesterol droplets in *Tpcn2*$^{-/-}$ hepatocytes is obvious and enzymes involved in cholesteryl ester synthesis seem also to be upregulated considerably [171].

1.6.8.2 Neoangiogenesis

There is also evidence that TPC2 but not TPC1 may be required in VEGF-induced neoangiogenesis. At the whole-animal level, injection of VEGF-containing matrigel into wild-type animal readily results in the formation of blood vessels in the matrigel while this effect is abolished in *Tpcn2*$^{-/-}$ but not *Tpcn1*$^{-/-}$ mice [96]. In single-cell experiments, partial silencing of TPC2 indeed resulted in a considerable reduction in the amplitude of the VEGF-induced Ca^{2+} transient, which is accompanied by impaired performance in *in vitro* angiogenesis assays [96]. Nevertheless, how these observations connect mechanistically will, again, require further investigation. It is also not known how these animals developed a functioning vascular system given this neoangiogenic defect.

1.7 Conclusion

Since the first exciting discovery of IP_3, other potential endogenous products have been explored concerning their potential to mobilize Ca^{2+} physiologically. Despite more than 25 years of research on these other candidates including cADPR and NAADP, canonical Ca^{2+} release channels including IP_3Rs, RyRs and Ca_V channels remain the most established and dominant pathways for Ca^{2+} mobilization. The introduction above has highlighted the fact that it has proven difficult to translate the potential physiological function of cADPR and NAADP from sea urchin eggs to mammalian systems, given the uncertainty of crucial mechanisms concerning upstream mechanism, enzymatic pathway and receptor targets. This may be due to the fact that sea urchin eggs and mammalian systems probably have very different physiology at the cellular level.

Indirect evidence such as those from Ca^{2+} imaging experiments have implicated the potential involvement of TPCs in the NAADP effect. These indirect measurements must stand the test of further experiments that directly examine the channel properties of TPCs. Patch-clamp electrophysiology on cells overexpressing TPCs, unlike methods that require further biochemical procedure such as organelle and/or protein isolation, is the most direct and least convoluted experimental approach to examine their channel properties. Using this technique, together with quantitative fluorescence measurements and analysis, this thesis asks the question of whether pharmacological and ion permeation properties of TPCs, in particular the human TPC2, may satisfy or may be consistent with the requirement of a potential NAADP-sensitive Ca^{2+}-release channel.

2 Ion permeation properties of hTPC2

2.1 Abstract

Controversies surround the Ca^{2+} permeability of endolysosomal two-pore channels (TPCs) and whether they may be targets of the emerging Ca^{2+} mobilising messenger NAADP (Nicotinic Acid Adenine Dinucleotide Phosphate). Using combined electrophysiology, imaging and modelling approaches with a plasma-membrane targeted human TPC2 ($L^{11}L^{12}$/AA, $hTPC2^{PM}$) expressed in HEK293 cells, we found that, under these conditions, $hTPC2^{PM}$ is a H^+_o-activated Na^+-selective channel capable of conducting Na^+ within the lower physiological range (relative to extracellular [Na^+]). The permeability ratios of group I monovalent cations to Na^+ are similar to the voltage-gated Na^+ channel and the P_{Ca}/P_{Na} is 0.05. Consequently, the fractional Ca^{2+} current through $hTPC2^{PM}$ is close to zero (<0.0004) under physiological extracellular ionic conditions. Importantly, using experimentally verified models, we found that the permeation parameters of hTPC2 cannot support physiologically relevant $[Ca^{2+}]_i$ increase, while that of a non-selective cation channels (NMDA-R) can. Our quantitative analysis therefore allowed us to differentiate hTPC2 from non-selective cation channels, which are known to and able to participate directly in Ca^{2+} signalling, and suggests negligible role for hTPC2 to directly function as a physiologically relevant Ca^{2+} source.

2.2 Introduction

TPCs have been proposed to play an important role in NAADP-induced Ca^{2+} release in mammalian cells [65, 99, 132]. Through experimental manipulation of expression levels, it was found that the presence of TPCs in various mammalian preparations may correlate to the observation of NAADP-induced Ca^{2+} release [65, 98, 99, 132, 176]. It has thus been proposed that TPCs may be the long sought NAADP-sensitive

Ca^{2+} release channels with Ca^{2+} permeability assumed prior to electrophysiological characterization. Several subsequent studies reported the observation of putative NAADP-activated single-channel currents that may possess characteristics consistent with Ca^{2+} release channels [152, 164]. Single-channel Ca^{2+} currents with 15pS [164] and 40pS [152] were observed that were ascribed to TPC2 and P_{Ca}/P_{K} was found to be 2.6 [164].

Recently, during the time of this DPhil, by directly recording the macroscopic current of endolysosomal TPC2, several studies have reported that TPC2 may be Na^{+}-selective channels regulated by $PI(3,5)P_2$ and ATP, while being insensitive to NAADP [157-160]. The P_{Ca}/P_{Na} of TPC2 was found to be 0.1 under standard bi-ionic conditions [157], resembling that of the mammalian voltage-gated Na^{+} channel [177]. TPC2 appeared also to be impermeable to the large monovalent ions K^{+} and Cs^{+} [157], in contrast to the single-channel studies described above where single-channel K^{+} conductance as high as 300pS [164] and Cs^{+} conductance of 128pS [152] were reported. Moreover, macroscopic TPC2 current showed considerable time-dependent inactivation [157], a property not found in the putative NAADP-activated single-channel current [164]. These discrepancies suggest that properties of channels of dissimilar types might have been attributed to TPC2 (compare Table 1.1 and Table 1.2).

Recent reviews [178-180] have suggested that channels with a P_{Ca}/P_{Na} of <0.1 may leak high enough Ca^{2+} despite the absence of any Ca^{2+} current without any justification. Some have also suggested functional similarity between NMDA-R and TPC2 in terms of Ca^{2+} permeation [159, 180] while the difference in Ca^{2+} permeability is in fact 20-fold (P_{Ca}/P_{Na} of NMDA-R ~2 [181]; P_{Ca}/P_{Na} ~0.05-0.1 ([157, 160] and this thesis). Here, we sought to resolve the current controversies by obtaining permeation parameters of the human TPC2 (hTPC2) to allow quantitative characterization of the physical behaviour of ion signalling through and in the

nanometer vicinity of hTPC2. We found that the fractional Ca^{2+} current of hTPC2 is close to zero (<0.0004) and that the probability of Ca^{2+} signalling, relative to an ideally non-selective cation channel (P_{Ca}/P_{Na} = 1), is also close to zero (relative probability ~2 x 10^{-7}). Thus, our quantitative data suggest negligible role for hTPC2, and generally channels with P_{Ca}/P_{Na} ~0.05, to directly function as a physiologically relevant Ca^{2+} source.

2.3 Methods

2.3.1 Molecular biology and constructs

A modified Quick-change mutagenesis protocol [182] was used to generate the plasma membrane-targeted LL/AA hTPC2-mCherry using hTPC2-mCherry as the template (in the vector pcDNA5/TO (Life Technologies)), with the following primers (0.5µl of 20µM each, from Life Technologies),

Forward: 5′ GAG CCC ***GCA GCA*** GGC GGG GCC CGC GGC GGT GGC GGC GAC TGG
Reverse: 5′ GCC ***TGC TGC*** GGG CTC CGA CTC CGC CTG GGG TTC CGC CAT CCA

in a 20µl reaction using Pfu (2x Hotstart, Agilent) as the DNA polymerase. The PCR product was purified using the QIAquick PCR purification kit according to manufacturer instructions. The purified PCR product (30µl) was digested with 1.5ul DpnI (Fermentas) in a 35µl reaction to remove methylated DNA template. The DpnI-digested PCR product (3.5µl) was transformed into Z-competent (Zymo research) NEB5alpha cells (50µl, made from chemically competent NED5alpha cells (New England Bio lab)) according to manufacturer protocol. Transformed bacteria were plated on LB-ampicillin agar plates and incubated overnight at 37°C. Single colonies were cultured in 2.5ml LB-ampicillin overnight and had plasmid purified

using a miniprep kit (Fermentas). Miniprep plasmids were subjected to sequencing to identify colonies containing the desired mutation (LL/AA). One of the colonies containing the desired mutation was selected for large-scale plasmid purification from a 150ml culture in LB-ampicillin using a maxiprep kit (Qiagen). The final purified plasmid, full length LL/AA hTPC2, was subjected to sequencing to confirm the desired mutation and to ensure that no other mutations were introduced by PCR.

2.3.2 Cell culture and recombinant expression

HEK293 and HeLa cells were cultured in DMEM (Sigma) supplemented with 1% penicillin-streptomycin-L-glutamine (PSG, Sigma) and 10% FBS (Lonza), and were maintained in a humidified atmosphere containing 5% CO_2. HEK293 cells were transiently transfected with the cDNA of interest (hTPC2^{PM} or hCa$_V$3.1 (Addgene plasmid 45811)) using the standard calcium phosphate precipitation method. 2µg of DNA were used per transfection for a 35mm cell culture dish. Plasmid DNA was diluted in a 100µl 240mM $CaCl_2$ solution and was mixed, while vortexing, with 100µl 2x HBS. The co-precipitated plasmid was then added drop-wise directly to the medium. Cells were split 4-6 hrs post-transfection and were seeded at low density on poly-D-lysine-coated (Sigma) glass coverslips for patch-clamp experiments. For imaging experiments, HeLa cells cultured in DMEM supplemented with 1% PSG and 10% FBS on non-coated glass coverslips were transiently transfected with 2µg plasmid per 35mm cell culture dish using the jetPEI method (Polyplus transfection) according to manufacturer protocol. Cells were fed with fresh medium 4-6 hrs post-transfection to minimize toxicity. Recordings were typically performed 24-48hrs post-transfection.

2.3.3 Electrophysiology

The standard whole-cell voltage-clamp technique [183] was employed to record macroscopic whole-cell current of HEK293 cells expressing the construct of interest. Voltage clamp was performed using the Axopatch 200B amplifier controlled by the Clampex 10.3 software and the data were digitized through Digidata 1322A (all from Molecular Devices). Raw signals were analog-filtered through a 4-pole Bessel low-pass filter with a cutoff frequency of 5kHz and the sampling frequency was 10kHz. Data for display and plotting I-V curves were filtered offline with a Gaussian low-pass filter at a cutoff frequency of 250Hz. All plotted voltages were corrected for liquid junction potential according to [184], which was calculated in the Clampex 10.3 software. Borosilicate patch pipettes (3-6MΩ when filled with standard pipette solution, Harvard apparatus) were pulled using a vertical puller (Narishige) and were fire-polished using a microforge (Narishige). Single cells with moderate fluorescence (relative to all transfected cells), or occasionally doublets with both cells exhibiting fluorescence, were selected for patch-clamp experiments. Only cells with series resistance below 10MΩ, or occasionally below 15MΩ, were subjected to analysis.

2.3.4 Solutions

2.3.4.1 pH_o activation experiments

External (mM): 121 NaCl, 5.4 KCl, 2 $CaCl_2$, 0.8 $MgCl_2$, 6 $NaHCO_3$, 5.5 D-glucose, 25 HEPES, pH 8.00, 7.40 or 7.00; 25 MES for pH 6.50 or 5.50, titrated with NaOH
Internal (mM): 125 NMDG-$MeSO_3$, 20 NaCl, 1.13 $MgCl_2$, 1 EGTA, 10 HEPES, pH 7.20, titrated with NMDG-OH

Note: These solutions are referred to as normal solutions.

2.3.4.2 Na^+ influx experiments

Na^+-free External (mM): 127 NMDG-Cl, 5.4 KCl, 2 $CaCl_2$, 0.8 $MgCl_2$, 5.5 D-glucose, 25 HEPES, pH 7.40; titrated with NMDG-OH
External (mM): 121 NaCl, 5.4 KCl, 2 $CaCl_2$, 1.13 $MgCl_2$, 6 $NaHCO_3$, 5.5 D-glucose, 25 HEPES, pH 7.40; titrated with NaOH

To iso-osmotically reconstitute the indicated $[Na^+]_o$, Na^+-free external solution in the bath was mixed with external solution at the desired ratio at the time of addition.

2.3.4.3 Ca^{2+} imaging in the whole-cell configuration

External (mM): 121 NaCl, 5.4 KCl, 2 $CaCl_2$, 0.8 $MgCl_2$, 6 $NaHCO_3$, 5.5 D-glucose, 25 HEPES, pH 7.40; titrated with NaOH
Internal (mM): 125 K-gluconate, 20 NaCl, 1.13 $MgCl_2$, 1 EGTA, 3 MgATP, 0.3 NaGTP, 10 HEPES, pH 7.20, titrated with KOH

2.3.4.4 Fractional Ca^{2+} current experiments

External (mM): 121 NaCl, 5.4 KCl, 2 $CaCl_2$, 0.8 $MgCl_2$, 6 $NaHCO_3$, 5.5 D-glucose, 25 HEPES, pH 6.50, titrated with NaOH
Internal (mM): 125 NMDG-$MeSO_3$, 20 NaCl, 1.13 $MgCl_2$, 1 Fluo4-K_5, 10 HEPES, pH 7.20, titrated with NMDG-OH

2.3.4.5 Bi-ionic solutions for monovalent ions

External (mM): 145 X-Cl, 5.5 D-glucose, 25 MES, pH 5.50, titrated with NMDG-OH
X represents Li, Na, K, Cs or NMDG.
Internal (mM): 125 Na-gluconate, 20 NaCl, 1 EGTA, 10 HEPES, pH 7.20, titrated with NaOH

When K^+ is the external monovalent ion, 1mM $BaCl_2$ was added to block endogenous K_{ir}-like currents that occur in a subpopulation of cells. External Ba^{2+} does not block $hTPC2^{PM}$ at 1mM.

2.3.4.6 Bi-ionic solutions for $[Ca^{2+}]_o$ titration

External:
95mM $[Ca^{2+}]_o$ (mM): 95 $CaCl_2$, 5.5 D-glucose, 25 MES, pH 5.50, titrated with $Ca(OH)_2$
10mM $[Ca^{2+}]_o$ (mM): 10 $CaCl_2$, 130 NMDG-Cl, 5.5 D-glucose, 25 MES, pH 5.50, titrated with HCl
1mM $[Ca^{2+}]_o$ (mM): 1 $CaCl_2$, 143.5 NMDG-Cl, 5.5 D-glucose, 25 MES, pH 5.50, titrated with HCl
Internal (mM): 125 Na-gluconate, 20 NaCl, 1 EGTA, 10 HEPES, pH 7.20, titrated with NaOH

Note: in some experiments, especially those performed at pH_o 5.5, most external Cl^- was substituted with $MeSO_3^-$ and at least 5mM Cl^- was always present in the external solutions.

2.3.5 Live-cell confocal imaging

Fluorescence changes were monitored on the stage of the Ti Eclipse microscope using the Nikon A1 confocal imaging system (Nikon) equipped with a 60x (NA 1.49) oil objective in the laser-scanning mode. Data were recorded using the NIS elements software (Nikon). For time-lapse experiments, confocal images of 256x256 pixels were taken at 1-2s intervals. Photomultiplier (PMT) voltage was set so that the basal fluorescence level is roughly 1/8 of the maximal dynamic range of the detector in order to accommodate dynamic changes in fluorescent signals during the experiments. Varying PMT voltages across experiments do not affect the outcome of the experiments, as fluorescent signals were all normalized to the basal value (F/F_0) and were converted to intracellular ion concentration whenever possible from the F/F_0 data. Fluo-4, Fluo-3, ANG-2 and Fura-Red were excited using a 488nm laser. The emitted fluorescence from Fluo-3, Fluo-4 and ANG-2 were band-pass filtered at 525-575nm, while Fura-Red fluorescence was band-pass filtered at 663-738nm, before detection with the photomultiplier.

2.3.5.1 Na^+ influx experiments

HeLa cells were loaded with 5µM ANG2-AM (TefLabs) in normal extracellular solution for 40 minutes at room temperature in the dark. Cells were washed 3 times and were incubated with dye-free Na^+-free extracellular buffer (Na^+ being replaced with $NMDG^+$) for 20 minutes at room temperature for dye de-esterification. Cells were then imaged immediately. F/F_0 data were obtained after subtraction from background fluorescence.

2.3.5.2 Ca^{2+} imaging in the whole-cell configuration.

Fluo3/Fura-Red ratiometric imaging was performed. Stable hTPC2.HA HEK293 cells were loaded with 2µM Fluo3-AM (Life technologies) and 5µM FuraRed-AM

(Life technologies) in normal extracellular solution for 40 minutes at room temperature in the dark. Cells were washed 3 times with extracellular buffer and were then imaged ratiometrically in the whole-cell patch-clamp configuration. De-esterification period was omitted as the time required for obtaining a successful whole-cell configuration and recording serves essentially as a de-esterification period. Fluorescence intensity from each channel was background-subtracted before obtaining F/F_0 data. The Fluo-3 F/F_0 data were then ratioed with the Fura-Red F/F_0 data to obtain the R/R_0 signals.

2.3.5.3 Fractional Ca^{2+} current measurements

Simultaneous patch-clamp recording and Ca^{2+} imaging was performed to record current and Ca^{2+} as required for the analysis. 1mM Fluo-4 (penta-potassium salt, Life Technologies) was included in normal internal pipette solution without EGTA and EDTA. Upon achieving the whole-cell configuration, Fluo-4 diffuses into the cell and was allowed to reach equilibrium. This typically takes 5-6 minutes using pipettes with 3-5MΩ resistance and followed an exponential time course in most cases. Fractional Ca^{2+} current experiments were then performed upon complete equilibration of Fluo-4. Background fluorescence subtraction was not required here as the data were required as absolute changes in fluorescence amplitude. As such, specific to this set of experiments, the PMT voltage and the pinhole size were both kept constant for all the conditions examined. Images of 512x512 pixels were recorded at 30 fps using the resonant scanning mode.

2.4 Data analysis

2.4.1 Determination of permeability ratios

Standard symmetrical bi-ionic conditions were used to determine the permeability ratios of various monovalent cation to Na^+ (P_X/P_{Na}). Under this condition, the permeability ratio is given by

$$E_{\text{rev}} = \frac{RT}{F} \cdot \ln\left(\frac{P_{\text{X}}}{P_{\text{Na}}}\right) \tag{2.1}$$

where E_{rev} is the reversal potential, R, T and F have their usual thermodynamic meanings.

For divalent cations, the permeability ratio was determined by plotting E_{rev} against [divalent cation] and fitting the data with E_{rev} predictions using the GHK current equation accounting for I_{Na}, $I_{divalent}$ and I_{leak}, given by

$$\mathrm{I_{total}} = \mathrm{I_{Na}} + \mathrm{I_{divalent}} + \mathrm{I_{leak}}$$

$$I_{\text{i}} = z_{\text{i}}^2 \cdot F \cdot P_{\text{i}} \cdot D \cdot \frac{[ion]_{\text{i,o}} - [ion]_{\text{i,i}}\, \mathrm{e}^{z_{\text{i}} \cdot D}}{1 - \mathrm{e}^{z_{\text{i}} \cdot D}} \tag{2.2}$$

where D = VF/RT, z is the valence, V is the membrane potential, $[ion]_{i,i/o}$ indicates the i^{th} ionic species inside or outside, P is the absolute permeability of the i^{th} ionic species.

2.4.2 Analysis of pH_o-dependence

The pH_o-response data were fitted to the Hill equation in the form,

$$I = I_{\text{max}} \cdot \frac{1}{1 + 10^{n(pH - pEC50)}} \tag{2.3}$$

where n is the Hill coefficient and p is $-\log_{10}$.

2.4.3 Stationary noise analysis

Stationary noise analysis [185] was performed for stationary currents taken at minus 40mV of a duration of 500ms. The analog signals were, as described in the method above, low-pass filtered at 5kHz and were then filtered offline with a Gaussian low-pass filter at 800Hz. We assumed that most high frequency non-channel noises were filtered at this cutoff frequency and that channel noise likely dominates. The variance was computed for each test condition (pH_o 5.5-7.4) and was plotted against the respective mean currents ($\bar{I}$). The resulting variance-<I> relationship was fitted with the equation

$$variance = i \cdot \bar{I} - \frac{\bar{I}^2}{N} \tag{2.4}$$

where i is the single-channel current and N is the number of channels.

2.4.4 Estimating the single-channel Na^+ conductance of hTPC2

The single-channel Na^+ conductance was estimated using the following transformation (Ch.8 by Gray [186]),

$$i = \frac{variance}{\bar{I} \cdot (1 - P_O)} \tag{2.5}$$

where variance is the variance of the stationary current, <I> is the mean macroscopic current and P_o is the open probability. The digitized data were further low-pass filtered with a Gaussian filter at a cutoff frequency of 800Hz before calculating the variance. Estimation was performed at pH_o 5.5 at a symmetrical Na^+ gradient at

145mM. The P_o was taken at 0.5 from the results of stationary noise analysis of proton activation (Figure 2.5D), but the P_o at this pH is likely lower than 0.5 and so using a P_o of 0.5 would give an upper limit for the estimated unitary conductance. The resulting unitary currents were plotted against voltage to yield the slope unitary conductance (γ) for a 145mM symmetrical Na^+ gradient.

2.4.5 Fractional Ca^{2+} current measurements

Fractional Ca^{2+} currents were measured using the method of Schneggenburger et al 1993 [187]. Briefly, single HEK293 cells were loaded with 1mM fluo-4 through a patch pipette. The saturating [fluo-4] allows the capture of all the Ca^{2+} ions that have entered the cell through an elicited current according to Neher & Augustine 1992 [188],

$$\Delta Fluo4\text{-}Ca \;=\; Ca_{\text{influx}} \cdot \frac{\kappa_{\text{Fluo-4}}}{1 + \kappa_{\text{Fluo-4}} + \kappa_{\text{endo}}} \tag{2.6}$$

where $\kappa_{fluo\text{-}4}$ and κ_{endo} are the buffering ratio of fluo-4 and endogenous buffers respectively. Under this condition,

$$\Delta F_{\text{Ca}} \;=\; k \cdot \Delta Fluo4\text{-}Ca \;=\; k \cdot \Delta Q_{\text{Ca}} \tag{2.7}$$

$$\Delta F_{\text{ns}} \;=\; k \cdot \Delta Fluo4\text{-}Ca \;=\; k \cdot P_{\text{f}} \cdot \Delta Q_{\text{ns}} \tag{2.8}$$

where k is a proportionality constant, Q is the charge in coloumb, P_f is the fractional Ca^{2+} current and F is the fluorescence change in arbitrary units. The fractional Ca^{2+} current (P_f) is therefore given by [187],

$$P_{\text{f}} = \frac{F_{\text{ns}}}{Q_{\text{ns}}} \div \frac{F_{\text{Ca}}}{Q_{\text{Ca}}} \tag{2.9}$$

Simultaneous patch-clamp recording and Ca^{2+} imaging was performed to obtain the experimental values of F and Q, and the experimental P_f was derived according to eq.(2.9). For the determination of F_{Ca} and Q_{Ca}, recombinant hCav3.1 (T-type Ca^{2+} channel) currents were recorded.

The relationship between P_f and P_{Na}/P_{Ca} can be obtained by rearranging the GHK current equation describing the sum of parallel [181, 187], independent I_{Na} and I_{Ca} under symmetrical $[Na^+]$ and negligible intracellular $[Ca^{2+}]$,

$$P_f = \frac{1}{1 + \left(\frac{P_{Na}}{P_{Ca}}\right) \cdot \left(\frac{[Na^+]}{[Ca^{2+}]_o}\right) \cdot (1 - e^{(2VF/(RT))/4)})} \tag{2.10}$$

where $[Na^+]$ is the symmetrical Na^+ concentration on either side of the membrane and $[Ca^{2+}]_o$ is the external concentration of Ca^{2+}.

2.4.6 Modelling Na^+ flux

Na^+ influx was modelled by numerically integrating the GHK current equation using the forward Euler method,

$$\frac{d[Na^+]_i}{dt} = z^2 \cdot F \cdot D \cdot P_{max} \cdot \left(\frac{[Na^+]_o}{K_m + [Na^+]_o}\right) \cdot \left(\frac{[Na^+]_o - [Na^+]_i\, e^{z \cdot D}}{1 - e^{z \cdot D}}\right) \cdot \left(\frac{1}{z \cdot F \cdot vol}\right) \tag{2.11}$$

where D = VF/RT, V is the membrane potential, vol is the cell volume assuming a spherical cell of 10μm. We arrived at the following empirical relationship by noting that the experimental time constant of Na^+ flux is a Michaelis-Menten function of $[Na^+]_o$,

$$P = P_{max} \cdot \frac{[Na^+]_o}{K_m + [Na^+]_o} \quad (2.12)$$

2.4.7 Modelling global Ca^{2+} transient

Global Ca^{2+} transients were modelled by numerically integrating the differential equation in the form [187],

$$\Delta F_{(t)} = \frac{F}{Q} \cdot \Delta I_{(t)} \cdot \Delta t - \frac{\Delta t}{\tau} \cdot \Delta F_{(t)} \quad (2.13)$$

where τ is the time constant of decay. The experimental values of F/Q and I (a family of I_{hTPC2} at different step voltages) were used to drive Ca^{2+} influx. The resulting ΔF were converted into $[Ca^{2+}]_{free}$ assuming a spherical cell of 10μm radius and was scaled according to the buffering ratio of the cell [188],

$$\Delta[Ca^{2+}]_{free} = \frac{\Delta[Ca^{2+}]_{total}}{1 + \kappa_{endo}} \quad (2.14)$$

A κ_{endo} value of 63 [189] was used.

2.4.8 Modelling Ca^{2+} nanodomain

Ca^{2+} nanodomains were modelled according to a reaction-diffusion model [190, 191],

$$\frac{d(\Delta[Ca^{2+}])}{dt} = D_{Ca} \cdot \nabla^2(\Delta[Ca^{2+}]) - k_{on} \cdot [B]_{free} \cdot (\Delta[Ca^{2+}]) + k_{off} \cdot [CaB] \quad (2.15)$$

where D_{Ca} is the diffusion coefficient of free Ca^{2+}, k_{on} and k_{off} are the association and dissociation rate constants respectively, $[B]_{free}$ is the concentration of the free buffer of interest and [CaB] is the concentration of the Ca^{2+}-bound buffer of interest. With the use of the excess buffer and equilibrium approximations [190], the analytical solution is given by

$$\Delta[Ca^{2+}]_{free} = P_f \cdot \left(\frac{i_{total}}{4\pi D_{Ca} F r}\right) \cdot e^{-\frac{r}{\lambda}} \tag{2.16}$$

where

$$\lambda = \left(\frac{D_{Ca}}{k_{on} \cdot [B]_{total}}\right)^{\frac{1}{2}} \tag{2.17}$$

where r is the radial distance from the channel pore and i_{total} is the total unitary current at -60mV. The experimental values of P_f and i_{total} obtained in this study were used to predict the characteristics of the putative Ca^{2+} nanodomain of the hTPC2. The results were compared to a non-selective ion channel case, the NMDA receptor channel, using values obtained from [181] and [192]. For the numerical values of the parameters used in the simulations, see Table 2.1.

The relationship between the hemispherical volume ($\Delta[Ca^{2+}]_{free} > 300nM$) and P_{Ca}/P_{Na} was described empirically (within the range of P_{Ca}/P_{Na} under investigation),

$$radius\ (\Delta[Ca^{2+}]_{free} > 300nM) \sim A_1 \cdot \frac{P_{Ca}}{P_{Na}}$$

$$hemispherical\ volume\ (\Delta[Ca^{2+}]_{free} > 300nM) \sim A_2 \cdot \left(\frac{P_{Ca}}{P_{Na}}\right)^3 \tag{2.18}$$

where A_1 and A_2 are proportionality constants.

For stochastic simulation of Ca^{2+} nanodomains, we generated random numbers that obey the Ca^{2+} nanodomain model using the inverse transform method [193]. The probability density function of the model was approximated using a power series containing 10 terms. The resulting random numbers representing the simulated radial distances were transformed into their corresponding x, y and z coordinates in spherical coordinates using uniformly distributed random θ and ◎, and were plotted in three-dimension using Igor Pro (Wavemetrics).

2.4.9 Data analysis

Data analysis, curve fitting, statistical tests and modelling/simulations were performed in Excel (Microsoft) and Prism 5 (GraphPad software). Data are presented as mean ± S.E.M.. Parameters obtained from curve fitting are presented as value ± standard error of fit. The student's t-test was used to test for potential statistical difference between two groups. For multiple comparisons, ANOVA was used, followed by the Tukey's HSD test when significant difference was detected by ANOVA. P values of <0.05 were considered statistically different.

2.5 Results

2.5.1 Recombinant expression of hTPC2 alone does not support NAADP-induced Ca^{2+} release in HEK293 cells

We performed experiments similar to Figure 2 in Calcraft et al 2009 by introducing free NAADP into the same stock of hTPC2.HA-stable cell via whole-cell patch-clamp. Ratiometric imaging using Fluo-3/FuraRed was used to avoid confounding signals that may not correspond to genuine Ca^{2+} transients. Immunocytochemistry was used to verify the expression of hTPC2.HA in the stable cell line as shown in Figure 2.1A. We kept the series resistance low to facilitate rapid dialysis of NAADP into the cell under investigation and monitor the seal by simultaneously recording plasma membrane currents.

Figure 2.1B shows the R/R_0 signals upon the establishment of the whole-cell configuration (t=0) when NAADP is present at the indicated concentration in the pipette solution. It can be seen that NAADP neither at 100nM (n=16) nor at 10μM (n=5) induced well-defined Ca^{2+} transients that were reported in Calcraft et al 2009. We therefore performed positive control experiments to verify that our experimental conditions can report Ca^{2+} transients induced by the more established Ca^{2+}-mobilizing messenger IP_3. As shown in Figure 2.2B, IP_3 introduced into the cell using identical methods, cell line and solutions induced robust Ca^{2+} transients (note the difference in the scale of the y-axis) in 100% of the cells investigated (n=13). We also checked that our NAADP, which was freshly reconstituted at the time, was indeed active using SUEH. As expected, NAADP at 100nM in the cuvette induced Ca^{2+} release from SUEH vesicles that is self-desensitizing without affecting the action of cADPR (Figure 2.2A).

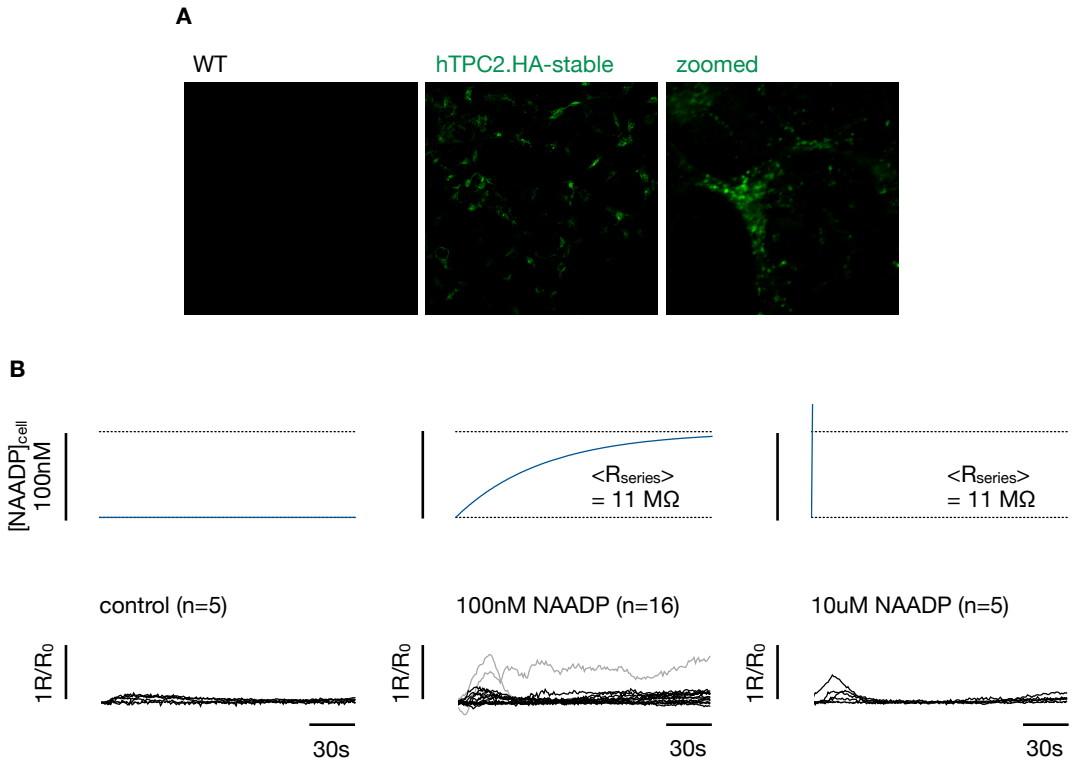

Figure 2.1 NAADP failed to evoke Ca^{2+} transients in HEK293 cells stably expressing hTPC2.HA

A. Confocal images showing expression of hTPC2.HA in the stable HEK293 cell line but not in control HEK293 cells. hTPC2 was visualized by immunofluorescence using an anti-HA antibody.

B. NAADP did not evoke Ca^{2+} transients in HEK293 cells stably expressing hTPC2.HA at a pipette concentration of 100nM and 10µM. Cells were co-loaded with 2µM Fluo3-AM and 5µM FuraRed-AM for 40 minutes and were imaged ratiometrically. R/R_o indicates Fluo-3/Fura Red intensity ratio. Shown above the traces are the expected dialysis time profile of NAADP given the averaged series resistance according to Pusch & Neher 1988 [194].

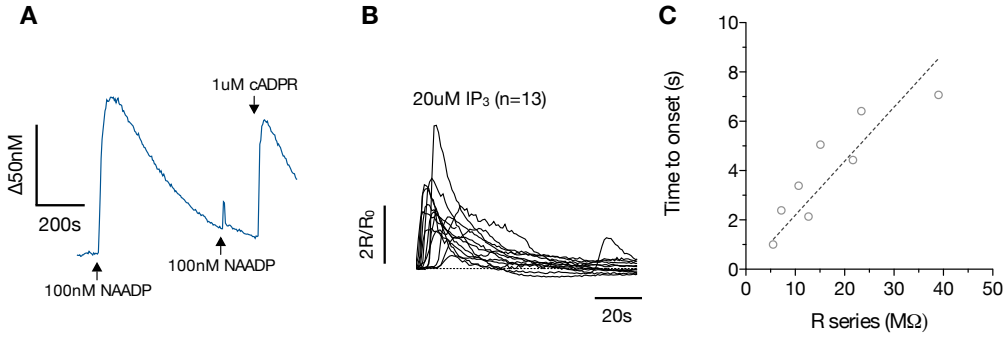

Figure 2.2 Positive controls for the NAADP experiments shown in Figure 2.1

A. Positive control showing that NAADP is active. 100nM NAADP was added to sea urhin egg homogenate to induce Ca^{2+} release from vesicles that shows homologous desensitization without affecting cADPR-induced Ca^{2+} release as originally observed in [56]. n = 3.
B. Positive control showing robust IP_3-induced Ca^{2+} transients in HEK293 cells stably expressing hTPC2.HA. Robust Ca^{2+} transients were observed upon break-in following a characteristic lag time. n = 13.
C. Relation between series resistance and lag time showing that these experimental quantities are closely and positively correlated [194], an important check to validate the dialysis process but is missing from all studies employing this method in the study of NAADP-induced Ca^{2+} release. It is therefore difficult to assess the validity of the results obtained in many previous studies claimed to be NAADP-induced Ca^{2+} release [65, 78-80, 85, 94, 154, 176, 195, 196] using this method.

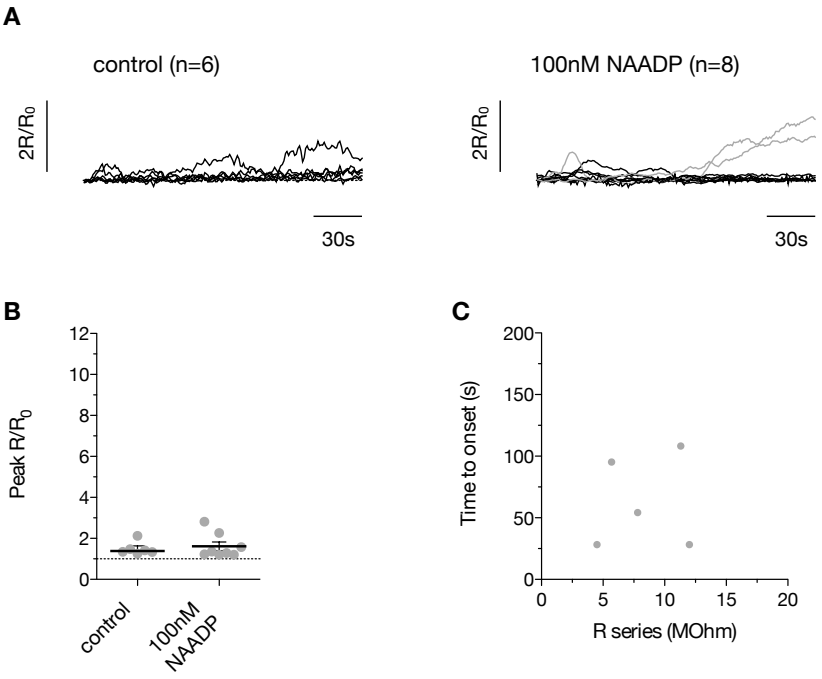

Figure 2.3 NAADP does not evoke intracellular [Ca^{2+}] changes in MEFs

A. Experiment as in Figure 2.1 but performed with MEFs. NAADP at 100nM pipette concentration did not evoke specific Ca^{2+} transients in MEFs in the whole-cell configuration. n = 6 for control and 8 for 100nM NAADP.
B. Peak R/R_0 is not significantly different between control and 100nM NAADP. p=0.18, student's t-test.
C. Lag time does not correlate with series resistance, indicating that the R/R_0 fluctuations cannot be attributed to substances diffusing from the pipette; compare with IP_3 in Figure 2.2.

In addition, as mouse embryonic fibroblasts (MEFs) were claimed to be robust responders to NAADP-AM at the time [197], we performed the same experiment

using MEFs under the same experimental conditions. We found that MEFs in fact do not respond to free NAADP at a pipette concentration of 100nM (Figure 2.3). This seems to be consistent with the lack of NAADP binding in these cells (in-house unpublished data).

2.5.2 Plasma membrane targeting of hTPC2

Results from the above experiments point to two questions – 1) is hTPC2 NAADP-sensitive in HEK293 cells, and 2) is hTPC2 a Ca^{2+}-permeable channel? Addressing these questions requires direct assessment of the channel properties of hTPC2. However, as hTPC2 is intracellular, it is not directly amenable to the traditional whole-cell patch-clamp technique. We therefore targeted hTPC2 to the plasma membrane by mutating its N-terminal di-leucine motif [152] (LL/AA hTPC2.mCh or $hTPC2^{PM}$). Indeed, as can be seen in Figure 2.4, $hTPC2^{PM}$ when overexpressed in HEK293 cells exhibit a surface-bound pattern of expression common to plasma membrane proteins. Moreover, its detection by TIRF, in which excitation intensity decays exponentially within 200nm from the coverslip, further suggests successful targeting to the plasma membrane.

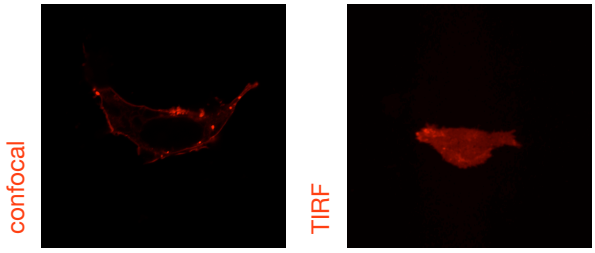

Figure 2.4 Plasma-membrane targeting of hTPC2

Representative confocal (left) and TIRF (right) images of HEK293 cells transiently expressing the di-leucine mutant LL/AA hTPC2.mCh.

2.5.3 hTPC2^{PM} can be activated by external H^+

The lysosomal lumen has a pH of 4.6. To mimic this acidic environment, we lowered the external pH from 7.4 to a moderately acidic pH 5.5. Lowering to pH 4.6 was not possible as this leads to cell deterioration. We found that robust activation of hTPC2^{PM} occurs as the external environment becomes more acidic (Figure 2.5A). This current is not observed in non-transfected cells and cells expressing a putative pore-dead mutant (D276K hTPC2^{PM}) (Figure 2.7A), indicating that this current is likely mediated by functional TPC2.

Instantaneous currents were plotted against the applied voltage, which shows the inwardly rectifying properties of the hTPC2^{PM} current given the asymmetrical Na^+ gradient used (Figure 2.5B). The I-V curves reversed at a reversal potential close to E_{Na} (experimental = 37.4 ± 0.6 mV, E_{Na} = +46.6mV, E_{Ca} = +154mV), suggesting that the dominant permeating ion could be Na^+, which was also the only dominant monovalent ion present. Nevertheless, because of the presence of other physiological cations, bi-ionic recording conditions are required to rigorously measure relative permeabilities as shown below.

At hyperpolarizing voltages, the current exhibits slow decay without an accompanying activation phase. We suspect that the lack of an activation phase may be due to a potential component of voltage-dependent potentiation that is too fast to be resolved. We also suspect that fast unblocking of internal $NMDG^+$ likely underlies the exaggerated rectification, as the internal solution had 125mM $NMDG^+$. We observed that internal $NMDG^+$ probably blocks hTPC2 when present at high concentration, as symmetrical Na^+ recording condition containing symmetrical $NMDG^+$ result in an strongly inwardly rectifying current, while symmetrical Na^+ recording conditions without $NMDG^+$ results in a linear I-V curve (not shown). The

potential fast potentiation and slow decay suggest that hTPC2 exhibits some voltage-dependent characteristics.

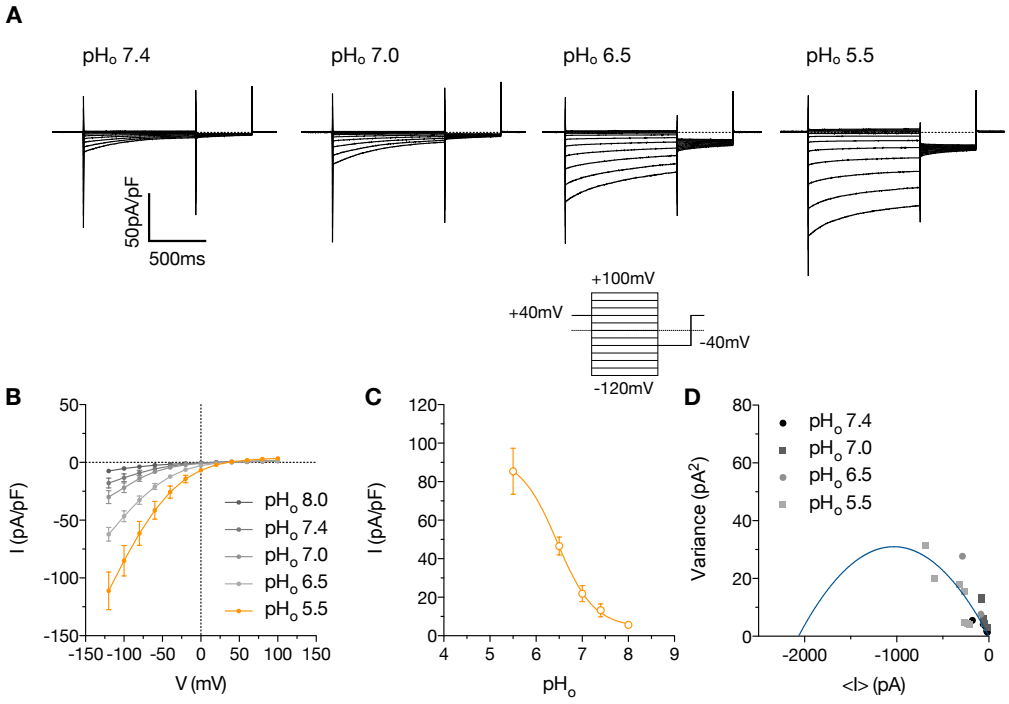

Figure 2.5 Proton-activated current through hTPC2^{PM}

A. pH$_o$-dependent activation of hTPC2^{PM}. hTPC2^{PM}-expressing HEK293 cells were recorded in standard external and internal solutions (see method for solution composition) using a voltage step-pulse protocol; V_{hold} = +40mV, V_{tail} = -40mV. Shown are averaged recordings of n = 5-8 cells for each condition.
B. I-V plot of the instantaneous currents under increasingly acidic external environment showing pH-dependent activation of hTPC2^{PM}, n = 5-8 cells for each condition.
C. pH-dependent increase in the current density taken at -100mV. The data were fitted to eq.(2.3). The parameters obtained from the fit are EC_{50} = 6.46 ± 0.12 pH units and Hill slope = 1.09 ± 0.28.
D. Stationary noise analysis of the stationary currents taken at -40mV. Each data point represents the mean current amplitude <I> and the corresponding variance of each cell under the indicated pH conditions. The obtained relationship between variance and <I> suggests that an increase in P_o likely underlies the increase in <I>. The data were fitted to eq.(2.4). The parameters obtained from the fit are i = -0.06 ± 0.01pA, N = 34462 ± 29155 and $<I>_{max}$ = -2064.46pA at -40mV (the non-zero x-intercept).

The concentration-response profile is shown in Figure 2.5C, which identifies an EC_{50} of 6.46 ± 0.12 pH units. Exogenous $PI(3,5)P_2$ was not required under this condition and hTPC2^{PM} appeared to be functional at cellular ATP level as constitutive current

was observed immediately after break-in before any significant dialysis can occur (complete dialysis of cellular K^+ typically requires ~1min). Substantial loss of cellular ATP instantaneously upon break-in is therefore unlikely.

To investigate whether external protons may activate hTPC2^{PM} by increasing its open probability (P_o), we performed stationary noise analysis with the stationary currents obtained at -40mV. The variance-mean current plot shown in Figure 2.5D shows that the variance increases with <I> within the range of investigation. This trend is consistent with an increase in P_o, suggesting that hTPC2^{PM} may be activated at the P_o level under acidic conditions. Nevertheless, because of the limited range of investigation, the maximal P_o cannot be measured unambiguously. This is reflected from the fit. While the estimated i has a small standard error of fit and is thus a more reliable estimate, the estimated N, the total number of channels, is ambiguous. This is due to the fact that i is the slope at 0, which is reasonably well represented by the data. Regardless, our data indicate that hTPC2 can be and may be constitutively activated at lysosomal pH_o.

2.5.4 hTPC2^{PM} is not activated by NAADP

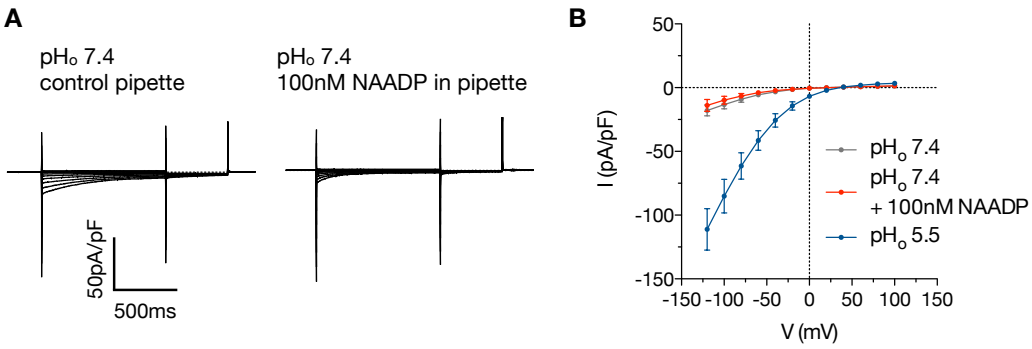

Figure 2.6 NAADP does not activate hTPC2^{PM}

A. Averaged current recorded from HEK293 cells transiently expressing hTPC2^{PM} with or without 100nM NAADP in the internal solution in response to a voltage-step protocol; V_{hold} = +40mV, V_{tail} = -40mV. n = 8 each.

B. I-V plots for the data shown in A.

In addition, we tested whether the channel itself can be activated by NAADP. We found that at 100nM pipette concentration, NAADP did not seem to activate any current (Figure 2.6). This is in contrast to the robust activation observed when extracellular pH is lowered to pH 5.5 (Figure 2.6B).

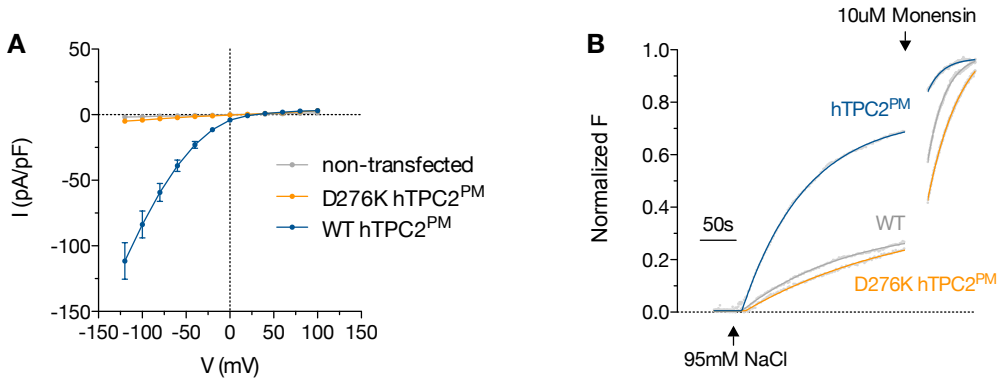

Figure 2.7 Na^+ current and influx are both dependent on functional $hTPC2^{PM}$

A. I-V plots from HEK293 cells transiently expressing $hTPC2^{PM}$ or a putative pore mutant D276K $hTPC2^{PM}$. Currents were recorded at pH_o 5.5 in normal extracellular and intracellular solutions (see section 2.3.4.1). n = 7-8 each.

B. Na^+ influx experiments as in Figure 2.9 showing that the putative pore mutant D276K $hTPC2^{PM}$ was unable to mediate Na^+ influx in HeLa cells. For solutions, see section 2.3.4.2. n = 3-4 coverslips each.

2.5.5 $hTPC2^{PM}$ is a Na^+-selective channel

Figure 2.8A shows the I-V plots of $hTPC2^{PM}$ currents under bi-ionic Na^+ conditions. Internal Na^+ was fixed at 145mM while external Na^+ was varied as indicated. Increasing external [Na^+] selectively increases inward current relative to outward current (Figure 2.8A) and shifted the reversal potential according to the GHK voltage prediction (Figure 2.8C), confirming the Na^+-dependence of the $hTPC2^{PM}$

current. Cl^- and H^+ are both impermeant as the reversal potential under symmetrical Na^+ gradient was close to 0mV despite a sizable pH and Cl^- gradient (see solution composition). We note that $NMDG^+$ is also not permeant as external [Na^+] were varied by substitution with $NMDG^+$, which did not affect the E_{rev}-$[Na^+]_o$ relationship (Figure 2.8C).

To determine the monovalent ion selectivity sequence, we performed ion substitution experiments under bi-ionic condition by substituting external Na^+ with different monovalent cations. The I-V relations are shown in Figure 2.8B. The I-V relations were normalized to the current at +100mV (as it is minimally contributed by inward current), as the absolute amplitude of the current has no bearing on this comparison. For some instantaneous currents where shallow rectification is observed at about +100mV, the current was extrapolated by fitting the non-rectifying section of the I-V curve with the GHK current equation (eq.(2.2)) for normalization purposes. Of the group I cations, only Na^+ and Li^+, but not the larger K^+ and Cs^+, gave rise to inward current when present on the external side. Reversal potentials were converted into P_X/P_{Na} using eq.(2.1), which yielded the following permeability sequence (Figure 2.8D): Na^+ (1) ≥ Li^+ (0.9) >>> K^+ (0.06) > Cs^+ (0.03) > $NMDG^+$. We note that this permeability sequence resembles that of the voltage-gated Na^+ channels, one of the most Na^+-selective mammalian ion channels known to date.

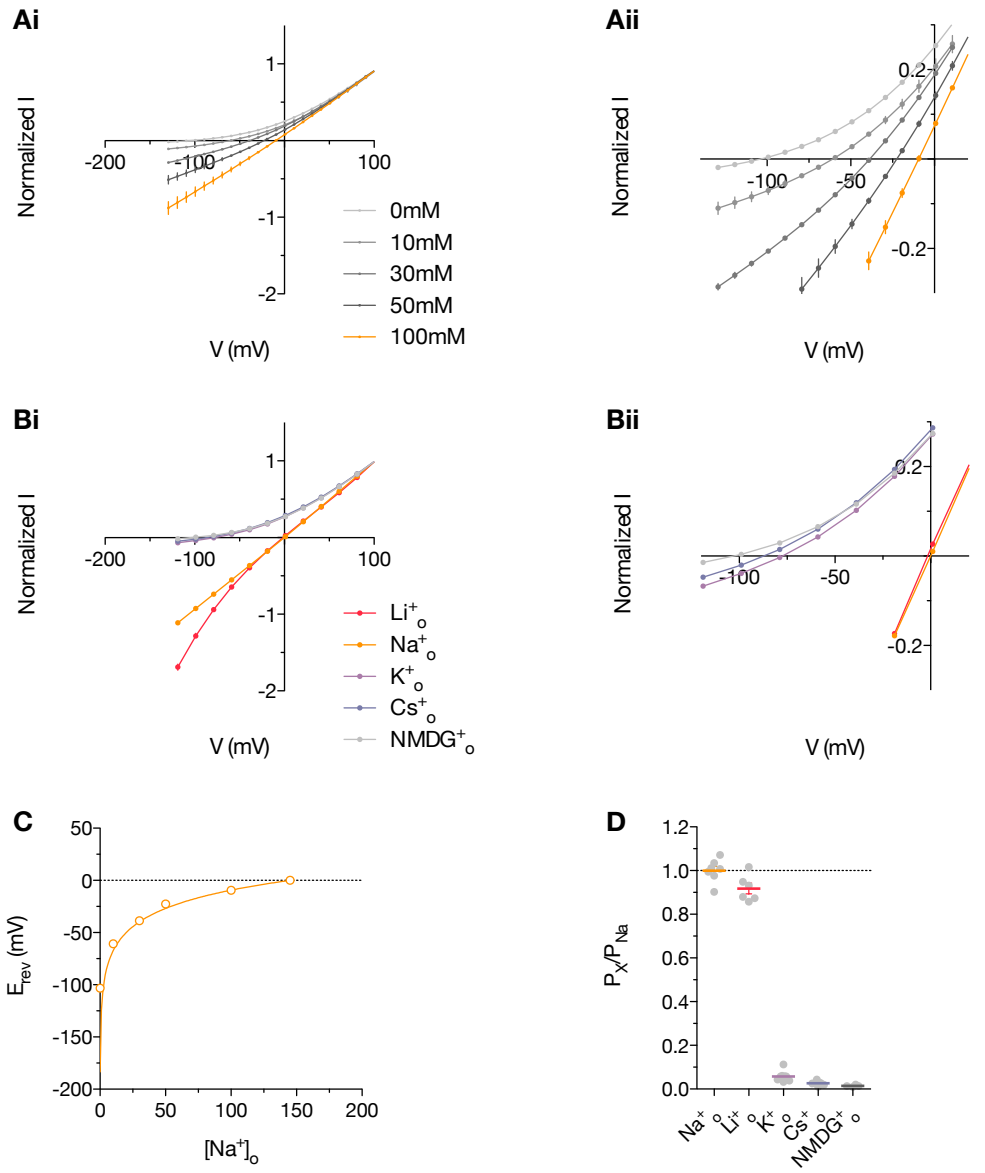

Figure 2.8 Na^+-selective ion conduction through $hTPC2^{PM}$

A. I-V curves showing the Na^+-dependence of the hTPC2 current under bi-ionic Na^+ condition. Internal [Na^+] was fixed at 145mM while external [Na^+] was varied as indicated, n = 4-9 each. $NMDG^+$, an impermeant ion, was used to maintain the osmolarity of the solutions. Ai, original scale; Aii, expanded scale.

B. I-V curves showing the relative permeability of group I monovalent cations under bi-ionic condition. Internal [Na^+] was fixed at 145mM and external Na^+ was substituted as indicated all at 145mM, n = 5-8 each. Bi, original scale; Bii expanded scale.

C. Reversal potential (E_{rev}) obtained from experiments shown in A plotted against external [monovalent ions]. The data was fitted to the GHK voltage equation (eq.(2.1)), which also accounts for substitution with $NMDG^+$ when $[Na^+]_o$ was lowered.

D. P_X/P_{Na} of the indicated monovalent cations obtained using the GHK voltage equation (eq.(2.1)).

2.5.6 hTPC2^{PM} operates at [Na^+] within the lower physiological range

To test whether this Na^+ current may impact on cellular Na^+ dynamics, we performed Na^+ imaging with a fluorescent Na^+ indicator Asante Natrium Green-2 (ANG-2, *in situ* K_d=18.2mM (Figure 2.9B)). This is shown in Figure 2.9A where $[Na^+]_o$-dependent Na^+ influx at the millimolar level was observed upon iso-osmotic re-addition of the indicated $[Na^+]_o$, indicating the high Na^+ permeability of hTPC2^{PM}-overexpressing plasma membrane. In contrast, non-transfected cells and cells expressing a putative pore-mutant that is electrophysiologically non-functional gave only background Na^+ influx (Figure 2.7B).

We fitted the flux data (Figure 2.9A) with a monoexponential function and obtained the time constants for all $[Na^+]_o$. When plotted against $[Na^+]_o$, the data follow the Michaelis-Menten relation (Figure 2.9C) with a K_m of 20.8 ± 4.95mM, which indicates that the affinity for Na^+ permeation of hTPC2 is well within the physiological range. To test whether the flux data is consistent with electrodiffusion of Na^+, we numerically integrated the GHK current equation incorporated with the Michaelis-Menten dependence of permeability (eq.(2.11) & (2.12)). Indeed, the time constants and equilibrium $[Na^+]_i$ from the model are seen to recapitulate quantitatively most features of the flux data (Figure 2.9A, C & D).

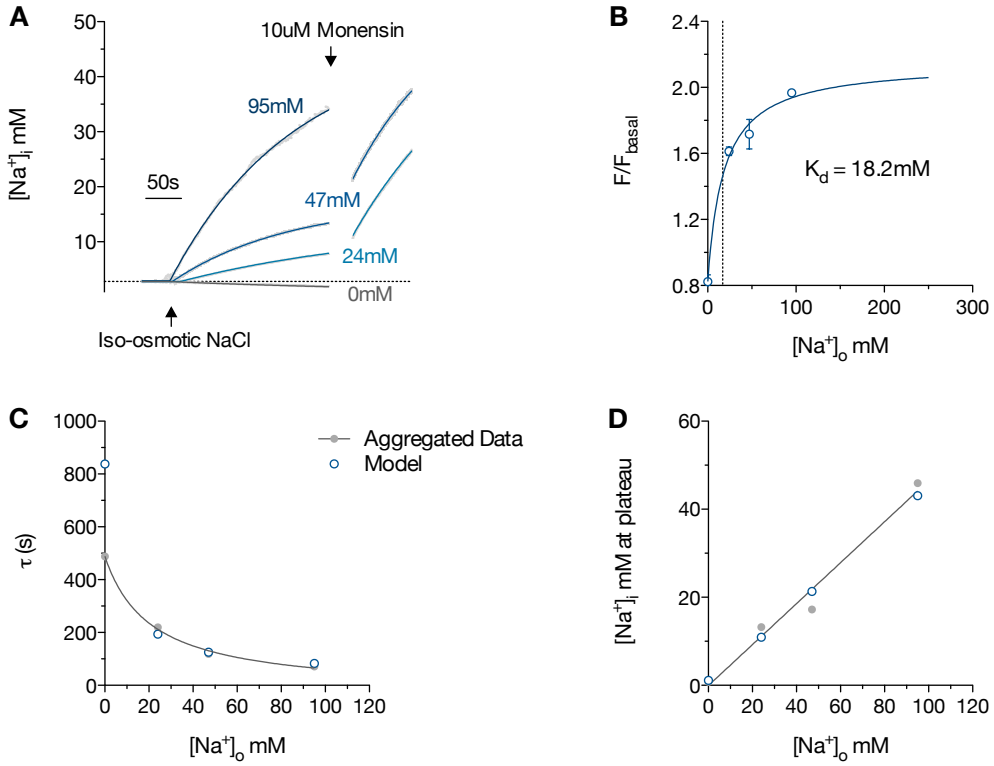

Figure 2.9 Na^+ electrodiffusion through $hTPC2^{PM}$

A. Na^+_o dependence of Na^+ influx in HeLa cells. Cells were loaded with 5µM ANG2-AM in normal external solution and intracellular ANG-AM was allowed to de-esterify completely in Na^+-free external solution. Arrow indicates iso-osmotic reconstitution of the indicated $[Na^+]_o$ to induce Na^+ influx. The Na^+ ionophore monensin was used to completely equilibrate the cellular $[Na^+]$ with the external $[Na^+]$ for calibration purposes. N = 3-4 coverslips for each condition.

B. *In situ* calibration of ANG-2; K_d = 18.2mM (K_d reported by Teflabs = 20mM). For calibration, F/F_0 values during the plateau reached after the addition of monensin were measured. The F/F_0 values were then plotted against their respective extracellular $[Na^+]$. Experiments performed using free ANG-2 dye at pH 7.0 showed a similar K_d (not shown).

C. Experimental and predicted time constants of Na^+ influx. Grey points are experimental time constants obtained from monoexponential fits of the data in A and were fitted to the Michaelis-Menten equation with K_m = 20.8 ± 4.95mM. Blue points are time constants of the predicted flux behavior modeled by numerically integrating the GHK current equation (eq.(2.11) & (2.12)) using the forward Euler method. The absolute permeability (given the expression level) obtained was P_{Na} = 1.5 x 10^{-14}cm/s and other constant parameters in eq.(2.11) & (2.12)) are V_m = +20mV, K_m = 20.8mM (experimental value) and spherical cell radius = 10µm; T = 293K.

D. Experimental and predicted $[Na^+]_I$ at plateau; methods as in C.

2.5.7 Estimating the unitary Na^+ conductance of hTPC2

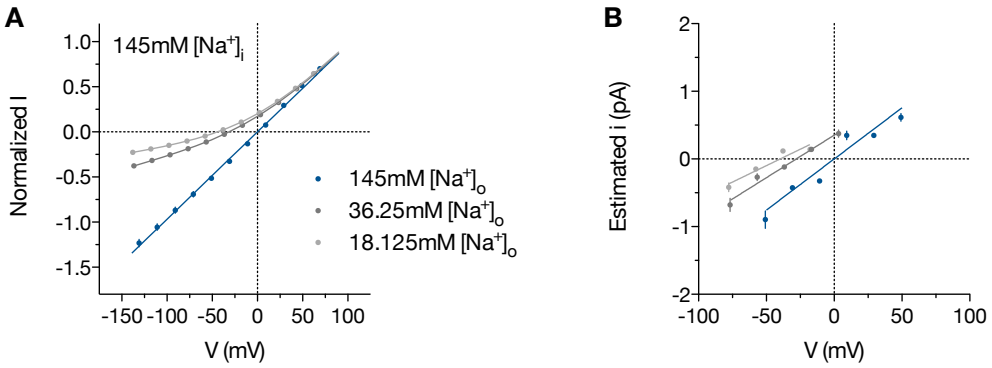

Figure 2.10 Estimation of slope conductance at symmetrical 145mM [Na^+] gradient

A. I-V relation recorded at the indicated $[Na^+]_o$; internal $[Na^+]_i$ was fixed at 145mM. Currents were normalized for illustration purposes; non-modified stationary currents were used to estimate the unitary slope conductance. n = 3-7 each.

B. i-V plot showing the estimated unitary current from A. Non-modified macroscopic currents at voltages close to E_{rev} were transformed according to eq.(2.5). P_o was set to 0.5 but it is likely that the maximal P_o is smaller than 0.5. Smaller P_o gives lower slope conductance according to eq.(2.5). The estimated slope conductance is 15.1±1.02 pS at symmetrical 145mM [Na^+].

At symmetrical 145mM [Na^+], it is possible to estimate the slope unitary conductance (γ) by a transformation method based on stationary noise analysis (eq.(2.5) and section 2.4.4). Macroscopic currents at voltages close to E_{rev} were transformed into unitary currents (i) according to eq.(2.5) and the P_o was set to 0.5 (Figure 2.10). As a control, we performed the same procedure at decreasing $[Na^+]_o$ while internal [Na^+] was fixed. We found that as $[Na^+]_o$ is decreased, γ estimated by this procedure decreased accordingly (Figure 2.10B). As expected, the estimated i is also linearly dependent of voltage at about E_{rev} (Figure 2.10B). The concentration and voltage dependence together suggest that this is unlikely to be an artifact due to other interfering electronic noise. The unitary conductance estimated using this method is 15.1±1.02 pS at symmetrical 145mM [Na^+]. This value represents an upper limit of the estimated γ, as the maximal P_o is likely lower than 0.5; the estimate

single-channel slope conductance should in fact be lower than 15pS. However, because of filtering, the current estimation may represent an underestimate.

2.5.8 hTPC2^{PM} is impermeable to Ca^{2+} at levels that occur physiologically

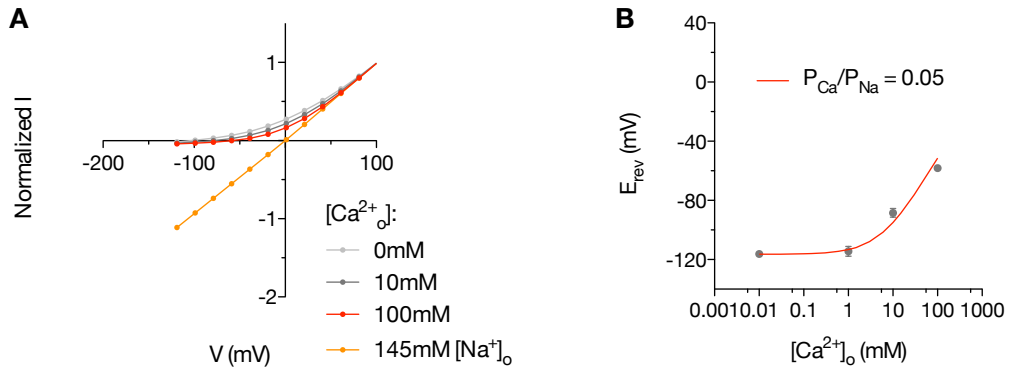

Figure 2.11 hTPC2^{PM} is impermeable to Ca^{2+} at physiological [Ca^{2+}] levels

A. I-V curves showing concentration-dependence of Ca^{2+} in the supraphysiological range (n = 5-8 each).

B. Relationship between E_{rev} and $[Ca^{2+}]_o$. E_{rev} were obtained from experiments shown in A. The data are overlaid with GHK current predictions modeling a sum of parallel independent I_{Na}, I_{Ca} and I_{leak} with the indicated P_{Ca}/P_{Na}. The prediction recapitulates the experimental relationship when P_{Ca}/P_{Na} is 0.05.

Due to the controversial Ca^{2+} permeability of hTPC2, we sought to investigate whether physiologically relevant $[Ca^{2+}]_o$ may give rise to inward current and thus rightward shift in the reversal potential in the absence of any competing ions. As can be seen in Figure 2.11A, addition of 1mM $[Ca^{2+}]_o$ to the $NMDG^+$-based external solution failed to shift the reversal potential in the positive direction. As ion permeation is concentration-dependent, we increased the external $[Ca^{2+}]_o$ from 1mM to 100mM and plotted the respective reversal potentials against $[Ca^{2+}]_o$. Indeed, we observed $[Ca^{2+}]_o$-dependent Ca^{2+} permeation which, however, was only measurable at $[Ca^{2+}]_o$ >5mM (Figure 2.11B), which is beyond levels that occur physiologically.

We overlaid the data with GHK current prediction, which models the sum of parallel, independent I_{Na}, I_{Ca} and I_{leak}, and found that P_{Ca}/P_{Na} is 0.05, consistent with that obtained by Wang et al 2012 [157]. We also note that at lysosomal [Ca^{2+}] (~500μM, [121]), there should be no observable Ca^{2+} current through hTPC2 according to this data.

2.5.9 F/Q ratio and fractional Ca^{2+} current (P_f)

As a more rigorous test, we investigated quantitatively the relationship between hTPC2 current and Ca^{2+} influx by performing simultaneous whole-cell patch-clamp and confocal Ca^{2+} imaging. We employed the F/Q ratio test originally proposed by Schneggenburger et al 1993 [187] to estimate the fractional Ca^{2+} current (P_f) through hTPC2 (see methods for methodological details). We held the cell at +60mV to minimize basal Ca^{2+} influx and Ca^{2+} influx was induced by a 1s voltage step pulse at the indicated voltages. For the recording of hCav3.1, cells were held at -90mV.

We performed these experiments using normal external solution, i.e. external [Na^+] = 127mM, external [Ca^{2+}] = 2mM, at pH_o 6.5, and normal internal solution, i.e. internal [Na^+] = 20mM, 1mM Fluo-4 without EGTA/EDTA. The normal extracellular [Ca^{2+}] may be considered supraphysiological for the normally lysosomal TPC2 as lysosomal [Ca^{2+}] have been reported to be ~500μM.

As qualitatively illustrated in Figure 2.12 and quantified as F-V and I-V plots in Figure 2.13A, we found that despite the large integral of hTPC2 currents, there was no significant difference ($p>0.05$) in the amplitude of the fluorescent signals between non-transfected and $hTPC2^{PM}$-expressing cells and that their F-V curves are identical in shape. The latter suggests that the two curves in fact obey the same underlying function. These observations suggest that background currents due to variable seal

resistances, and therefore the inevitable co-occurrence of non-selective currents, account for most, if not all, of the fluorescent signals observed in hTPC2^{PM}-expressing cells when the voltage step pulses were elicited.

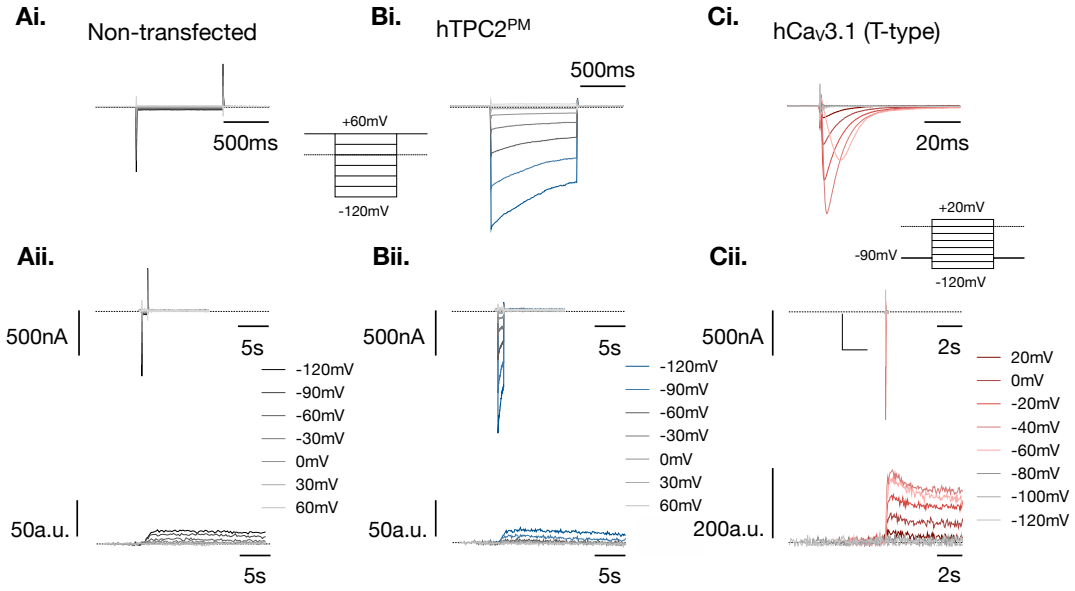

Figure 2.12 Negligible Ca^{2+} influx through hTPC2 revealed by simultaneous patch-clamp/Ca^{2+} imaging

Ai, Bi and Ci. Representative current recordings in expanded time-scale at the indicated voltages for non-transfected, hTPC2^{PM}-expressing and hCa$_V$3.1-expressing HEK293 cells, respectively (n = 7-8 each). Aii, Bii and Cii. Paired current and fluorescent traces showing fluorescent increase upon the application of a voltage protocol at the indicated voltages (see text for details).

To obtain the maximal F/Q ratio, we performed recordings from HEK293 cells expressing the human T-type voltage-gated Ca^{2+} channel (hCa$_V$3.1), whose P_f is assumed to be 1. As shown in Figure 2.12C, activation of hCa$_V$3.1, *with a duration as short as <20ms*, was able to elicit rapid, step-like fluorescent changes of ~200a.u. (Figure 2.12C & Figure 2.13B), which, in addition, illustrates the high sensitivity of our recording method. Importantly, the F-V and I-V relations obey the GHK current equation scaled with the normalized Boltzmann equation (Figure 2.13B) and that the

F-V plot is a mirror image, around the x-axis, of the I-V plot, indicating close correlation between Ca^{2+} influx and charge transfer.

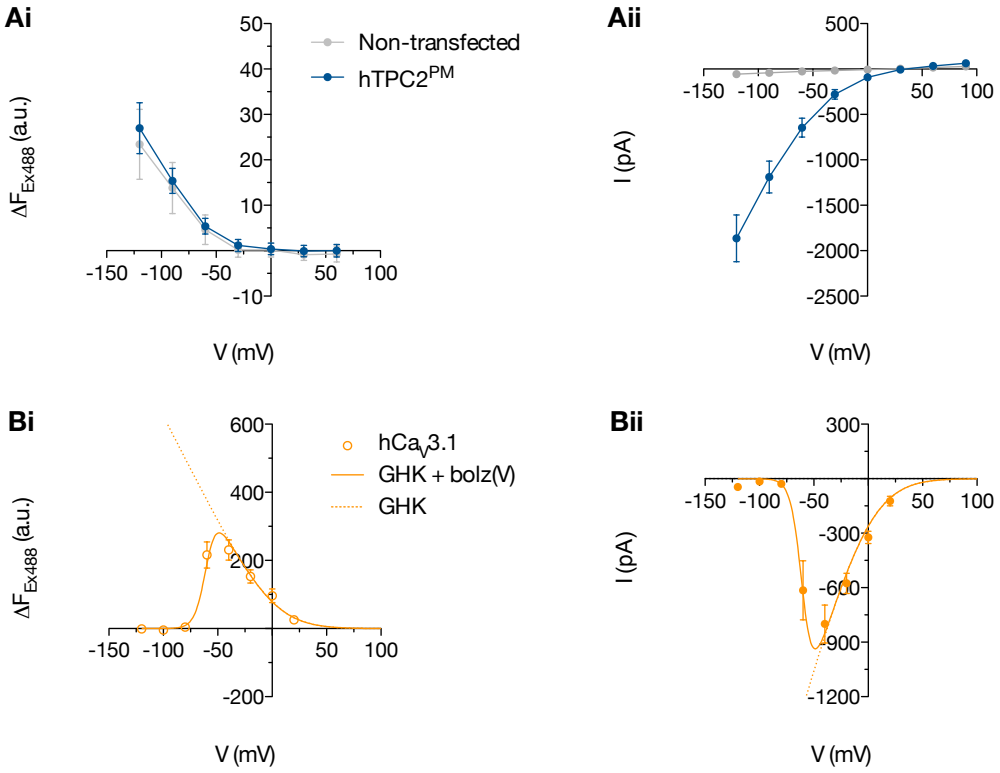

Figure 2.13 I-V and F-V relations of hTPC2^{PM} and hCa$_V$3.1

A. Paired (i) F-V and (ii) I-V curves recorded from non-transfected (grey) and hTPC2^{PM}-expressing HEK293 cells (n=7-8 for each). All experiments were performed at pH_o 6.5 in normal external solution.

B. Paired (i) F-V and (ii) I-V curves recorded from hCa$_V$3.1-expressing HEK293 cells (n=7). The data were fitted using the GHK current equation (eq.(2.2)) with a pure Ca^{2+} component scaled with a Boltzmann sigmoidal (P_o=1/(1+exp((V_{50}-V_m)/V_s))). The parameters were V_{50} = -60mV, V_s = 5mV, P_{Ca} = 6.8 x 10^{10}cm/s, $[Ca^{2+}]_o$ = 2mM and $[Ca^{2+}]_i$ = 100nM, T = 293K.

To obtain the F/Q ratios, we plotted the mean amplitude of the fluorescent changes <ΔF> against the mean charge transfer of the current (<Q>) (Figure 2.14A & B). From linear regression, we obtained the F/Q ratios as the slope of the regression line, which are 0.007634 ± 0.0005 for hTPC2^{PM}-expressing and 18.39 ± 0.6886 for hCav3.1-expressing cells. This is justified by that P_f changes minimally at extreme voltages

and that all of the observed fluorescent signals occurred only at extreme negative voltages. As leak currents accounted for most of the fluorescent signals observed in hTPC2^{PM}-expressing cells, it is difficult to estimate the true P_f from our data as it is very close to zero. After subtraction from the control, the P_f was estimated to be ~4.15 x 10^{-4}, which is ~0.04% (Figure 2.14B).

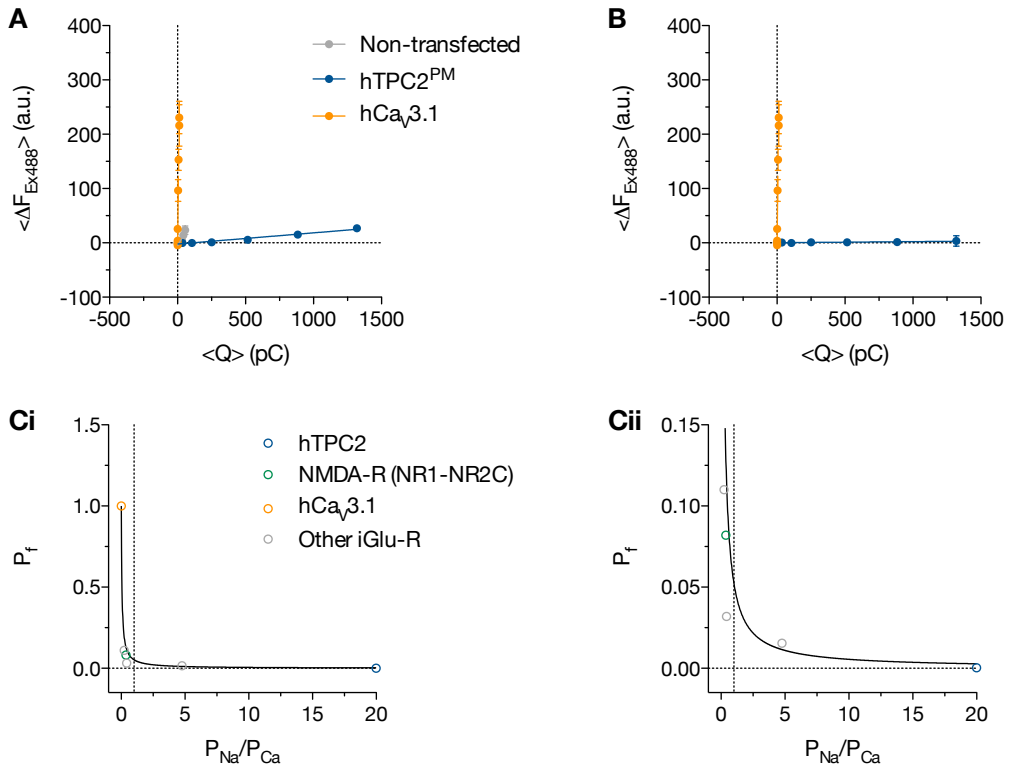

Figure 2.14 P_f (normalized F/Q ratio) of hTPC2^{PM} and relation with P_{Ca}/P_{Na}

A. <F>-<Q> plot comparing the F/Q relationship of non-transfected (grey), hTPC2^{PM}-expressing (blue) and hCa$_V$3.1-expressing (orange) cells.

B. Control-subtracted <F>-<Q> plot comparing the F/Q relationship of hTPC2^{PM}- (blue) and hCa$_V$3.1-expressing (orange) cells. From linear regression, the F/Q ratio is 0.007634 ± 0.0005 for hTPC2^{PM} and 18.39 ± 0.6886 for hCa$_V$3.1. The P_f of hTPC2^{PM} is therefore ~0.0004.

C. Relationship between P_f and P_{Na}/P_{Ca}, (i) original and (ii) expanded scale. Data points are experimental values of P_f given the P_{Na}/P_{Ca} obtained from bi-ionic reversal potentials. P_f of hCa$_V$3.1 is by default 1. Data points representing ionotropic glutamine receptors (iGlu-R) were published in Burnashev et al 1995. The blue data point represents the values obtained for hTPC2 in the current study. Line is prediction using a rearranged GHK current equation modeling a linear summation of I_{Na} and I_{Ca} (eq.(2.10)).

Figure 2.14Ci & Cii show the general relationship between P_f and P_{Na}/P_{Ca}. We found that the P_f-P_{Na}/P_{Ca} data for hTPC2 is consistent with the experimental trend observed in Burnashev et al 1995 [181]. The data were overlaid with prediction using a rearranged GHK current equation modeling the sum of parallel, independent I_{Na} and I_{Ca} (eq.(2.10)). It can be seen that the data can be well described by the model, despite the assumption of independence. Together, this indicates that the low P_f of hTPC2 is a direct consequence of its high Na^+ selectivity.

2.5.10 Permeation properties of hTPC2 do not support physiologically relevant Ca^{2+} influx

To conclude our data from a more quantitative perspective, we performed simulations using parameters and experimental records obtained in our study to investigate how the permeation parameters of hTPC2 may affect global and local $[Ca^{2+}]$. Figure 2.15A shows the simulation of a family of Ca^{2+} transients for hTPC2 with different P_f values modeled with the differential equation (eq.(2.13)) using the experimental hTPC2 current (Figure 2.12Bi) to drive ionic influx. It can be seen that, given a moderate buffering capacity κ_{endo} = 63 [189], the experimental ionic currents in Figure 2.12Bi was only able to give rise to a physiologically relevant Ca^{2+} transient *if* the P_f of a non-selective cation channel (NMDA-R) was used, but not that of hTPC2 (Figure 2.15A & B). This indicates that it is the P_f, which is ultimately governed by the physicochemical properties of the hTPC2 selectivity filter, that limits the ability of hTPC2 to generate global Ca^{2+} transients even when overexpressed and exposed to 2mM external $[Ca^{2+}]$ (lysosomal $[Ca^{2+}]$ is ~500μM).

We further investigated whether hTPC2 may be able to contribute to local Ca^{2+} signalling by examining the effect of its permeation properties on the hypothetical Ca^{2+} nanodomain. We modeled the Ca^{2+} nanodomain of a single channel using a

reaction-diffusion model with excess buffer approximation at equilibrium [190]. To visualize the Ca^{2+} nanodomain, we performed stochastic simulation according to the Ca^{2+} nanodomain model (Figure 2.16A). The plots in Figure 2.16A show the distribution of Ca^{2+}, which represents the stochastic position of individual Ca^{2+} ions at equilibrium. The physical size of the Ca^{2+} nanodomain is substantially larger for the NMDA-R than that for hTPC2, which is expected given the large ratio difference of $P_f \cdot i$ of the channels (~667-fold, see below for implications). Figure 2.16B shows the decay of the local Ca^{2+} domain in one-dimension as a function of radial distance from the channel pore. We can see that the amplitude of the NMDA-R Ca^{2+} nanodomain is much higher than that of hTPC2 (Figure 2.16B) while the decay, as expected from eq.(2.17), is not affect by the properties of the channel. To examine the minimal requirement for hTPC2 to function as a physiologically relevant Ca^{2+} source, we computed the Ca^{2+} nanodomain with varying P_f while fixing the unitary current of hTPC2. It can be seen in Figure 2.16C that, given the size of the unitary current of hTPC2, a P_{Ca}/P_{Na} of >1 at the minimum is required for hTPC2 to function as a physiologically relevant Ca^{2+} source, using the NMDA receptor as a reference. This corresponds to the complete loss of Na^+ selectivity, a requirement that is maybe unlikely to be realized.

Table 2.1 Parameters used in the Ca^{2+} nanodomain model

Parameter	Value	Units	Reference
Membrane potential	-120	mV	
P_f hTPC2	0.0004		this thesis (Ch.2)
P_f NMDA-R	0.082		[181]
γ hTPC2	10.5	pS	value at K_m (this thesis, Ch.3)
γ NMDA-R	51	pS	[192]
D_{Ca}	7.9×10^{-6}	cm^2s^{-1}	[177]
[endogenous Ca^{2+} buffer]	50	μM	[14]
k_{on}	6×10^6	$M^{-1}s^{-1}$	value of parvalbumin [14]

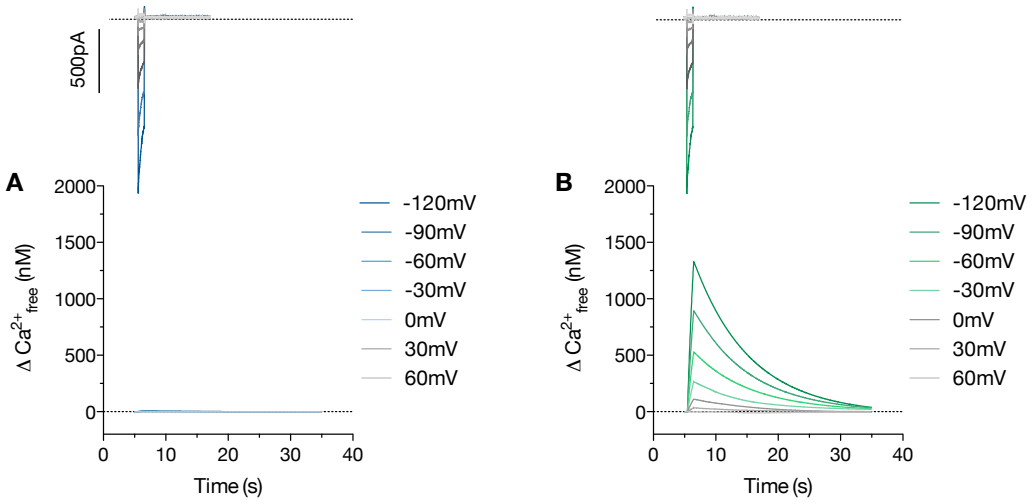

Figure 2.15 Impact of P_f on global Ca^{2+} transients

Family of global Ca^{2+} transients at different holding potentials modeled using a 1st order differential equation (eq.(2.13)), taking into account the effect of cytosolic buffering in the form of the buffering capacity (Neher and Augustine (1992) [188]). The experimental currents of hTPC2 (Figure 2.12Bi) were used to drive ionic fluxes and the decay time constant (τ = 9.3s) was also derived experimentally. P_f of the NMDA receptor channel was 8.2% and P_f of hTPC2 was 0.04% as estimated in this study. A moderate buffering capacity (κ_s = 63 [189]) was used. Traces for A) hTPC2 and B) the NR1-NR2C NMDA receptor channel are shown in blue and green respectively.

Finally, to investigate the probability that a Ca^{2+} sensor molecule will sample the minute space covered by the hTPC2 Ca^{2+} nanodomain, we computed the hemispherical volume of the Ca^{2+} nanodomains with $\Delta[Ca^{2+}]_{free}$ > 300nM (a concentration that we considered potentially competent for signalling, although we note that some common Ca^{2+} sensors function in the 1-10μM range [9, 198-200]). We can see in Figure 2.16D that the hemispherical volume decreases steeply, as a power of 3, with decreasing P_{Ca}/P_{Na}. For any given volume, this represents the fold-change in the probability that a Ca^{2+} sensor molecule will sample the signalling-competent volume, assuming homogeneous distribution of the sensor. This means that even when all the sensors are within the signalling-competent volume of a non-selective cation channel, the probability that the sensor will sample the signalling-competent volume of hTPC2 remains virtually zero (2×10^{-7}).

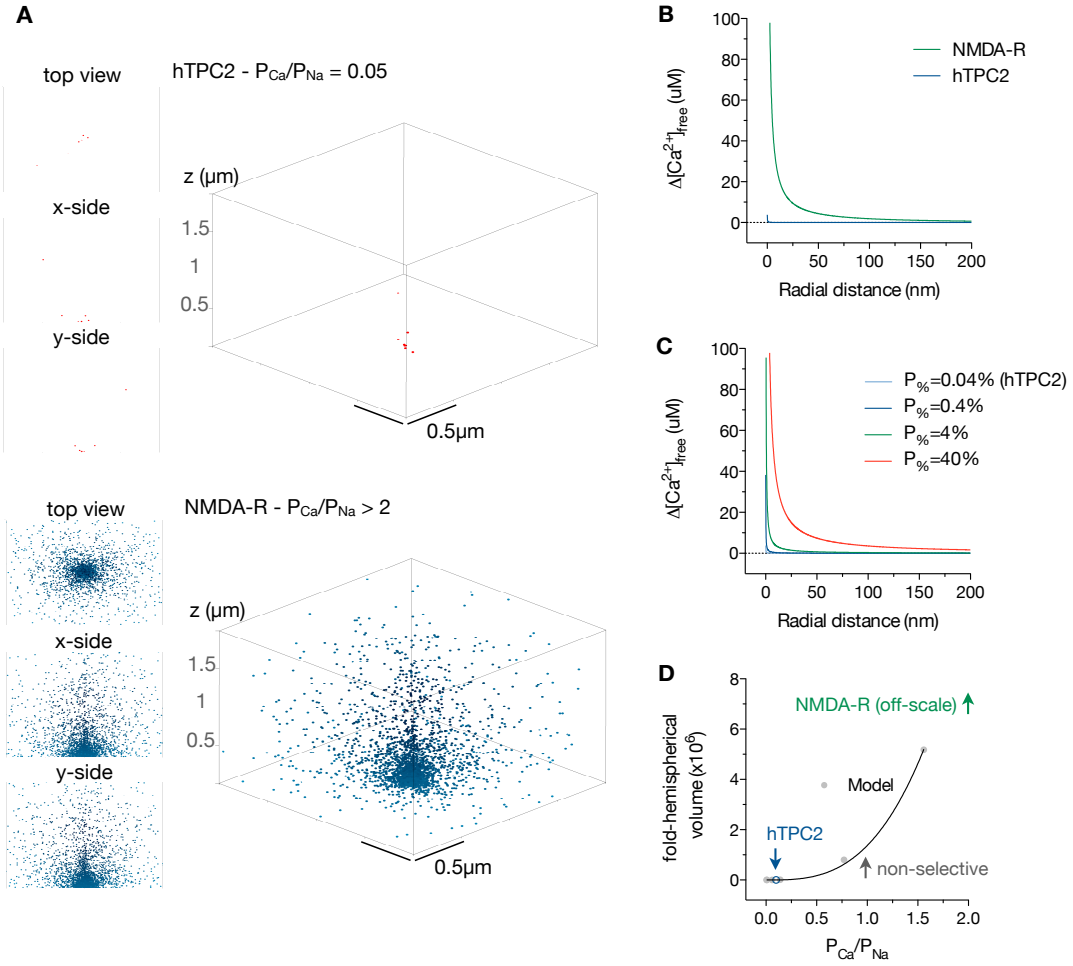

Figure 2.16 Impact of P_f on Ca^{2+} nanodomains

A. Three-dimensional visualisation of Ca^{2+} nanodomains of hTPC2 (top) and the NR1-NR2C NMDA receptor channel (bottom). Individual data points were computed from stochastic simulation using the Ca^{2+} nanodomain model described in the methods. For parameters, see Table 2.1.

B. Ca^{2+} nanodomain of hTPC2 and the NMDA receptor channel in one-dimension. P_f and i of hTPC2 were experimental values from this study. See Table 2.1 for details of other parameters.

C. Effect of varying P_f while fixing i on the hTPC2 Ca^{2+} nanodomain. Note that channel properties only contribute to the amplitude of the Ca^{2+} nanodomain.

D. Signalling-competent volume as a function of P_{Ca}/P_{Na}. Data points are hemispherical volume corresponding to their respective radial distances of $\Delta[Ca^{2+}]_{free}$ > 300nM obtained by varying P_{Ca}/P_{Na} in the simulation (eq.(2.16) & (2.17)). Line is empirical fit using eq.(2.18).

2.6 Discussion

Here, we performed detailed electrophysiological characterization of hTPC2. We found that, under our conditions, hTPC2^{PM} functions as a H^+-activated Na^+ channel capable of conducting Na^+ at the lower physiological range. We also estimated the fractional Ca^{2+} current through hTPC2 to be close to zero under normal extracellular conditions, which, most importantly, is consistent with a P_{Ca}/P_{Na} of 0.05 Moreover, we modelled global Ca^{2+} transients and nanodomains using the experimentally derived permeation parameters of hTPC2 and found negligible role for hTPC2 to directly function as a physiologically relevant Ca^{2+} source.

From bi-ionic reversal potential measurements, the permeability sequence of hTPC2^{PM} was found to be Na^+ (1) ≥ Li^+ (0.9) >>> K^+ (0.06) > Cs^+ (0.03) > $NMDG^+$, similar to that of the voltage-gated Na^+ channels in nerves and represents one of the Eisenman permeability sequence [201]. A qualitative agreement between the permeability sequence with one of the Eisenman sequence suggests that ion conduction through hTPC2^{PM} is consistent with the simplified quantitative picture of the energetics associated with ion transfer to channel's selectivity filter from the bulk aqueous solution.

Our metric of defining ion selectivity is based on P_X/P_{Na} from the GHK voltage equation, which has some inherent assumptions for example independent ion movement. We feel that this assumption is not too offensive as simpler forms of ion interaction models, i.e. non-independence, leads to the same definition of flux ratio as in the logarithmic term of the GHK voltage equation. For example, as can be seen in the following chapter (section 3.5.7), two competing ions following a Michaelis-Menten-type permeation in opposite direction leads to a flux ratio that is equivalent to that used in the GHK voltage equation, i.e. classical definition of relative

permeability. As in many cases, the GHK voltage equation is very well followed, which adequately describes the shift in E_{rev} as a function of external [ion] (Figure 2.8B, Figure 2.11B and data not shown for Li^+ and K^+). However, higher ion interaction models are not expected to yield the equivalent $P_X[X]_o/P_{Na}[Na]_i$ expression as multiple binding steps and multiple permeating configurations all need to be taken into account and may deviate from the GHK expectation. Thus, the use of the GHK voltage equation and P_X/P_{Na} is justified if the degree of dependence is low and/or experimentally verified. Essentially, the assumption of the sum of independent currents may be thought of as fixed populations of channels (as defined by their K_M with competition accounted for) each permeating their respective ions with different rates at quasi-steady state.

Ion permeation through hTPC2 appears to be insensitive to external pH, which may play a crucial role for hTPC2 function. From our data, the Nernstian behavior of $[Na^+]$ dependence of reversal potential at pH_o 5.5 suggests negligible interference by the sizable proton gradient that was present (Figure 2.8A & B). Stationary noise analysis using data pooled from various pH_o conditions (Figure 2.5D) also suggests that the single-channel Na^+ current of hTPC2 does not seem to exhibit sensitivity to pH_o changes, i.e. a well-defined slope close to zero <I>. These data may suggest that, unlike some Na_V channels [202], the hTPC2 selectivity filter may not contain titratable residues. The different design in the selectivity filter of hTPC2 may be particularly suited for its lysosomal localization as the lysosomal lumen is highly acidic (pH_o 4.60), which may ensure minimal interference by lysosomal protons and thus may serve to preserve this Na^+ conductance.

We note that the controversy concerning the permeation properties of hTPC2 lies 1) between macroscopic and single-channel studies (Ch.1, Table 1.1 & Table 1.2), and 2) the observation of anomalous Ca^{2+} influx claimed to be through hTPC2. Notably,

a similar situation is also true for studies that investigate the permeation properties of hTPC1 [156, 161, 162].

A possible reason for this discrepancy is that two different approaches have been used - blind recording from randomly selected samples known to express hTPC2 but of partial purity and selective recording of single membrane entities known to express hTPC2 judged by fluorescence. Unlike organelle isolation methods where lysosomes are almost always co-purified with mitochondria and peroxisomes due to similar densities, overexpression on the normally electrically quiescent membrane of HEK293 cells is advantageous as the ionic current of interest can be studied in isolation without contamination from endogenous currents. The approach used here is therefore best suited in characterizing novel ion channels especially when their pharmacology and permeation properties *have been unknown* and eliminates the uncertainty that arises when using mixed organelles/proteins preparations.

One obvious note is perhaps on the purification procedure itself. It has not been determined whether the detergent used, CHAPS in this case [162, 164], may maintain the stability of the channel in solution. In one case, TPC2 was 'purified' using *anti-serum* [164], which may not be the purist method of isolating the channel of interest. Western blot may show the presence of the channel [162, 164], but probably does not indicate purity. Likewise, fluorescence image may show the presence of a GFP-tagged lysosomal marker thereby indicating the presence of isolated lysosomes [163], but probably does not indicate purity.

Some inherent assumptions are also present in bilayer experiments where single channels have to be incorporated into the lipid bilayer, aside from preparation purity and its anecdotal nature. As the channel is incorporated into the lipid bilayer under a K^+ gradient in most cases, any channel that is seen incorporated will by default be a K^+-permeable channel, which is not the case for TPCs. Incorporation is

also mostly done at voltages not beyond +/-30mV, any channel that is seen incorporated will by default be a relatively high conductance channel. The presence of these experimental criteria before any observations are made means that, despite its strength in resolving single-channel kinetics, this technique may not be suitable for characterizing novel ion channels as evidently shown in the TPC case.

We note that patch-clamp recording is inherently subjected to a set of predefined conditions as the channel of interest inevitably sits in a membrane with potentially function-modifying lipid components. For example, although the overall membrane content, e.g. phosphatidylcholine, phosphatidylethanolamine, are very similar between lysosomes and the plasma membrane, differences have been observed, for example cholesterol content and different phosphoinositide isoforms that in part mark the identity of their resident membranes [203, 204]. In some cases, vacuolin is also used to yield recordable large endomembrane structures [156, 157, 159], which may induce non-native membrane curvature and/or composition, although vacuolin itself is usually not acutely present during the recording. Nonetheless, these limitations equally apply to patch-clamp recordings of single-channels and crucial components that may regulate TPC2 in a manner as robust as $PI(3,5)P_2$ and external protons, or abruptly change the channel properties have yet to be identified.

Despite the above concerns, it appears that patch-clamp studies recording macroscopic current of hTPC2 have all agreed on that hTPC2 is a Na^+-selective channel [157-160], regardless of the membrane environment and the LL/AA mutation, and our data are in line with this conclusion (Table 1.1). This consistent result obtained from macroscopic current measurement, which reflects the properties of a population of channels, is also in contrast to the heterogeneous results obtained from single-channel studies [152, 161, 162, 164]. The inconsistency between the permeation characteristics of the putative NAADP-activated single-

channel currents and the macroscopic TPC2 currents may suggest the need to revise the groundbreaking proposal that TPC2 may be the *bona fide* target of NAADP.

Another important controversial issue is the observation of anomalous Ca^{2+} influx associated with hTPC2 expression reported in two previous studies [152, 159]. Although Brailoiu et al 2010 [152] reported Ca^{2+} current through hTPC2, it is surprising that 1) such claim was based on a single voltage-step, thus 2) no I-V relationship was reported, and 3) nor did Ca^{2+} dependence of the reversal potential and rectification were examined. Importantly, their recording condition was symmetrical 140mM Ca^{2+} - a reversal potential of 0mV is usually avoided and is often a concern as without rigorous ion substitution experiments, it can be difficult to distinguish channel currents from seal leak, especially when patch stability can become problematic as 140mM Ca^{2+} was present in the internal solution. Similarly, Jha et al 2014 [159] did not report a coherent relationship between Ca^{2+} current and influx.

It is intuitive that the origin of Ca^{2+} influx is the conduction of Ca^{2+} ions through open channels and thus its dependence on the fractional Ca^{2+} current (eq.(2.13)), which is in turn governed by P_{Ca}/P_{Na} (eq.(2.10)). Rigorous characterization of the P_{Ca}/P_{Na} is therefore essential to validate the notion that the observed Ca^{2+} transient may be due to Ca^{2+} going through hTPC2.

We attempted to readdress these issues here by 1) performing rigorous ion substitution experiments, and by 2) estimating the fractional Ca^{2+} current, which was crosschecked with the determined P_{Ca}/P_{Na}, where both were further checked with the classical theory of electrodiffusion. By examining the relationship between E_{rev} and $[Ca^{2+}]_o$ in the absence of competing ions, we obtained a P_{Ca}/P_{Na} of 0.05 (Figure 2.11B). Also, by using supraphysiologically high $[Ca^{2+}]_o$ (Figure 2.11, 10mM and 100mM), we observed $[Ca^{2+}]_o$-dependence of the rectification, although still

negligible compared to the Na^+ current. Further, through examination of the F-V and I-V relations (Figure 2.13), we were able to rule out the possibility that charge transfer through the large hTPC2 current could give rise to experimentally observable Ca^{2+} influx. Most importantly, the estimated fractional Ca^{2+} current and the P_{Ca}/P_{Na} are in line with existing data and the theory of electrodiffusion, validating our experimental approach and data.

In addition to experimental approach, we examined how the P_f value may affect Ca^{2+} signalling using a modeling approach. Our data suggest that, unlike the non-selective pore of NMDA-R, the high P_{Na}/P_{Ca} of hTPC2, together with its relatively low unitary conductance, ensures low-enough Ca^{2+} leakage and the consequential formation of a defective Ca^{2+} nanodomain at the hTPC2 pore. Our data therefore make instant discrimination of hTPC2 from non-selective cation channels, which are known to and able to participate in Ca^{2+} signalling, but suggest a possible electrical rather than a biochemical role for hTPC2. Although we cannot rule out the contribution of auxiliary subunits that may change the permeation properties of hTPC2, the possibility that this may allow hTPC2 to signal Ca^{2+} is maybe unlikely to be realized since the minimal requirement corresponds to the complete loss of Na^+ selectivity.

We note that our, or any, modeling data are subjected to potential errors in parameter estimation. As the Ca^{2+} nanodomain model depends relatively heavily on P_f·i, accurate measurement of these parameters is crucial. We note that our estimation of i is not unambiguous and can vary within 5-fold as $P_{o\,max}$ decreases from 0.5 to 0.1 (denominator of eq.(2.5)) and thus represents a possible source of error. However, the occurrence of this error means that we are only likely to have overestimated the amplitude of the TPC2 Ca^{2+} nanodomain as the estimated i will be 5-fold smaller if a $P_{o\,max}$ of 0.1 was used ($P_{o\,max}$ of 0.5 was used in our calculation). In fact, P_f is a more dominant parameter as it can vary within two to three orders of

magnitude due to its sensitivity to changes in P_{Ca}/P_{Na} (Figure 2.14C). Thus, given the relatively accurate measurements we have taken for estimating the P_f of TPC2 and its experimental agreement with P_{Ca}/P_{Na} (Figure 2.14C), we feel that our modeling data remain a good approximation. Nevertheless, further efforts using more detailed models would certainly be beneficial.

Consistent with others [157-160], we found lack of observable effect of NAADP on the hTPC2^{PM} current (Figure 2.6). We also found no observable Ca^{2+} transients when NAADP was dialyzed into hTPC2-stable HEK293 cells in the whole-cell configuration (Figure 2.1), which is in line with our Ca^{2+} titration (Figure 2.11) and fractional Ca^{2+} current experiments (Figure 2.12 & Figure 2.13) and is most readily explained by the lack of Ca^{2+} permeability of hTPC2 at lysosomal [Ca^{2+}]. Significant loss of potential NAADP-binding proteins seems not plausible, as the loss of proteins, which have very high molecular weight, would be much slower than the influx of small molecules like NAADP [194]. These data suggest that although TPC2 may be required for NAADP-induced Ca^{2+} release, recombinant expression of TPC2 alone is unable to recapitulate phenomena observed in pseudo-native preparations and suggests that additional components may be required.

Our observation that hTPC2^{PM} can be activated by H^+_o, however, differs from other studies showing that $PI(3,5)P_2$ is essential for the activation of hTPC2 [157-160]. This does not appear to be caused by plasma membrane targeting as Wang et al 2012 [157] observed $PI(3,5)P_2$ sensitivity and NAADP insensitivity in their LL/AA mutant and the same was observed for hTPC2 expressed in plant vacuoles [160]. One observation is that activation of plasma membrane-targeted hTPC2 may require higher levels of $PI(3,5)P_2$ than in lysosomes [157, 159]. A scenario akin to the BK_{Ca} channel where voltage and Ca^{2+} exert their co-stimulatory effects is also possible [205]. Nevertheless, hTPC2 seems to remain Na^+-selective despite the presence of the different stimuli.

2.7 Conclusion

This is the first study applying simultaneous electrophysiological and fluorescence measurements with quantitative analysis to examine the Ca^{2+} permeability of TPC2. Our data have illustrated the biological extremes of the consequences of ion selectivity by contrasting the F/Q relationship of a highly Ca^{2+}-selective channel ($Ca_V3.1$) and a Na^+-selective channel (TPC2). Our data have also shown that hTPC2 and other Na^+-selective channels are unlike non-selective cation channels in that they do not, and cannot, function as physiologically relevant Ca^{2+} source. Suggestion of similarity in terms of Ca^{2+} permeation between the two therefore appears to be quantitatively inappropriate. Our study, together with other patch-clamp studies [157-160], therefore raises concern over studies that claim the observation of NAADP-induced Ca^{2+} release in recombinant expression systems upon overexpression of hTPC2 [65, 99, 132, 152, 176]. Importantly, our data highlight the natural consequence of matter conservation - low P_{Ca}/P_{Na} results in low P_f thus negligible Ca^{2+} influx and signalling probability. The lack of further selection pressure may explain the rarity of mammalian ion channels with even higher Na^+ selectivity, which may further imply the negligible nature of the inevitable Ca^{2+} leakage through channels with P_{Ca}/P_{Na} of ~0.1, including hTPC2.

3 Ion-binding selectivity & conduction mechanisms in hTPC2

3.1 Abstract

The permeation pathway of hTPC2 (human two-pore channel 2) was studied using a plasma membrane-targeted hTPC2 ($hTPC2^{PM}$) and the tetravalent cation spermine. We found that intracellular spermine blocks $hTPC2^{PM}$ (K_d~1mM) via a bi-molecular mechanism and displays intrinsic voltage sensitivity under zero extracellular Na^+ condition. Extracellular Na^+ decreases the observed binding energy of spermine, which allowed the determination of equilibrium dissociation constant of the responsible binding site. The contribution of extracellular ions to the effective valence of spermine block suggested that this binding site is located within the voltage field, likely at the selectivity filter external to the spermine-binding site. By analysing the shifts in spermine binding energy, we arrived at the following sequence of equilibrium ion selectivity (K_d) of this binding site: Li^+ (0.54mM) < Na^+ (3.1mM) < K^+ (18.8mM) < Cs^+ (81.2mM) and Ba^{2+} (5.7mM) ~ Ca^{2+} (6.6mM) < Mg^{2+} (80.7mM); which contrasts with the electrophysiological selectivity sequence: Na^+ (1) ≥ Li^+ (0.94) >> Ca^{2+} ~ Ba^{2+} (0.04) ≥ K^+ (0.03) ≥ Cs^+ (0.02) ≥ Mg^{2+} (<0.02). We found that Li^+ and Na^+ permeation exhibit K_M values higher than their respective K_d's, which indicates a second ion-binding event that leads to ion permeation, while Ca^{2+} displays only one affinity and a very low ion conduction rate. This implies a knock-on mechanism of Li^+ and Na^+ permeation and that failure to establish a knock-on-permissive multi-ion configuration may be one of the mechanisms that prevents Ca^{2+} from permeating at a physiologically significant rate.

3.2 Introduction

The low relative permeability of K^+ and Ca^{2+} suggests, in the classical definition of P_X/P_{Na}, that K^+ and Ca^{2+} likely experience a large energy barrier when passing through the channel than that experienced by Na^+ (relative to the bulk) [177]. The classical assumptions are however not very realistic and the parameter P_X/P_{Na} gives no information as to whether ions may bind selectively at the selectivity filter. Hence, whether K^+ and Ca^{2+} may bind at the selectivity filter is not known, as with other impermeant ions. Here, we used intracellular spermine block to study equilibrium selectivity by systematically determining the K_d of various group I and II ions. Our results suggest that electrophysiological selectivity does not necessarily reflect equilibrium selectivity and that kinetic factors and the ability to establish a multi-ion configuration both appear also to be fundamental in the generation of Na^+ selectivity in hTPC2.

3.3 Methods

3.3.1 Cell culture and construct expression

HEK293 cells (ECACC) were cultured in DMEM (Sigma) supplemented with 1% penicillin-streptomycin-L-glutamine (Sigma) and 10% FBS (Sigma), and were maintained in a humidified atmosphere containing 5% CO_2. LL/AA hTPC2.mCh (Ch.2) were transiently transfected into HEK293 cells using the standard calcium phosphate precipitation method as described in Ch.2. Recordings were performed 24-48hrs post-transfection.

3.3.2 Electrophysiology

Whole-cell voltage-clamp recordings [183] were made on HEK293 cells expressing hTPC2^{PM} using the Axopatch 200B amplifier controlled by the Clampex 10.3 software communicated through Digidata 1322A (Molecular Devices). Borosilicate patch pipettes (Harvard apparatus or Sutter) were fire-polished using a microforge (Narishige) and had 3-6MΩ resistances when filled with standard pipette solutions. Seals are typically 10-20GΩ before breaking in. Raw signals were analog-filtered through a 4-pole Bessel low-pass filter with a cutoff frequency of 5kHz. Sampling frequency was 10kHz. Data for display and plotting I-V curves were filtered offline with a Gaussian low-pass filter at a cutoff frequency of 250Hz. Data used for kinetic measurements were filtered offline with a Gaussian low-pass filter at a cutoff frequency of 1kHz. All plotted voltages were corrected for liquid junction potential according to [184] and was calculated in the Clampex 10.3 software. All the recordings were made under bi-ionic conditions unless otherwise stated. All recordings were performed at least 5 minutes after break-in to ensure complete dialysis of spermine and other blockers into the cell, which was confirmed by monitoring the time course of current decay using a voltage ramp protocol. I-V plots were obtained strictly using the indicated voltage step protocol and were constructed by measuring current amplitude at the end of each voltage pulse in Clampfit (Molecular devices). Typically, the voltage step protocol was repeated at least 3-5 times for averaging purposes to obtain smooth I-V plots.

3.3.3 Solutions

Bi-ionic monovalent external (mM):

140 X($MeSO_3$), 5 XCl, 5.5 D-glucose, 25 MES, pH 5.50

where X corresponds to $NMDG^+$, Na^+, Li^+, K^+ or Cs^+.

Bi-ionic divalent external (mM):

100 $Mg(SO_4)_2$, 2.5 $MgCl_2$, 5.5 D-glucose, 25 MES, pH 5.50

100 $Ca(MeSO_3)_2$, 2.5 $CaCl_2$, 5.5 D-glucose, 25 MES, pH 5.50

100 $Ba(MeSO_3)_2$, 2.5 $BaCl_2$, 5.5 D-glucose, 25 MES, pH 5.50

Bi-ionic Na^+ internal (mM):

125 $Na(MeSO_3)$, 20 NaCl, 1 EDTA, 25 HEPES, pH 7.20 (for spermine & spermidine)

125 Na-gluconate, 20 NaCl, 1EGTA, 4.875 $MgCl_2$, 25 HEPES, pH 7.20 (for Mg^{2+}, free $[Mg^{2+}] = 3mM$)

For titration experiments, concentration was varied by mixing X^+ with $NMDG^+$ bi-ionic solutions at the desired ratio. For ions whose $MeSO_3$ salts are not available, the solutions were made using the corresponding hydroxide and titrated with $MeSO_3H$. This ensures charge balance in the solution as the amount of $MeSO_3H$ added matches up with the concentration of the cation-hydroxide. This was experimentally verified by calculating the final concentration of $MeSO_3^-$ after titration. All external solutions were titrated to the desired pH using 1M hydroxide solution of the inert and impermeant ion $NMDG^+$ ($NMDG^+$-OH^-) in order to keep the concentration of the test ion unchanged. Internal solution was titrated to the desired pH using NaOH to ensure that the only cations present are Na^+ and the test blocker.

3.3.4 Homology modeling and energy minimization

A homology model of the hTPC2 pore was constructed using Modeller 9.13 [206] using NavMs (PDB entry: 3ZJZ) in an open state [207] as the structural template. The first pore domain (S5-S6) was modeled using chain A and C and the second pore domain (S11-S12) was modeled using chain B and D. A short stretch of the external loop between the S11 helix and the pore helix (see supplementary) was removed due to poor loop modeling as a result of lack of homology region. Sequence

alignment was performed with EMBOSS which uses the Needleman-Wunsch algorithm (http://www.ebi.ac.uk/Tools/psa/emboss_needle/). The alignments agree well with secondary structure predictions where helices and pore-loops are aligned with their counterparts without manual interventions and can be found in the supplementary in this chapter.

The individual hTPC2 models generated by Modeller were assembled as tetramer using MacPymol, embedded in a preformed POPC bilayer and solvated in a water box at 150mM NaCl using VMD [208]. The periodic boundary system had dimensions of 77Å x 77Å x 77Å. The system was energy-minimized for 1000 steps at 2fs/step and was further equilibrated for 250pS using NAMD2.10 [209] with CHARM22 force field [210] and TIP3P water model in an NPT ensemble (constant pressure and temperature) at 310K. Electrostatic interactions were computed using the particle mesh Ewald algorithm. The RMSD of the structure after equilibration was 1.58Å with reference to the initial energy-minimized structure and is close to equilibrium.

3.3.5 *In silico* docking

In silico docking was performed using a fully charged (4+) spermine molecule and the energy-minimized structure of the hTPC2 model using Autodock Vina [211]. The grid for dock search had dimensions of 18Å x 18Å x 34Å and was centered at (0, 0, -8). The center of geometry of the hTPC2 model was (0, 0, 1.3), thus the grid overlaps with the aqueous cavity. Docking was performed 5 times and the top twenty poses (-3.5 to -3.8 kcal/mol) from each run were extracted. Center of mass were calculated for all 100 poses in VMD and were used to construct probability density distributions in X, Y and Z (axes) relative to that of the hTPC2 model to identify low-energy spermine binding regions.

3.4 Data analysis

3.4.1 Determination of permeability ratios

The bi-ionic permeability ratio was calculated by

$$E_{rev} = \frac{RT}{F} \cdot \ln\ (P_X / P_{Na}) \tag{3.1}$$

where E_{rev} is the reversal potential, R, T and F have their usual thermodynamic meanings.

For divalent ions, the shift of E_{rev} by the external ion is modeled as a sum of independent currents were used,

$$I_{total} = I_{Na} + I_{divalent} + I_{leak}$$

$$I_i = z_i^2 \cdot F \cdot P_i \cdot D \cdot \frac{[ion]_{i,o} - [ion]_{i,i}\, e^{z_i \cdot D}}{1 - e^{z_i \cdot D}} \tag{3.2}$$

where D = VF/RT, z is the valence, V is the membrane potential, $[ion]_{i,i/o}$ indicates the i^{th} ionic species inside or outside, P is the absolute permeability of the i^{th} ionic species.

3.4.2 Determination of voltage dependence

Although all families of data were fitted using the models detailed below, it is nevertheless useful to quantify the observed ΔG for each voltage dependence curve

for systematic analysis of the effect of a third experimental variable such as blocker and ion concentrations. We use the following form of the Boltzmann equation [212]

$$Fraction\ unblocked = \frac{1}{1 + \exp\left(\frac{\Delta G_{obs} + zVF}{RT}\right)} \tag{3.3}$$

where ΔG_{obs} is the free energy difference between an initial and a final states, z is the effective valence, V is the voltage, and R, T, F have the usual thermodynamic meanings. Using this form, and by comparison with the voltage dependence equations below, it can be seen that ΔG_{obs} is often the sum of ΔG_{spm} and a function corresponding to the third experimental variable, allowing the quantification of the effect of this latter variable.

The voltage dependence of the I-V curves were obtained by fitting with the GHK current equation modified with the above Boltzmann equation

$$I_{total} = I_{leak} + f(V)\cdot I_{Na}$$
$$I_{total} = I_{leak} + f(V)\cdot (I_{Na} + I_{divalent})$$

$$I_{total} = g_{leak} \cdot V + \frac{1}{1 + \exp\left(\frac{\Delta G_{obs} + zVF}{RT}\right)} \cdot \sum {z_i}^2 \cdot F \cdot P_i \cdot D \cdot \frac{[ion]_{i,o} - [ion]_{i,i}\, e^{z_i \cdot D}}{1 - e^{z_i \cdot D}} \tag{3.4}$$

where g_{leak} is the leak conductance and all other symbols indicate the same quantities as those described in eq.(3.2) and eq.(3.3). ΔG_{obs}, z, P and g_{leak} are free parameters that are fitted. Fixed parameters are independent variables of the experiments, which include valence of the ion and [ion] present in the external and internal solutions. In general, g_{leak} is very small as E_{rev} was used to reject leaky patches.

3.4.3 Spermine block model

Spermine (spm) block was analyzed using a bi-molecular interaction model where a spermine molecule penetrates fully into the aqueous cavity of the channel but not into the selectivity filter (Scheme 3.1). The voltage profile assigned to the channel is based on the voltage profile calculated using Poisson-Boltzmann electrostatics on channels whose structures have been experimentally determined [213-217]. Therefore, this model refines previously used models [218, 219] by incorporating intrinsic voltage sensitivity of the blocker, extrinsic voltage sensitivity due to selectivity filter ion occupancy and a realistic voltage profile. It is assumed that the voltage drop across the channel is

$$V_m = V_{selectivity\ filter} + V_{aqueous\ cavity} \tag{3.5}$$

which correspond to the voltage drop across the channel, selectivity filter (SF) and the aqueous cavity respectively. The voltage drop across the latter components are approximated as linear.

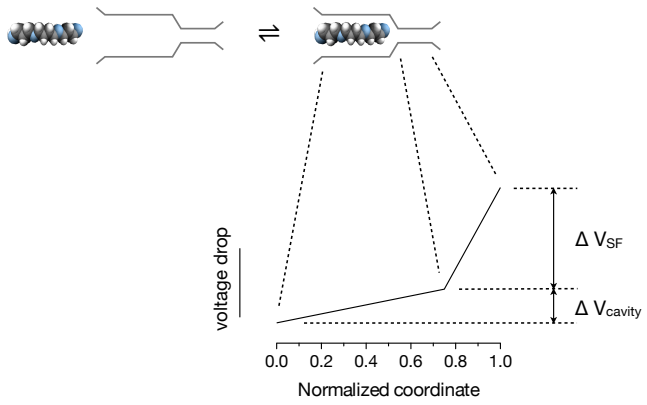

Scheme 3.1 Spermine block model

This model gives the following expression at equilibrium

$$Fraction\ unblocked = \frac{1}{1 + \exp\left(\frac{\Delta G_{spm} + (-RT \cdot \ln[spm]) + \left[-z_{spm} f_{spm}(1 - \delta_{SF})VF\right]}{RT}\right)} \tag{3.6}$$

where ΔG_{spm} is the free energy change corresponding to the free and spermine-bound states, z_{spm} is the valence of spermine (4+ at neutral pH), f_{spm} is the fractional penetration into the cavity, which is assumed to be 1, δ_{SF} is the voltage drop across the selectivity filter. This arranged form shows that the energetic contribution can be decomposed into the intrinsic energy difference between the free and bound states, the effect of altering [spermine] and voltage as a sum of the individual components. The observed ΔG (ΔG_{obs}), in comparison with eq(3.3), is shifted by increasing concentration of spermine, which is given by

$$\Delta G_{obs} = \Delta G_{spm} - RT \cdot \ln[spm] = RT \cdot \ln\left(\frac{K_d}{[spm]}\right) \tag{3.7}$$

where K_d is the equilibrium dissociation constant of spermine at zero voltage.

The time constant of block (τ_{block}) is given by

$$\tau_{block} = \frac{1}{[spm] \cdot k_{on} \cdot \exp\left(\frac{z_{spm} f_{0\to TS}(1 - \delta_{SF})VF}{RT}\right) + k_{off} \cdot \exp\left(-\frac{z_{spm}(1 - f_{0\to TS})(1 - \delta_{SF})VF}{RT}\right)} \tag{3.8}$$

where f_{0_TS} is the fractional distance from the pore entrance to the transition state (where the highest energy barrier is encountered) and $k_{on/off}$ are the rate constants of binding and unbinding respectively.

3.4.4 Ion-spermine allosteric interaction model

The functional interaction between the external ion of interest and internal spermine was analyzed using an allosteric model where spermine binds at the cavity and the external ion binds at the selectivity filter (Scheme 3.2). Mutually exclusive binding was not assumed initially but was often found to be the case. At equilibrium,

$$Fraction\ unblocked = \frac{1+\frac{[ion]}{K1\cdot\exp\left(\frac{z_{ion}f_{ion}\delta_{SF}VF}{RT}\right)}}{1+\frac{[ion]}{K1\cdot\exp\left(\frac{z_{ion}f_{ion}\delta_{SF}VF}{RT}\right)}+\frac{[spm]}{K3\cdot\exp\left(-\frac{z_{spm}f_{spm}(1-\delta_{SF})VF}{RT}\right)}+\frac{[ion]}{K1\cdot\exp\left(\frac{z_{ion}f_{ion}\delta_{SF}VF}{RT}\right)}\cdot\frac{[spm]}{K3\cdot\exp\left(-\frac{z_{spm}f_{spm}(1-\delta_{SF})VF}{RT}\right)}} \quad (3.9)$$

where the symbols have the same meanings as those employed in eq.(3.3) and the subscript ion indicates the same quantity but corresponding to the ion. K1-4 are the K_d of the ligand in the corresponding binding reactions.

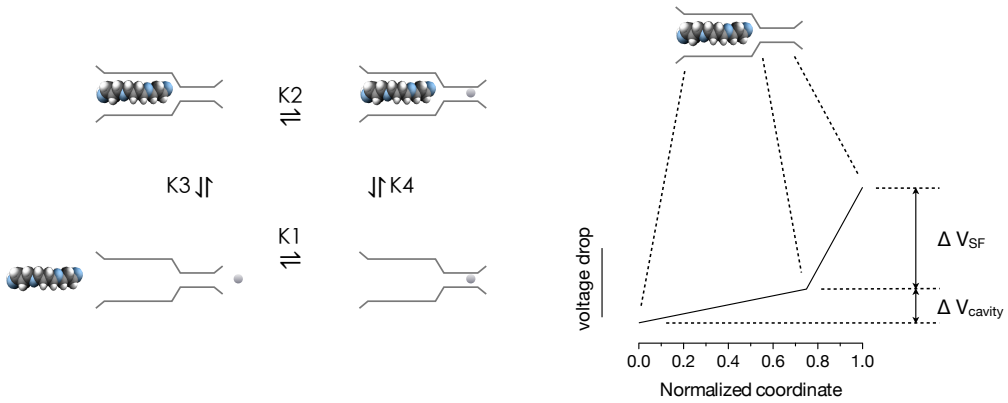

Scheme 3.2 Ion-spermine allosteric interaction model

For analysis of [ion]-dependent shifts in ΔG_{obs}, a reduced model, where the dually bound state is omitted, is used.

$$Fraction\ unblocked = 1 - \frac{1}{1 + \exp\left(\frac{\Delta G_{spm} + (-RT \cdot \ln[spm]) + RT \cdot \ln\left(1 + \frac{[ion]}{K1 \cdot \exp\left(\frac{z_{ion} f_{ion} \delta_{SF} VF}{RT}\right)}\right) + \left(-z_{spm} f_{spm} (1 - \delta_{SF}) VF\right)}{RT}\right)} \tag{3.10}$$

Therefore, increasing [ion] shifts the ΔG_{obs} by

$$\Delta G_{obs} = \Delta G_{spm} + RT \cdot \ln\left(\frac{[ion] + K1 \cdot \exp\left(\frac{z_{ion} f_{ion} \delta_{SF} VF}{RT}\right)}{K1 \cdot \exp\left(\frac{z_{ion} f_{ion} \delta_{SF} VF}{RT}\right) \cdot [spm]}\right) \tag{3.11}$$

For analysis, the voltage was set to zero.

At saturating [ion], the ionic term effectively becomes

$$RT \cdot \ln\left(1 + \frac{[ion]}{K1 \cdot \exp\left(\frac{z_{ion} f_{ion} \delta_{SF} VF}{RT}\right)}\right) \approx RT \cdot \ln\left(\frac{[ion]}{K1 \cdot \exp\left(\frac{z_{ion} f_{ion} \delta_{SF} VF}{RT}\right)}\right) \tag{3.12}$$

$$\approx RT \cdot \ln\left(\frac{[ion]}{K1}\right) + RT \cdot \frac{-z_{ion} f_{ion} \delta_{SF} VF}{RT} \tag{3.13}$$

Therefore, at saturating [ion], the observed effective valence (z_{eff}) is the sum of z_{spm} and z_{ion}.

$$voltage\ dependence = z_{spm} f_{spm} (1 - \delta_{SF}) VF + z_{ion} f_{ion} \delta_{SF} VF \tag{3.14}$$

$$z_{eff} = z_{spm} f_{spm} (1 - \delta_{SF}) + z_{ion} f_{ion} \delta_{SF} \tag{3.15}$$

This contributes to the observed increase in z_{eff} as [ion] increases to saturation in all ionic species tested.

3.4.5 MWC model for ion-conduction

The conductance-$[ion]_o$ relation was modeled using a MWC model (Scheme 3.3) where the selectivity filter displays certain tendency to alternate between a conducting and a non-conducting mode (Y_0, $[R_0]/[T_0]$).

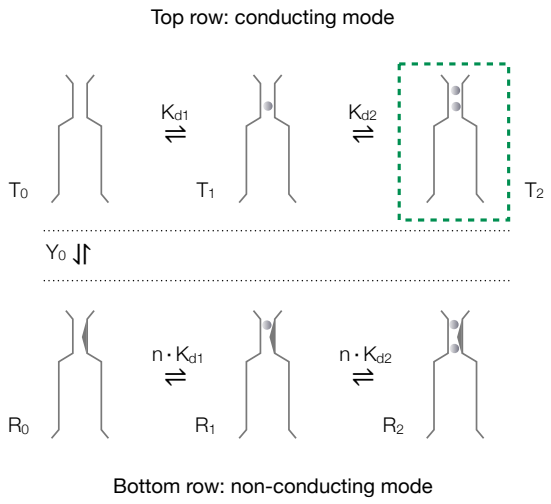

Scheme 3.3 MWC model for ion-conduction

The conducting mode (T) binds ion with affinity close to experimental values (K_{d1} and K_{d2}) while the non-conducting mode (R) binds ion with low affinity and is expressed as a multiple (n) of the normal affinity K_d. Assuming only the conducting mode in a multi-ion state accounts for the majority of permeation events (Scheme 3.3, green box with dotted line), the conductance-[ion] relationship is

$$conductance = \gamma_{max} \cdot \frac{\frac{[ion]^2}{K_{d1}K_{d2}}}{1 + \frac{[ion]}{K_{d1}} + \frac{[ion]^2}{K_{d1}K_{d2}} + Y_0\left(1 + \frac{[ion]}{nK_{d1}} + \frac{[ion]^2}{n^2K_{d1}K_{d2}}\right)} \tag{3.16}$$

where γ_{max} is the saturating conductance which is effectively the exit rate (k_{ex}). K_{d2} is effectively the K_M, ($\frac{k_{off}+k_{ex}}{k_{on}}$), under quasi-steady-state assumption. This model was invoked to explain the observed sigmoidal behavior of the concentration-conductance relationship while taking into account the likely negative cooperativity of sequential ion binding.

3.4.6 Data analysis

Curve fitting and statistical analysis were performed in Prism 5 (GraphPad software). Data are presented as mean ± S.E.M. unless indicated otherwise. Parameters obtained from curve fitting are presented as value ± standard error of fit.

3.5 Results

3.5.1 Intracellular spermine blocks hTPC2^{PM}

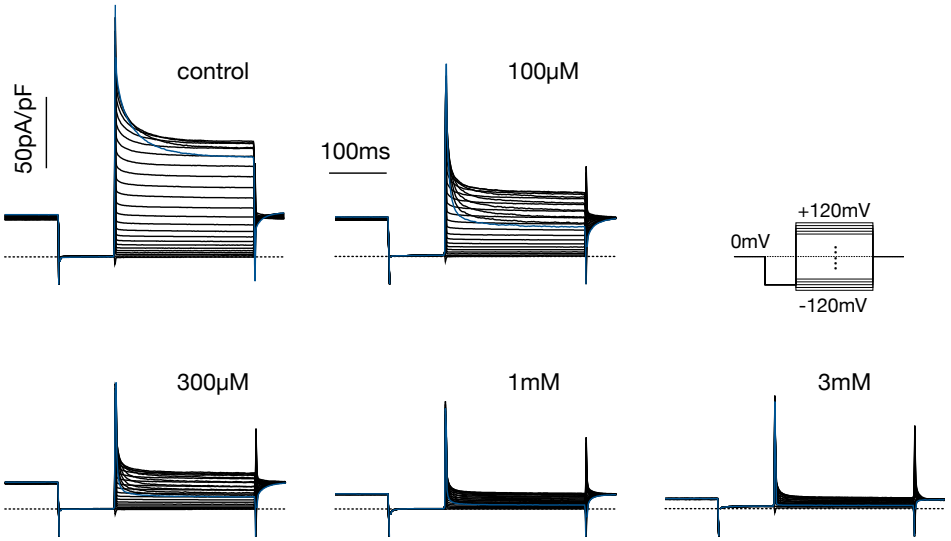

Figure 3.1 Intracellular spermine blocks hTPC2^{PM}

Na^+ current was recorded in the presence of increasing concentrations of intracellular spermine. Blue trace denotes the current trace recorded at +120mV. Extracellular [Na^+] = 0mM (145mM $NMDG^+$), pH 5.50; intracellular [Na^+] = 145mM, pH 7.20. n = 5-13 each.

When spermine was present in the pipette solution, time-dependent decay of the hTPC2^{PM} current was observed that becomes more profound as the concentration increases and the voltage becomes more positive (Figure 3.1). This was quantified in an I-V plot (Figure 3.2A), where the family of I-V relations shows a negative conductance and the suppression becomes more complete as [spermine] increases. The extreme outward rectification and the very negative reversal potential is due to the ionic gradient used, zero Na^+_o and 145mM Na^+_I, which ensures that little or virtually no leak was present that could alter the observed rectification of I-V relation when otherwise present.

3.5.2 A bi-molecular mechanism of block

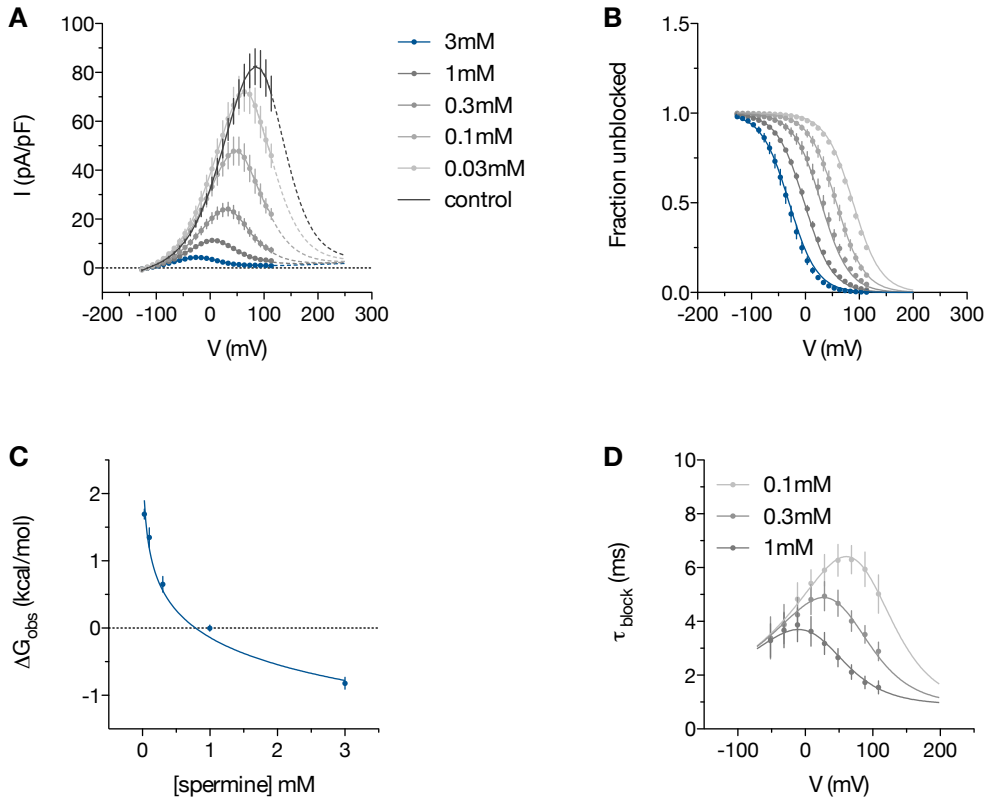

Figure 3.2 Voltage and concentration dependence of block

A. I-V plot of the steady-state current shown in Figure 3.1. n = 5-13 each.
B. Voltage and concentration dependence of spermine block. The data points were calculated using eq(3.3) by plugging in the experimental values of ΔG_{obs} and z (extracted from A using eq.(3.4)) for each concentration and cell; shown are averaged data. Family of data was fitted to eq.(3.6). K_d = 1.87±0.02 mM at zero voltage, δ_{SF} = 0.76±0.0013.
C. [spermine] dependence of ΔG_{obs}. Data were fitted to eq.(3.7). K_d = 0.79±0.06 mM at zero voltage.
D. Voltage and concentration dependence of time constants extracted from Figure 3.1 by fitting the first 100ms of the blocking event with a double exponential. Spermine block itself exhibits a single-exponential behavior; the second exponential is attributed to the intrinsic slow decay of the current. Family of data were fitted to eq.(3.8). k_{on} = 132±33 $M^{-1}ms^{-1}$, k_{off} = 0.229±0.013 ms^{-1}, δ_{SF} = 0.79±0.02, $f_{0\rightarrow TS}$ = 0.71±0.04.

To identify the mechanism of block, we quantified the effect of [spermine] on the voltage dependence. The voltage dependence was formally quantified in Figure 3.2B, which shows a classic sigmoidal decay in fractional current as a function of

voltage. The voltage dependence was first individually quantified using a more natural form of the Boltzmann equation (eq.(3.3)), which allows the decomposition of the energetic term into ΔG_{obs} and the voltage dependence. In this form, it can be seen that ΔG_{obs} can be identified at 0mV, while the effective valence of block contributes to the steepness and the V_{50} of the curve. When ΔG_{obs} is plotted against [spermine], it can be seen that increasing [spermine] makes the ΔG_{obs} more negative, without changing the effective valence, in a manner that is well described by bi-molecular interaction (eq.(3.7)). Using this model (eq.(3.6)), the family of voltage dependence curves in Figure 3.2B can be fitted globally using the same parameter set with the only changing parameter being [spermine]. The K_d of spermine at this blocking site is 1.87±0.02 mM at zero voltage. The exponential dependence on voltage of the K_d, can be naturally inferred from the voltage dependence (Figure 3.2 & eq.(3.6)).

Because the data were recorded under zero extracellular Na^+, we conclude that this represents intrinsic voltage dependence where an observable voltage gradient is present in the path involved in spermine block. According to this model (Scheme 3.1), assuming that spermine penetrates fully into the aqueous cavity but not into the selectivity filter (eq.(3.5), f_{spm}=1), the voltage drop across the selectivity filter is 0.76±0.0013 and the remaining voltage drop is therefore 0.24.

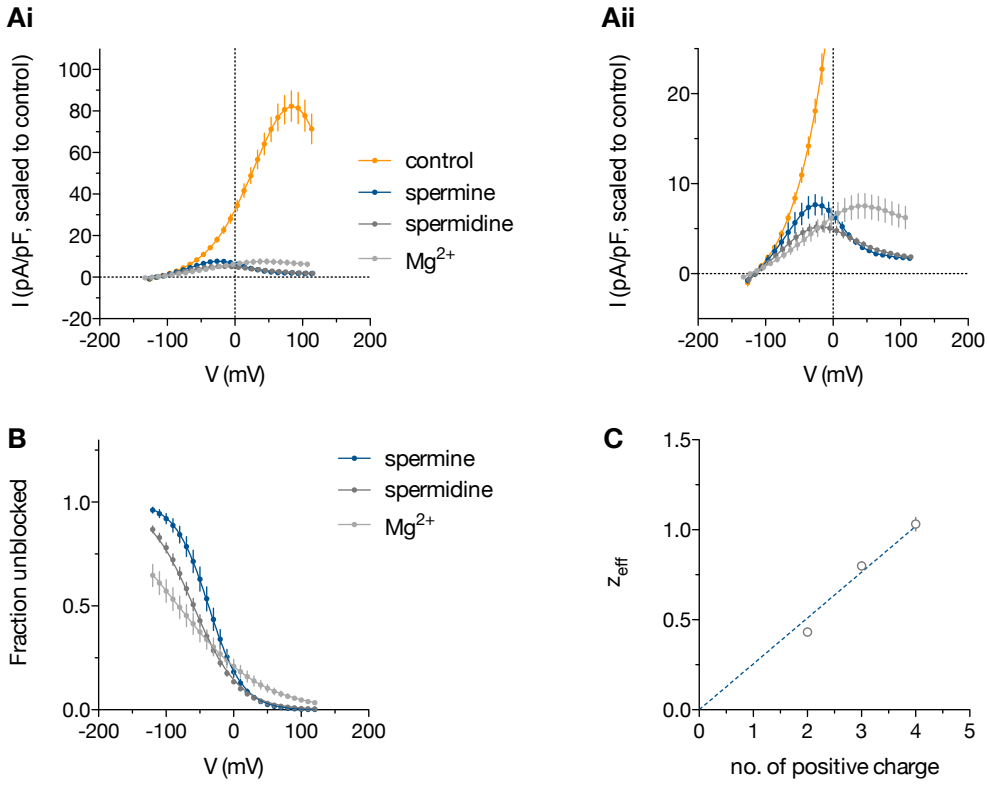

Figure 3.3 Voltage sensitivity is a function of blocker valence

A. I-V plots of control and spermine, spermidine or Mg^{2+} present at 3mM in internal solution. Ai, original scale; Aii, expanded scale. n = 5-9 each.
B. Voltage dependence extracted from A using eq.(3.4). Data were fitted with eq.(3.6) with δ_{SF} fixed to 0.75 according to C; f_{Mg} = 0.82±0.04; K_d of spermine = 0.69±0.05mM; K_d of spermidine = 0.51±0.02mM; K_d of Mg^{2+} = 0.79±0.05mM (all at 0mV).
C. Relationship between z_{eff} and blocker valence. Line is constrained to go through the origin as required and has a slope (1 - δ_{SF}) of 0.25±0.01.

We further quantified the time constant of block to investigate the voltage dependence of the underlying rate constants. Figure 3.2D shows the voltage dependence of the blocking time constant at different [spermine]. It can be seen that the time constants display a bi-phasic voltage dependence, suggesting that k_{on} and k_{off} are both intrinsically voltage dependent. The asymmetry of the voltage dependence may also suggest that the peak of the energy barrier is not located at the mid point between the pore entrance and the aqueous cavity. Importantly,

increasing [spermine] selectively increases the on rate constant in a linear fashion, while having no effect on the off rate (Figure 3.2D). The family of curves was well fitted globally to eq.(3.8), which further shows that spermine block conforms with a bi-molecular mechanism. From this fit, we found that the k_{on} is 132±33 $M^{-1}ms^{-1}$, k_{off} is 0.229±0.013 ms^{-1}, the position of the energy barrier is 0.71±0.04 (closer to the cavity), and the voltage drop across the selectivity filter is 0.79±0.02, consistent with the equilibrium data discussed above. The K_d from the kinetic data is also consistent with the equilibrium data above, where k_{off}/k_{on} is 1.74mM.

3.5.3 Voltage sensitivity is a function of blocker valence

As the control current exhibits negative conductance at more extreme positive voltages, we tested whether the voltage sensitivity z_{eff} may be a function of blocker valence. We tested the effect of blockers with lower valence: spermidine, which has a similar structure but has a valence of 3, and Mg^{2+}, which has been reported to block hTPC2 previously [159] and has a valence of 2. As expected, the presence of these blockers resulted in substantial suppression of the outward current and negative changes in conductance (Figure 3.3A). The underlying voltage dependence was extracted using eq.(3.4). Indeed, the voltage sensitivity z_{eff}, i.e. the slope, decreases with blocker valence (Figure 3.3B) and appears to be a linear function of blocker valence (Figure 3.3C). This indicates that the voltage dependence observed is indeed a block and that these blockers may have very similar site of action. The slope of this plot is 0.25±0.01 (Figure 3.3C), which corresponds to the fractional voltage drop across the aqueous cavity and is consistent with the result obtained from the spermine data alone.

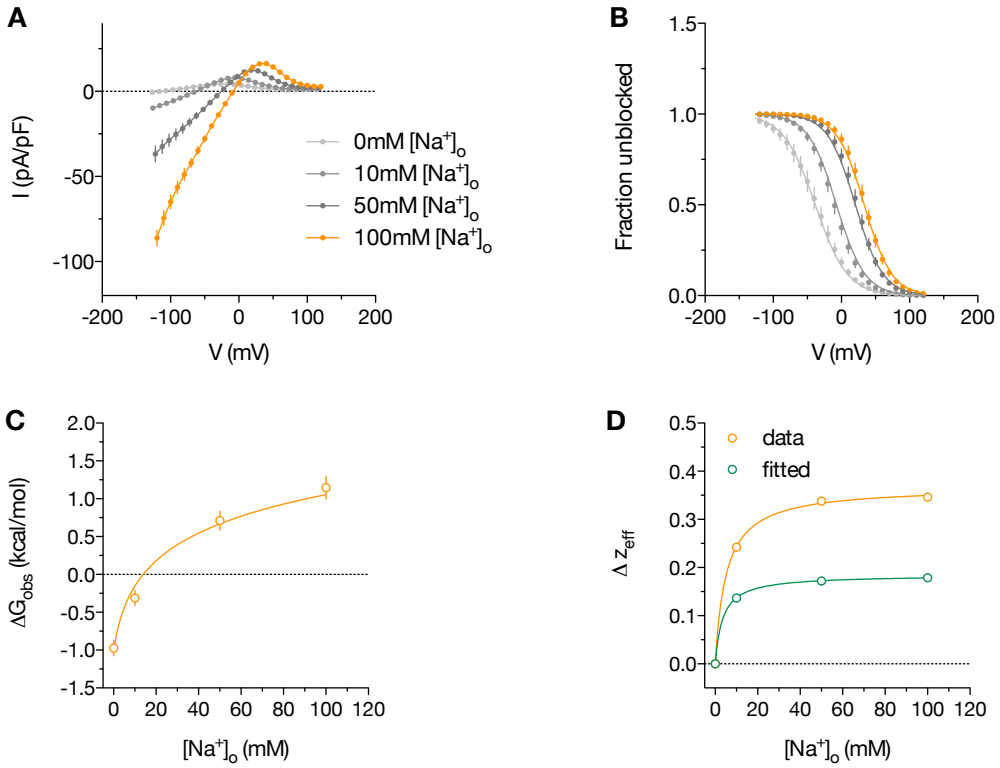

Figure 3.4 Na^+ affects the energetics of block and permeates

A. I-V plot of the steady-state current in ion titration experiments. [spm] = 3mM, intracellular [Na^+] = 145mM, extracellular [Na^+] = 0, 10, 50 & 100mM. n = 6-8 each.
B. $[Na^+]_o$ dependence of spermine block plotted using data extracted from A. Family of data was fitted to eq.(3.10). K_d of Na^+ = 3.97±0.36 mM, K_d of spermine = 0.59±0.004mM, δ_{SF} = 0.73±0.009, f_{ion} = 0.26±0.06.
C. $[Na^+]_o$ dependence of ΔG_{obs}. Data were fitted to eq.(3.11). ΔG_{spm} = -4.36±0.04kcal/mol (K_d = 0.56mM), K_d of Na^+ = 3.12±0.0004mM.
D. $[Na^+]_o$ dependence of Δz_{eff}. Data were fitted to the Michaelis-Menten equation. K_M = 5.13±0.36mM, $\Delta z_{eff\ max}$ = 0.37±0.004.

3.5.4 Selectivity filter occupancy interferes with block

With the basic physical picture of the ion-conduction pathway established, it is possible to investigate the effect of selectivity filter occupancy on block, and to use this as a tool to probe equilibrium ion selectivity at the selectivity filter where the ions bind, be it permeant or observably impermeant. We first investigated the effect

of the physiologically relevant permeant ion Na^+ by performing the same blocking experiments at varying extracellular [Na^+]. The I-V plot is shown in Figure 3.4A. It can be seen that increasing extracellular [Na^+] gives rise to increasing inward current, positively shifts the reversal potential and the voltage required to produce negative conductance. This is quantified in Figure 3.4B & C where the voltage dependence is positively shifted (eq.(3.9)) hence the inferred ΔG_{obs} is made more positive as extracellular [Na^+] increases (eq.(3.11)). This strongly suggests that increasing extracellular [Na^+] lowers the affinity of spermine block (eq.(3.11)). The effective valence (z_{eff}) is also increased as extracellular [Na^+] increases as a saturating binding function (Figure 3.4D), suggesting that the site of Na^+ action is located within a voltage gradient at the selectivity filter, although this is considerably higher than that predicted by the model. The K_d of Na^+ at the selectivity filter was found to be 3.97±0.36 mM.

These data therefore conform to an allosteric mechanism where permeant ion binding at the selectivity filter allosterically interferes with spermine binding due to the close proximity of the binding sites and the strong electrostatic repulsion between the positively charged ions in a confined space (Scheme 3.2). Although we did not initially assume mutually exclusive binding between spermine and Na^+, it was found to be the case as the K_d of Na^+ binding in a spermine-bound channel is often at least several orders of magnitude higher than that of an unoccupied channel.

We then tested whether Ca^{2+}, a physiological divalent ion with 20-fold lower permeability, may occupy the selectivity filter by performing the same blocking experiments with varying extracellular [Ca^{2+}]. The I-V plot is shown in Figure 3.5A. In contrast to the Na^+ case, although increasing extracellular [Ca^{2+}] positively shifts the voltage required to produce negative conductance, it failed to give rise to significant inward current and only minimally shifted the reversal potential (Figure

3.8). This is quantified in Figure 3.5B & C, which show that the ΔG_{obs} of spermine block indeed positively shifted as a function of increasing extracellular [Ca^{2+}]. This suggests that increasing extracellular [Ca^{2+}] also lowers the affinity of spermine block. However, although increasing extracellular [Ca^{2+}] did positively shift the voltage dependence, the extent of shift is lower than that observed with Na^+ within the same concentration range. When fitted to the same model, we found that the K_d of Ca^{2+} at the selectivity filter is 10.6±0.0007 mM. This suggests that although Ca^{2+} exhibits very limited permeability, it is able to bind at the selectivity filter with an affinity that is about 3-fold lower than that of Na^+. As with Na^+, increasing extracellular [Ca^{2+}] increases z_{eff} as a saturating binding function (Figure 3.5D), suggesting that the binding site is indeed located within the selectivity filter.

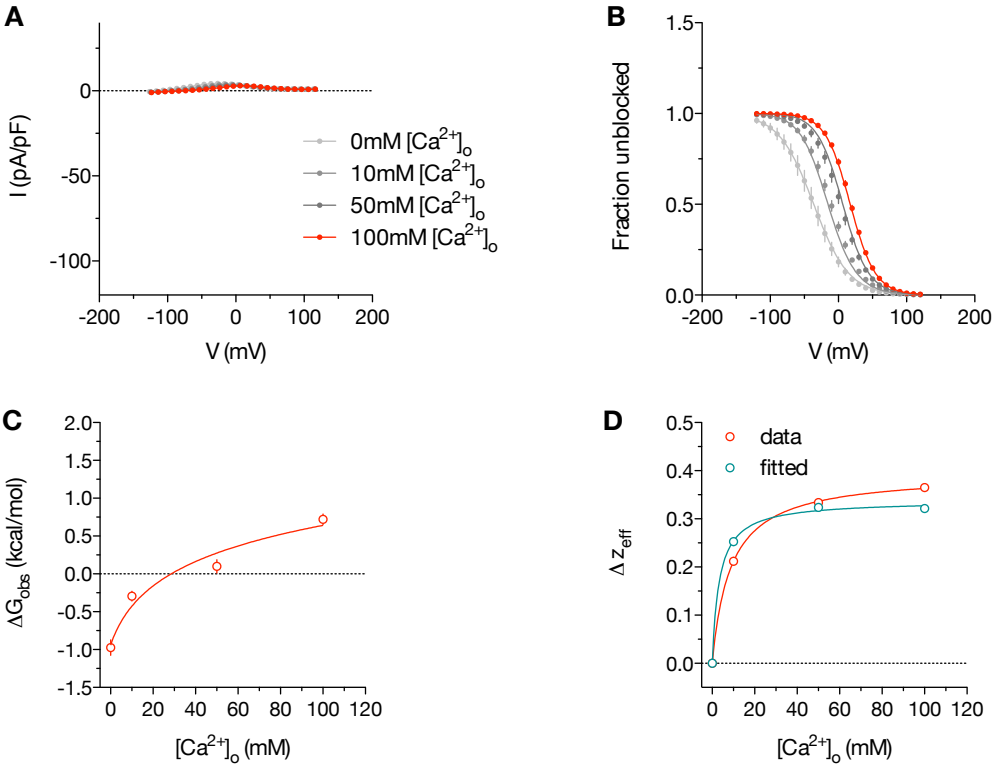

Figure 3.5 Ca^{2+} also affects the energetics of block, but does not permeate

A. I-V plot of the steady-state current in ion titration experiments similar to that shown in Figure 3.4. [spm] = 3mM, intracellular [Na^+] = 145mM, extracellular [Ca^{2+}] = 0, 10, 50 & 100mM. n = 4-6 each.
B. $[Ca^{2+}]_o$ dependence of spermine block plotted using data extracted from A. Family of data was fitted to eq.(3.10). K_d of Ca^{2+} = 10.6±0.0007mM, K_d of spermine = 0.74±0.003mM, δ_{SF} = 0.76±0.006, f_{ion} = 0.29±0.03.
C. $[Ca^{2+}]_o$ dependence of ΔG_{obs}. Data were fitted to eq.(3.11). ΔG_{spm} = -4.36±0.04kcal/mol (K_d = 0.56mM), K_d of Ca^{2+} = 6.6±0.001mM.
D. $[Ca^{2+}]_o$ dependence of Δz_{eff}. Data were fitted to the Michaelis-Menten equation. K_M = 8.68±0.26mM, $\Delta z_{eff\,max}$ = 0.39±0.003.

3.5.5 Equilibrium ion binding selectivity at the selectivity filter

The above examples show that it is possible to use spermine block as a tool to probe equilibrium ion selectivity at the selectivity filter more generally. We therefore extended the analysis by testing monovalent and divalent ions of the same groups with different ionic radii and investigated the mechanism of ion selectivity. Figure 3.6A & B show the effect of group I and II ions on the affinity of spermine block. It can be seen that 1) for the same concentration, ions with higher affinity are more effective at shifting ΔG_{obs}, and 2) the relationship of shift is the same for all the ions tested and the only difference is the concentration from which the shift starts to occur. These suggest that all the tested ions appear to obey the allosteric model within this concentration range while, according to eq.(3.11), the ions have different K_d's. Using this model, we arrived at the following sequence of equilibrium ion selectivity (K_d) of this binding site: Li^+ (0.54mM) < Na^+ (3.12mM) < K^+ (18.8mM) < Cs^+ (81.2mM) and Ba^{2+} (5.7mM) ~ Ca^{2+} (6.6mM) < Mg^{2+} (80.7mM). This is contrasted to the electrophysiological selectivity sequence: Na^+ (1) ≥ Li^+ (0.94) >> Ca^{2+} ~ Ba^{2+} (0.04) ≥ K^+ (0.03) ≥ Cs^+ (0.02) ≥ Mg^{2+} (<0.02). When plotted against ionic radius, we found that the K_d of group I monovalent ions exhibits an exponential relationship with increasing ionic radius (Figure 3.6Bi), which corresponds to a linear decrease in the binding energy (less tight) as the ionic radius increases (Figure 3.6Bii). Interestingly, the reverse trend is observed for group II divalent ions, where Mg^{2+} appears to be the least tightly bound within the group (Figure 3.6Bi & Bii).

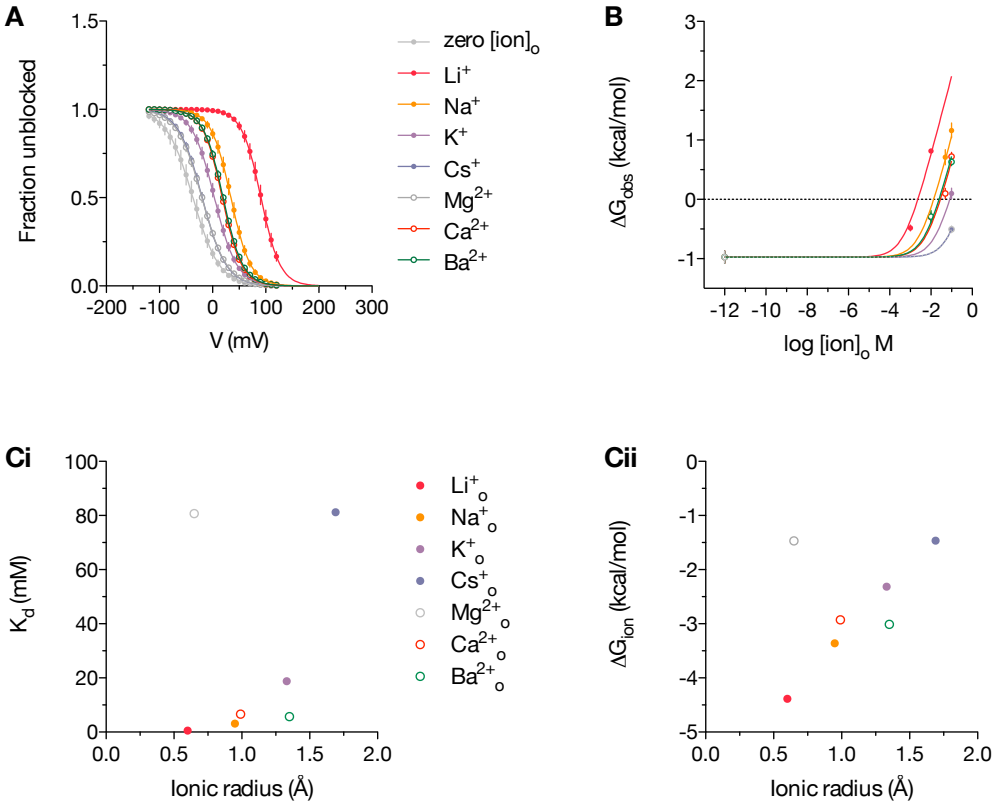

Figure 3.6 Equilibrium ion selectivity at the selectivity filter

A. ΔG_{obs} shifts in the presence of the indicated group I and II ions at 100mM on the external side. n = 4-7 each.

B. $[ion]_o$ dependence of ΔG_{obs}. n = 4-8 each. Family of data was fitted to eq.(3.11). ΔG_{spm} = -4.36±0.04kcal/mol (K_d = 0.56mM), K_d of Li^+ = 0.54±0.0001mM, K_d of Na^+ = 3.12±0.0004mM, K_d of Ca^{2+} = 6.6±0.001mM, K_d of Ba^{2+} = 5.7±0.001mM, K_d of K^+ = 18.8±0.005mM, K_d of Cs^+ = 81.2±0.03mM, K_d of Mg^{2+} = 80.7±0.03mM.

C. (i) K_d as a function of ionic radius. (ii) ΔG_{ion} as a function of ionic radius. ΔG_{ion} was calculated using $\Delta G_{ion} = RT \ln(K_{d\ ion})$ and was converted into kcal/mol.

3.5.6 Multi-ion binding correlates with ion throughout

In order to gain better understanding on the mechanism of ion selectivity and permeation, it is important to determine whether this one-ion binding state may

contribute directly to the actual ion permeation event or whether a multi-ion binding state may be involved. Figure 3.7 shows the current-[ion] relation for Li^+, Na^+ and Ca^{2+}. The sigmoidal behavior of Li^+ and Na^+ permeation suggests that it may involve further ion binding to achieve a multi-ion configuration at the selectivity filter, consistent with a K_M much larger than the K_d determined above. From the sigmoidicity, it is likely that this involves a ≥two-ion configuration. In contrast to Li^+ and Na^+ permeation, Ca^{2+} permeation, albeit little if any, follows a Michaelis-Menten relation with a K_M similar to that of the K_d determined above. This suggests that the permeant ions Li^+ and Na^+ are both able to establish a multi-ion configuration, while the impermeant ion Ca^{2+} remains in a single-ion binding state throughout this concentration range. This implies a knock-on mechanism of Li^+ and Na^+ permeation and that failure to establish a knock-on-permissive multi-ion configuration may be one of the mechanisms that prevents Ca^{2+} from permeating at a physiologically significant rate. Indeed, the very low conductance of Ca^{2+} (Figure 3.7C) is consistent with this interpretation.

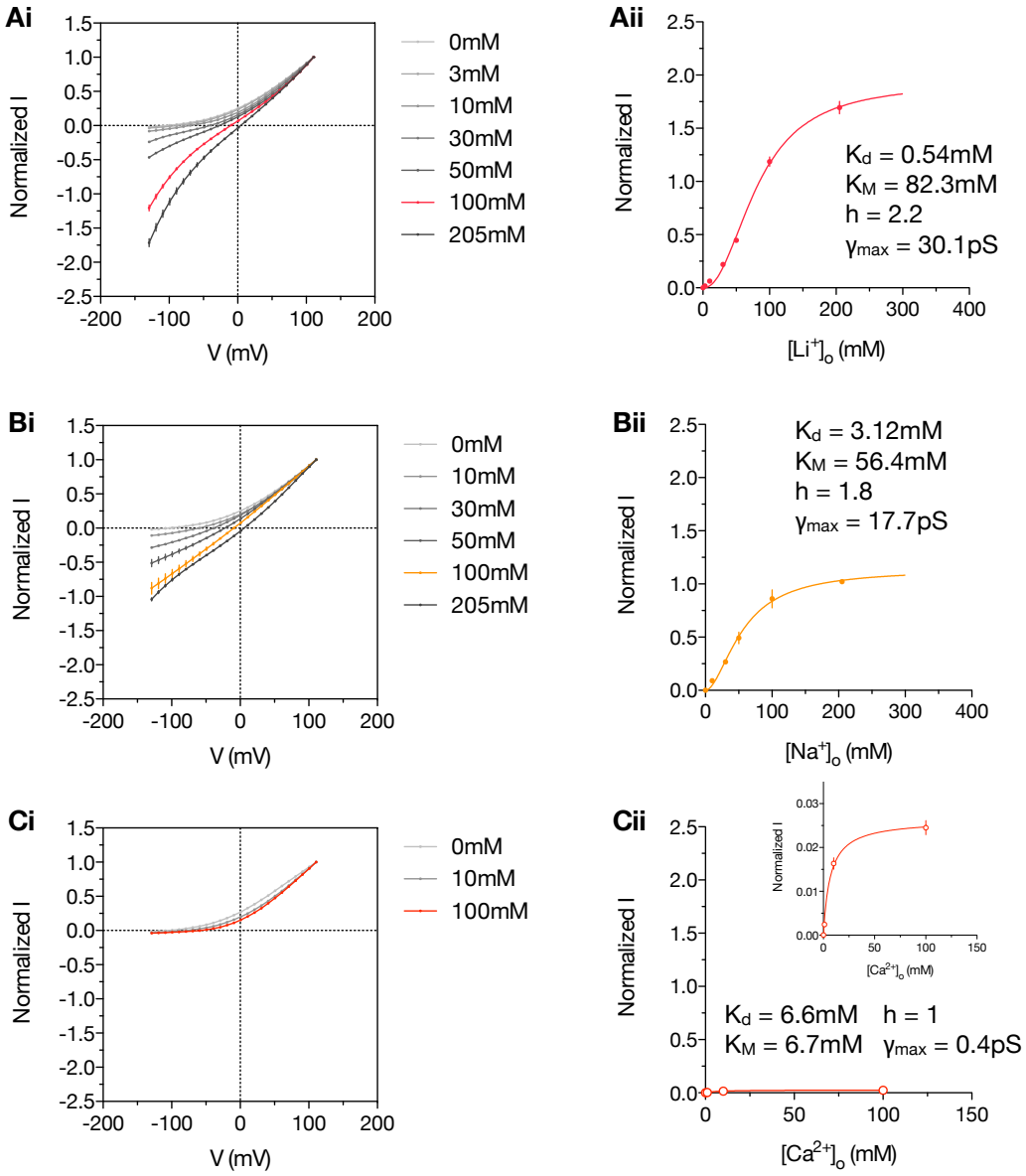

Figure 3.7 Multi-ion occupancy correlates with ion throughput

I-V plot (i) and current-[ion] plot (ii) for (A) Li^+, (B) Na^+ and (C) Ca^{2+} at -120mV under bi-ionic conditions with intracellular Na^+ held at 145mM. Current amplitudes were normalized to outward Na^+ at +120mV. n = 4-9 each. Data were fitted to the Michaelis-Menten equation scaled with a Hill slope-like sigmoidicity factor (h). Affinity differences are shown to illustrate the difference between ion binding and permeation for Li^+ and Na^+ but not Ca^{2+}. K_M of Li^+ = 82.3±5.3mM, h_{Li} = 2.19±0.19, K_M of Na^+ = 56.4±5.6mM, h_{Na} = 1.79±0.23, K_M of Ca^{2+} = 6.7±1.08mM, h_{Ca} = 1. γ_{max} was calculated based on the unitary conductance of Na^+ at symmetrical 145mM estimated previously from noise analysis. γ_{max} of Li^+ = 29.1±1.38pS, γ_{max} of Na^+ = 17.2±1.04pS, γ_{max} of Ca^{2+} = 0.4±0.02pS.

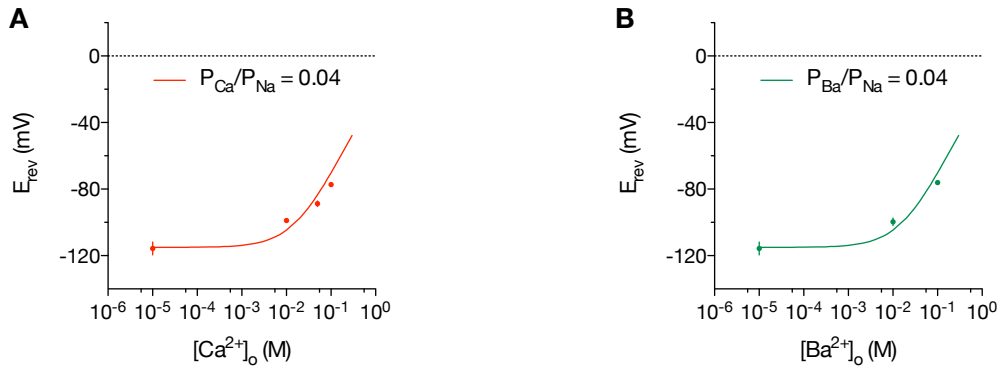

Figure 3.8 Comparison of Ca^{2+} and Ba^{2+} bi-ionic relative permeability

P_X/P_{Na} was determined under bi-ionic condition, A) Ca^{2+} and B) Ba^{2+}. Extracellular [Ca^{2+}] and [Ba^{2+}] are as indicated and external was pH 5.5; intracellular [Na^{+}] = 145mM, pH 7.2. See Methods for solution composition. Data were fit visually to eq.(3.2). n = 4-6 each.

3.5.7 Equilibrium selectivity and ion throughput contributes to electrophysiological selectivity

We plotted the flux ratio against the occupancy for each ion (Figure 3.9A). This plot is analogous to the classical definition of permeability and relates the degree of occupancy ($[ion]_o/K_d$) to the flux ratio through

$$Flux\ ratio = \frac{K_{M\,i}}{k_i[ion]_i} \cdot k_o \frac{[ion]_o}{K_{M\,o}} \tag{3.17}$$

where K_M is the Michaelis-Menten constant, k is the exit rate constant of the bound ion; the subscripts o and i indicates external and internal, respectively. The term $\frac{K_{M\,i}}{k_i[ion]_i}$ is contributed solely by the internal ion and is a constant under our experimental condition. This relation is derived from a one-site permeation model under quasi-steady-state assumption, which allows us to relate equilibrium selectivity and ion throughput, as determined above, to electrophysiological

selectivity in the form of flux ratio. The use of this relation is supported by the Michaelis-Menten-like behavior of Na^+ permeation and that only one Ca^{2+} ion is admitted to the selectivity filter. Under these assumptions, therefore, the ratio of the slope to that of Na^+ can be interpreted as the ion exit rate relative to external Na^+. According to this relation, the flux ratio approaches infinity as $[ion]_o/K_d$ approaches infinity in a linear fashion, which is indeed observed experimentally (Figure 3.9A).

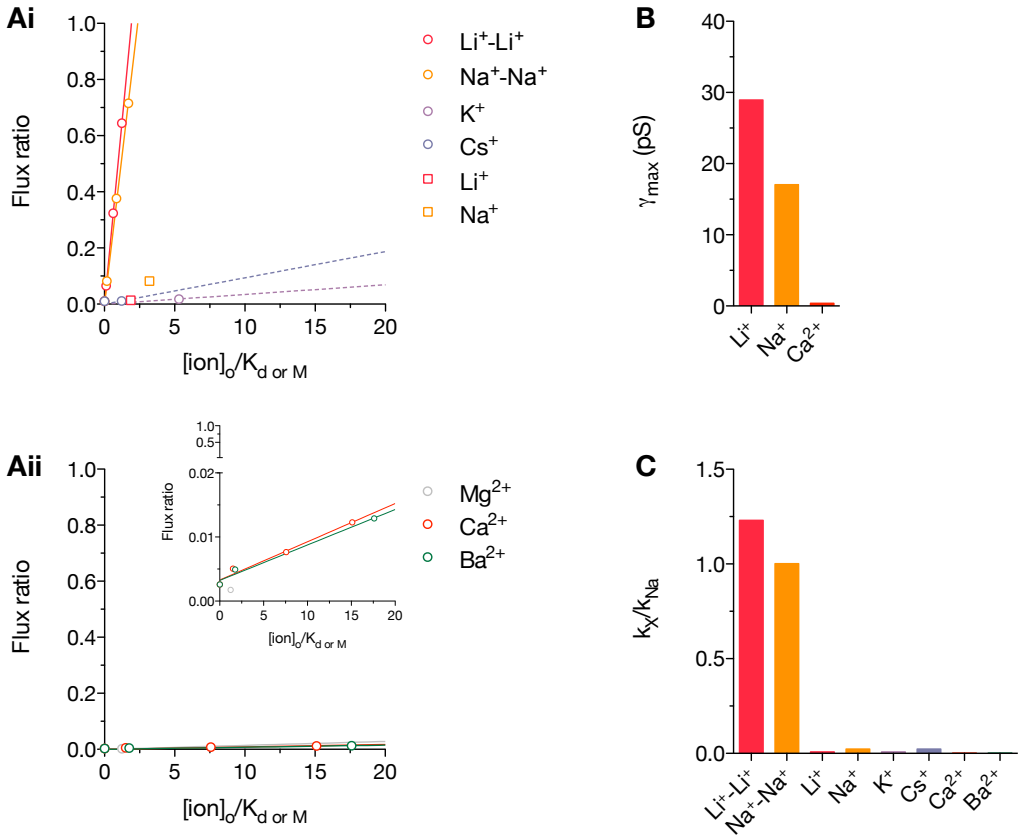

Figure 3.9 Relation between ion binding affinity, throughput and electrophysiological selectivity

A. (i-ii) Ion flux relative to that of intracellular Na^+ as a linear function of occupancy ($[ion]_o/K_d$). Shown are data for monovalent (i) and divalent (ii) ions. For monovalent ions, flux ratios were calculated using $flux\ ratio = \exp\left(\frac{E_{rev}F}{RT}\right)$. For divalent ions, flux ratios were calculated using $flux\ ratio = 0.25 \cdot \exp\left(\frac{E_{rev}F}{RT}\right) \cdot \left(\exp\left(\frac{E_{rev}F}{RT}\right) + 1\right)$. Inset, expanded scale.

B. Estimated saturating single-channel conductance of Li^+, Na^+ and Ca^{2+} from Figure 3.7.

C. Exit rate relative to Na^+ for all ions tested. Relative exit rates (k_X/k_{Na}) were calculated as the slope ratio to that of Na^+ extracted from Ai and Aii.

Using the above, we estimated that the exit rate of Ca^{2+} from its binding site (from the selectivity filter to the aqueous cavity) is >100-fold lower than that of Na^{+} in its permeation-permissive multi-ion configuration. Ba^{2+} appeared to behave almost identical to Ca^{2+} in terms of both affinity and exit rate. The low rate of Ca^{2+} and Ba^{2+} exit likely explains their low relative permeability and is in semi-quantitatively agreement with the very low conductance of Ca^{2+} (Figure 3.7C & Figure 3.9B). This is intuitive since the K_d of Ca^{2+} for the single-ion state is much lower than the K_M of Na^{+} for the multi-ion state. We note that the rates of Li^{+} and Na^{+} permeation are similarly low in their one-ion binding configuration (Figure 3.9C), suggesting that multi-ion occupancy indeed increases the ion exit rate, i.e. lower energy barrier encountered upon releasing an ion. Together, our results indicate that, in hTPC2, the establishment of a knock-on permissive multi-ion configuration is a general mechanism for achieving a physiologically significant ion conduction rate and is fundamental to the generation of ion selectivity.

3.5.8 Evidence for a high energy barrier to Ca^{2+} permeation

Our data above suggest that Ca^{2+} observably occupies the selectivity filter but shows low probability of exiting from the selectivity filter, which in turn suggest that Ca^{2+} may block hTPC2 from the external side. We re-examined the bi-ionic Ca^{2+}_o/Na^{+}_I I-V curves and found that there is indeed voltage-dependent reduction of the outward Na^{+} current that cannot be accounted for by an increase in inward Ca^{2+} current at higher $[Ca^{2+}]_o$ (Figure 3.10A). We performed similar experiments with 30mM $[Na^{+}]_o$ to better examine the blockade in the inward direction and to see whether increasing $[Na^{+}]_o$ may decrease the ability of external Ca^{2+} to block hTPC2. As shown in Figure 3.10B, this is indeed the case. While 10mM $[Ca^{2+}]_o$ partially blocked hTPC2

in the absence of external Na^+ (Figure 3.10A), 10mM $[Ca^{2+}]_o$ was ineffective when 30mM $[Na^+]_o$ was present (Figure 3.10B). At 80mM $[Ca^{2+}]_o$, we indeed observe negative change in conductance at more extreme negative potential (Figure 3.10B). Nonetheless, quantification of block in this instance is not as straightforward as permeation occurs within the same voltage range.

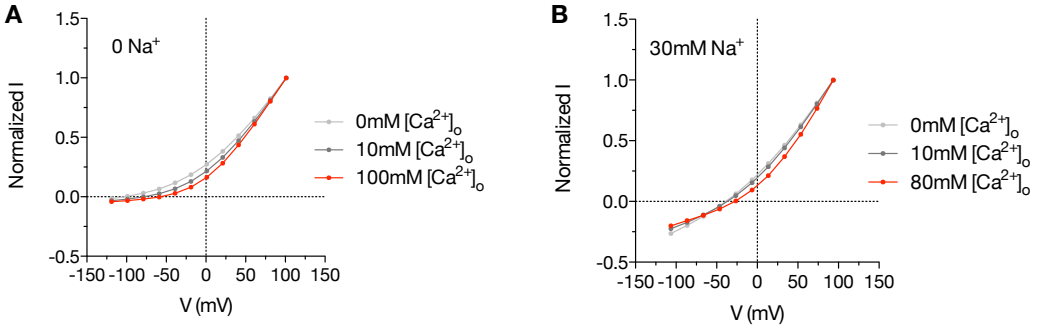

Figure 3.10 Evidence for a high energy barrier to Ca^{2+} permeation

A. I-V curves from Figure 3.7Ci. Outward Na^+ current is partially blocked in the voltage range that favours Ca^{2+} binding at the selectivity filter. At extreme -ve voltages, Ca^{2+} gave rise to little if any inward current. n = 4-8 each.

B. I-V curves similar to A, but in the presence of 30mM extracellular Na^+. Partial blockade by extracellular Ca^{2+} is alleviated, consistent with competition. The voltage-dependent decrease in Na^+ conductance due to partial blockade is shown more evidently when inward current is present. Extracellular solution (mM): 30 Na, 0-80 Ca^{2+}, pH 5.5; intracellular solution (mM): 145 Na^+, pH 7.2.

3.5.9 A possible non-conducting mode adopted by the selectivity filter

In the above, we fitted the data using the Michaelis-Menten equation incorporated with a sigmoidicity factor without including further details. We note that sigmoidicity requires positive cooperativity yet sequential ion-binding events are likely to display negative cooperativity due to electrostatic repulsion, which appears to be counter-intuitive. It appears that a non-conducting mode, akin to the inactive state in the MWC model, which binds ions with much lower affinity, has to be invoked in order to explain this apparent discrepancy. We find that with reasonable

constraints that fit with our experimental data and the assumptions of the model, the conductance data can be explained by this simplest MWC model (Scheme 3.3, eq.(3.16)), which can withstand certain degree of negative cooperativity while retaining sigmoidicity within a particular window of parameter set (Figure 3.11). Nevertheless, we suggest that further interpretation should await further experimental data.

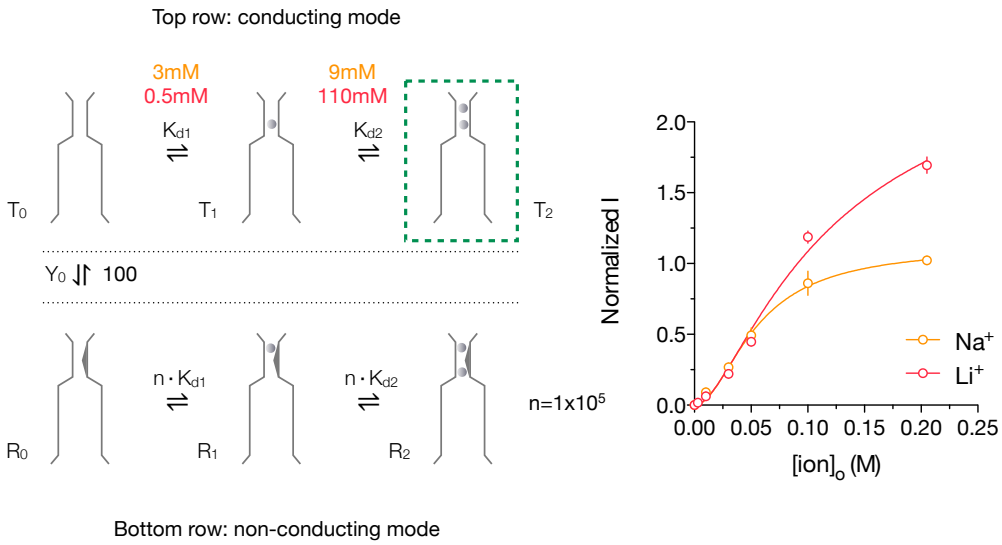

Figure 3.11 Evidence suggestive of a non-conducting mode of the hTPC2 selectivity filter

Na^+ and Li^+ conduction data from Figure 3.7 fitted with the MWC model (Scheme 3.3) shown on the left. The isomerization tendency Y_0 and the K_d multiple n were arbitrarily constrained to 100 and $1x10^5$ respectively for both Na^+ and Li^+ to capture the essence of the MWC model. K_{d1} for both ions were experimental values determined from the spermine block data and K_{d2} were left as the only free parameter. This model assumes the conducting mode in the two- or multi-ion state (green box with dotted line) accounts for the majority of the permeation events.

3.5.10 Location of the spermine-binding site

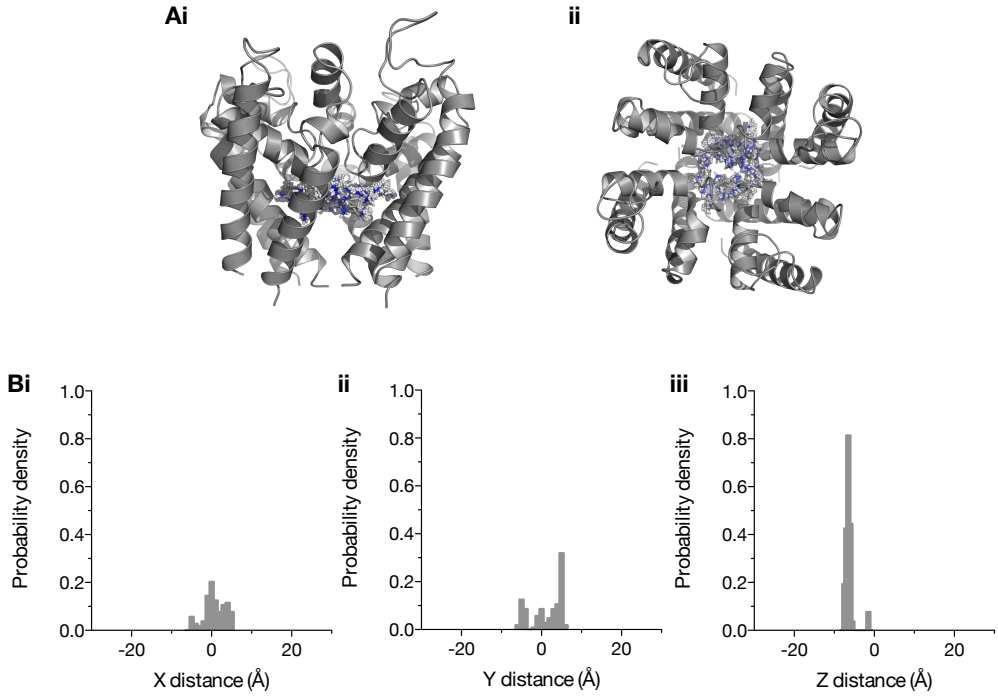

Figure 3.12 Low-energy configurations of spermine in a hTPC2 model

A. *In silico* docking of a fully charged (4+) spermine molecule with a homology model of hTPC2 using Autodock vina. (i) side view and (ii) view from the top (external/luminal). hTPC2 was modeled using Modeller 9.13 using Na_vMs (PDB entry: 3ZJZ) as a template as described in the Method section. Shown are the low-energy binding configurations (100 poses). Molecular graphic images were rendered using MacPyMol. *In silico* docking yielded a predicted K_d of ~0.87mM, which is in close agreement with experimental results.

B. X, Y, and Z center of mass distances of docked spermine molecules relative to that of the hTPC2 model. The center of mass values were calculated in VMD.

Finally, to identify potential spermine-binding site(s), we performed *in silico* docking using a fully charged (4+) spermine molecule with a homology model of the hTPC2 pore (S5-S6) based on the template Na_vMs (PDB entry: 3ZJZ) (see methods for further details and citations). Figure 3.12A shows the low-energy binding configurations of spermine in the hTPC2 model. Results from *in silico* docking are in close agreement with the experimental K_d, which yielded a predicted

K_d of ~0.87mM. The locations of these potential binding sites were quantified as the distribution of the center of mass of the different spermine poses relative to that of the hTPC2 model (Figure 3.12B). It appears that spermine may have some preferences for the peripheral spaces in the aqueous cavity (X-Y distribution) and shows remarkable preference for the residues right below the selectivity filter (Z distribution). This supports our predicted model of spermine binding and thus the experimentally inferred voltage profile along the Z-axis of hTPC2.

3.6 Discussion

Here, we investigated the mechanism of spermine block and utilized this phenomenon to study the ability of different external ions to occupy the selectivity filter of hTPC2^{PM}. Our experimental observations suggest that spermine block of hTPC2 is consistent with a bi-molecular mechanism, most likely through direct occlusion by binding at the channel's aqueous cavity. By analyzing the shift in spermine binding energy in the presence of different external ions, we have identified the different binding affinities of different ions at the selectivity filter. Importantly, our study relates equilibrium and kinetic selectivity to electrophysiological selectivity, which allows deeper understanding of the energetics associated with ion permeation.

Consistent with previous studies on K_{ir} channels [220-223], we found that selectivity filter occupancy antagonizes the binding of the blocker, most likely via direct electrostatic repulsion in the confined space within the channel. However, instead of a single-step linear voltage gradient approximation used in these studies, we have used a more realistic two-step voltage profile inferred from recent electrostatics calculations using experimental structures where most of the voltage drop is focused across the selectivity filter and the remaining voltage drops across the aqueous cavity [213-217]. It is likely that this accounts for the intrinsic voltage sensitivity of spermine block in the absence of external ions (Figure 3.2), while the occupancy of the selectivity filter accounts for the increase in the effective valence of block due to the vacation of ion at depolarizing voltages, which is expectedly more prominent as $[ion]_o$, and hence selectivity filter occupancy, increases (Figure 3.4 & Figure 3.5). Our experimental observations are therefore consistent with the picture that ions in the selectivity filter are more sensitive to voltage than in the aqueous cavity for any given transmembrane potential.

Various previous studies have employed different approaches to obtain experimental values of the K_d of putative ion-binding sites in a channel or selectivity filter. More recently, isothermal calorimetry (ITC) has been used for purified channels to obtain ion-binding affinities [224-228] which revealed that in K^+-selective channels such as KcsA, equilibrium selectivity appeared to be semi-quantitatively similar to electrophysiological selectivity, suggesting the involvement of selective binding in the generation of high K^+ selectivity [225]. However, similar to our results, there are also cases where equilibrium and electrophysiological selectivity do not match completely [226], suggesting indeed that one selectivity sequence does not necessarily reflect the other and vice versa. Our approach is akin to the pioneer studies by Neyton & Miller [229, 230] and more recently Piasta et al [231] who studied the effect of permeant and impermeant ions on blocking the permeation of the permeant blocker Ba^{2+} in K^+-selective channels. In contrast to these studies where the ionic effect is on the blocked state, the effect of external ions in our study is to prevent the establishment of a blocked state. Therefore, our data reflect ion-binding events in an empty channel and are therefore likely to remain valid in the absence of the blocker.

We conclude that in hTPC2, Na^+ vs Ca^{2+} selectivity under physiological conditions is likely governed by the following factors: 1) at physiological $[Na^+]$ as low as that found in the cytosol, $[Na^+]/K_d$ is ≥1 and is ≥10 at normal extracellular $[Na^+]$ whereas at physiological $[Ca^{2+}]_o$, $[Ca^{2+}]/K_d$ is ≤0.2 or ≤0.1 at lysosomal $[Ca^{2+}]_o$ and therefore little if any Ca^{2+} binding at the selectivity filter can occur; 2) the ion release rate of the permeation-permissive configuration of Ca^{2+} within the 100mM range is ~100-fold lower than that of Na^+, suggesting that Ca^{2+} faces a much higher energy barrier while attempting to escape from the selectivity filter to the aqueous cavity; 3) whereas Na^+ likely permeates by establishing a multi-ion configuration attainable within the 100mM range which tends to lower the energy barrier to ion release, Ca^{2+} is unable to establish this more permeation-permissive configuration within the

physiological range; and 4) thus increasing $[Ca^{2+}]_o$ increasingly blocks hTPC2 rather than being conducted through (Figure 3.10). These conclusions are supported by the quantitative and coherent relationship between ion-binding selectivity, ion throughput and the observed electrophysiological selectivity, which were all determined systematically in this study.

Recently, the appearance of the crystal structure of a prokaryotic voltage-gated Na^+-selective channel, NavAb [147, 232], has prompted computational studies on Na^+ permeation through the selectivity filter of this channel [233-240]. From the crystal structure and these studies, there appear to be two to three Na^+-binding sites within the selectivity filter, lined by the SELT sequence contributed by the side chains of S and E and the backbone carbonyls of L and T. The two-ion mechanism (or >1) of ion conduction inferred from our results is qualitatively similar to this observation. In addition, the low affinity of ion binding in hTPC2 is also qualitatively similar to the observation that no deep energy wells are observed in the ion conduction pathway in NavAb.

In NavAb, Na^+ appears to be coordinated by the carboxyl group of a glutamate at the top site and one carbonyl of a leucine at the lower site while retaining most of the water molecules in its first hydration shell. The putative selectivity filter of hTPC2 or TPCs in general is not very dissimilar to this SELT sequence, which is predicted to be lined by NATT and NNVV in the first and the second pore domain respectively if one considers the side chain and backbone carbonyl usage in the SELT filter and the considerable chemical similarity of N to a protonated D. From molecular dynamics studies, Ca^{2+} did not exhibit much lower affinity towards the selectivity filter, which is similar to our experimental observations that Na^+ and Ca^{2+} have similar binding affinities. Interestingly, the fully protonated EEEE ring of NavAb appears to close the pore and prevent Na^+ penetration into the selectivity filter [233, 238]. The one-carbon shorter Asp residue in TPC2, compared to the Glu

residue in Na_vAb at an equivalent position, may represent an evolutionary strategy to overcome this inherent geometry problem faced when exposed to an external acidic condition such as the lumen of the lysosome and may explain the insensitivity of Na^+ permeation at increasingly acidic external pH (Ch.2).

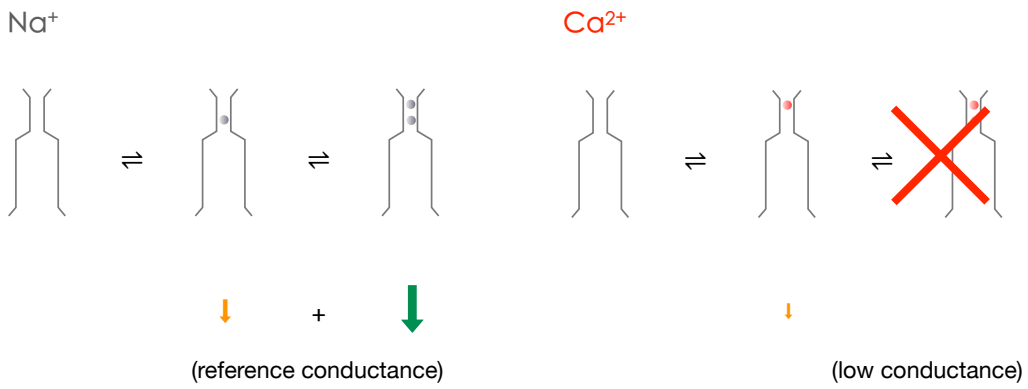

Figure 3.13 A possible mechanism for Na^+/Ca^{2+} selectivity
See text (below) for details.

Our final interpretation of the data is summarized in Figure 3.13. In the case of Na^+ and Li^+, two- or multi-ion binding is achievable within the 100-200mM range. Ion-ion repulsion therefore yields a high probability of ion exit to the intracellular side. In the case of Ca^{2+} and/or Ba^{2+} which are also able to bind at the selectivity filter with not-much-lower affinity, two- or multi-ion binding is not achievable within the 100-200mM range, the lone ion is therefore effectively trapped in the selectivity filter and hence a low probability of exit to the intracellular side. In light of the possible non-conducting mode of the selectivity filter (Scheme 3.3), a plausible scenario is that Na^+ or Li^+ binding progressively stabilizes the conducting mode, leading to the experimentally observed sigmoidicity despite the likely negative cooperativity of sequential ion binding.

3.7 Conclusion

In conclusion, we have identified an intracellular physiological blocker of hTPC2 and used it as a tool to experimentally investigate the mechanism of ion selectivity and permeation. Our study offers mechanistic, although abstract, insights into how the selectivity filter of hTPC2 selectively conducts Na^+ over Ca^{2+} or K^+ under physiological conditions. The different K_d's or K_M's for ion binding and permeation also imply the multi-ion nature of ion conduction in hTPC2, an apparently loosely general mechanism so far observed in biological ion channels within the 4x6TM superfamily whose atomic structures have been solved experimentally. Future studies will be required for further validation of these hypotheses, which would likely require the determination of the structure of this channel at atomic resolution and accompanying mutagenesis and computational studies.

3.8 Supplementary

Sequence alignment used in homology modeling

1st pore domain (S5-S6, 216-310)

```
hTPC2     202 MKKTLKCIRWSLPEMASVGLLLAIHLCLFTMFGMLLFAGGKQDDGQDRER     251
                          :.||..||.:...:..:....|:.....:
NavMs     131 --------------VGSVAALLTVVFYIAAVMATNLYGATFPE-------     159

hTPC2     252 LTYFQNLPESLTSLLVLLTTAN-NPDVMIPAYSKNRAYAIFFIVFTVIGS     300
                :|.:|.:||.:|..::|..: :..::.|..:.:....:|||.|.::.:
NavMs     160 --WFGDLSKSLYTLFQVMTLESWSMGIVRPVMNVHPNAWVFFIPFIMLTT     207

hTPC2     301 LFLMNLLTAI-----    310
              ..::||...|
NavMs     208 FTVLNLFIGIIVDAM    222
```

2nd pore-domain (S11-S12, 579-694)

```
hTPC2     564 LMAVVASTVLGLVQNMRAFGGILVVVYYVFAIIGINLFRGGNSSYWANNF     636
                           :.:...:|.||:|:.|::..||: |.....|   |
NavMs     131 ----------------VGSVAALLTVVFYIAAVMATNLY-GATFPEW---F     161

hTPC2     637 DDFAAALVTLWNLMVVNNWQ--VFLDAYRRYSGPWSKIYFVLWWLVSSVI     684
              .|.:.:|.||:.:|.:.:|.  :.........:...|  ::|:.:.:::..
NavMs     162 GDLSKSLYTLFQVMTLESWSMGIVRPVMNVHPNAW--VFFIPFIMLTTFT     209

hTPC2     685 WVNLFLALIL---     694
              .:|||:.:|:
NavMs     210 VLNLFIGIIVDAM     222
```

External loop (grey) that is not present in the homology model

```
Model     551 -------------LMAVVASTVLGLVQNMRAFGGILVVVYYVFAIIGINL    600
                           |||||||||||||||||||||||||||||||||||||
hTPC2     551 IVFRFLRIIPSMKLMAVVASTVLGLVQNMRAFGGILVVVYYVFAIIGINL    600

Model     601 FRG------GNSS------------------YWANNFDDFAAALVTLWNLM    650
              |||      ||||                  ||||||||||||||||||||
hTPC2     601 FRGVIVALPGNSSLAPANGSAPCGSFEQLEYWANNFDDFAAALVTLWNLM    650

Model     651 VVNNWQVFLDAYRRYSGPWSKIYFVLWWLVSSVIWVNLFLALIL------    694
              ||||||||||||||||||||||||||||||||||||||||||||||||
hTPC2     651 VVNNWQVFLDAYRRYSGPWSKIYFVLWWLVSSVIWVNLFLALILENFLHK    700
```

4 Conclusion and outlook

In this thesis, a relatively detailed account has been given to relate electrophysiological ion selectivity, ion dynamics and ion-binding selectivity. These qualities are not separate but serial events starting from the initial ion-binding events to the resultant cellular ion dynamics, bridged by the electrophysiological ion selectivity, functional consequence of microscopic ion binding. Nevertheless, although these experimental observations provoke some interesting determinants that govern ion permeation, the molecular mechanisms that underlie these determinants have not been explored. One obstacle is the reliance on electrophysiological methods to determine ion-binding affinity, which would not be readily applicable to channel mutants that do not conduct ions at a measurable rate, which is possible given that pore-lining residues are the likely candidates for mutagenesis study. This emphasizes the need to expand the methodology range to determine ion-binding affinity experimentally without having to measure ionic current. Techniques that directly measure ion binding will thus be required.

One such technique is isothermal titration calorimetry (ITC). ITC directly measures the differential heat upon ion binding, thereby allowing the determination of both enthalpic and entropic contributions to the free energy of binding. Therefore, it is possible to extend the current study by investigating the potential differences in enthalpic and entropic contributions between different ions. Further ITC experiments combined with mutagenesis are likely to yield important information regarding the role of certain structural elements in the pore-lining region which may govern the enthalpic and entropic differences between different ions. Nevertheless, parallel electrophysiological investigation and those presented in this

thesis will be important for the interpretation of new ITC data in terms of the location and the stoichiometry of ion binding.

In addition, structural elements that underlie selectivity filter and the aqueous cavity have been unknown. Knowledge has been based mostly on multiple sequence alignment within the superfamily and/or homology modeling using recently available crystal structures of various bacterial Na_V channels as has been attempted here. Although secondary structure predictions, which are considerably accurate, can be used to help assign better alignment to the template, the exact homologous positions can be ambiguous as has been demonstrated recently in the case of the voltage-gated proton channel H_V1 [241] and depends to some extent on gap penalty assignment. Further, the lack of homologous template for the extracellular loops of both repeats of hTPC2 renders these domains not amenable to homology modeling and these domains have to be deleted to prevent the formation of erroneous structures that geometrically interfere with the pore helices. Therefore, as briefly mentioned in Ch.3, an experimental structure of TPCs will be required to more accurately assign the spatial organization of the pore residues and how the bound ion is coordinated and to test whether multi-ion-like mechanisms may be indeed operating in hTPC2.

Aside from the above biochemical and structural considerations of the permeation pathway, regulation of channel opening represents another important aspect that warrants further experimental investigation. Whether external protons may activate hTPC2 directly and how external protons and internal $PI(3,5)P_2$ exert their co-stimulatory effects are also not known. Reconstitution experiments recording macroscopic currents from demonstrably purified proteins will be required to address these questions. In addition, it is not known whether channel opening involves rearrangement of the four inner helices (S6) or conformational changes in the selectivity filter, which may also occur during channel gating. Fluorescent

labeling studies together with patch-clamp measurements and more detailed blocker accessibility experiments, for example, will provide functional clues to this intriguing question.

Direct measurements of biophysical, biochemical and structural properties of TPCs are likely to shed important light on channel function in the future, which should help clarify the controversies that the literature currently suffers. Thanks to the progress in *in vitro* expression systems and methods on whole-endolysosome patch-clamp, the elusive resident channels and transporters are now amenable to direct functional assessment. Together with the increasing list of endolysosomal channels/transporters identified, this is likely to provide tremendous insights into membrane transport mechanisms in endolysosomes and their molecular origin, which will ultimately allow for a better understanding in the elusive endolysosomal membrane physiology and pathophysiology.

Finally, how the basic electrophysiological properties of TPCs may fit with the proposed roles of TPCs is currently not clear. The substantial disparity between the channel properties of TPCs and the vast literature related to their proposed function may warrant further investigations but may also imply genuine incompatibility. It is maybe too early to speculate the potential role of a lysosomal Na^+-selective conductance, as details regarding the *trans*-lysosomal ionic gradient are not entirely clear [124, 157, 173]. Nonetheless, the work presented in this thesis provides a basis for further understanding the function of TPCs and establishes important constraints on potential channel function given their Na^+ selectivity and ligand sensitivity.

5 Appendix

Materials and reagents

Activated charcoal (Sigma)
ATP-Mg (Sigma)
$BaCl_2$ (AnalaR)
$Ba(OH)_2$ (Sigma)
$CaCl_2$ 1M solution (VWR)
$Ca(MeSO_3)_2$ (TCI)
$Ca(OH)_2$ (Sigma)
cADPR (synthesized in-house)
CsCl (Sigma)
$Cs(MeSO_3)$ (Sigma)
D-Glucose (Sigma)
EDTA (Sigma)
EGTA (Melford)
GTP-Na (Sigma)
HCl (Fisher Scientific)
HEPES (Melford)
IP_3 (Calbiochem or Sigma)
Ionomycin (Calbiochem)
LB broth (Sigma)
LB agar (Melford)
LiCl (Sigma or AnalaR)
LiOH (Sigma)
$Li_2(SO_4)$ (Sigma)
$MeSO_3H$ (TCI)
$MgCl_2$ 1M solution (Fluka or Sigma)
$Mg(SO_4)_2$ heptahydrate (AnalaR)
Monensin (Sigma)
NaCl (Fisher Scientific)
Na-gluconate (Sigma)

$NaHCO_3$ (AnalaR)
$Na(MeSO_3)$ (Sigma)
NaOH (AnalaR)
$Na_2(SO_4)$ (Sigma)
NAADP (synthesized in-house)
MES monohydrate (Sigma or Melford)
NMDG (Sigma)
KCl (Sigma)
$K(MeSO_3)$ (TCI)
KOH (AnalaR)
Spermidine trihydrochloride (Sigma)
Spermine tetrahydrochloride (Sigma)

6 Bibliography

1. Berridge, M.J., P. Lipp, and M.D. Bootman, *The versatility and universality of calcium signalling.* Nat Rev Mol Cell Biol, 2000. **1**(1): p. 11-21.
2. Hoeflich, K.P. and M. Ikura, *Calmodulin in action: diversity in target recognition and activation mechanisms.* Cell, 2002. **108**(6): p. 739-42.
3. Burgoyne, R.D., *Neuronal calcium sensor proteins: generating diversity in neuronal Ca2+ signalling.* Nat Rev Neurosci, 2007. **8**(3): p. 182-93.
4. Corbalan-Garcia, S. and J.C. Gomez-Fernandez, *Signaling through C2 domains: more than one lipid target.* Biochim Biophys Acta, 2014. **1838**(6): p. 1536-47.
5. Gerke, V., C.E. Creutz, and S.E. Moss, *Annexins: linking Ca2+ signalling to membrane dynamics.* Nat Rev Mol Cell Biol, 2005. **6**(6): p. 449-61.
6. Brini, M. and E. Carafoli, *Calcium pumps in health and disease.* Physiol Rev, 2009. **89**(4): p. 1341-78.
7. Prins, D. and M. Michalak, *Organellar calcium buffers.* Cold Spring Harb Perspect Biol, 2011. **3**(3).
8. Hilgemann, D.W., et al., *Molecular control of cardiac sodium homeostasis in health and disease.* J Cardiovasc Electrophysiol, 2006. **17 Suppl 1**: p. S47-S56.
9. Fill, M. and J.A. Copello, *Ryanodine receptor calcium release channels.* Physiol Rev, 2002. **82**(4): p. 893-922.
10. Foskett, J.K., et al., *Inositol trisphosphate receptor Ca2+ release channels.* Physiol Rev, 2007. **87**(2): p. 593-658.
11. Catterall, W.A., *Voltage-gated calcium channels.* Cold Spring Harb Perspect Biol, 2011. **3**(8): p. a003947.
12. Soboloff, J., et al., *STIM proteins: dynamic calcium signal transducers.* Nat Rev Mol Cell Biol, 2012. **13**(9): p. 549-65.
13. Ramsey, I.S., M. Delling, and D.E. Clapham, *An introduction to TRP channels.* Annu Rev Physiol, 2006. **68**: p. 619-47.
14. Schwaller, B., *Cytosolic Ca2+ buffers.* Cold Spring Harb Perspect Biol, 2010. **2**(11): p. a004051.
15. Ritter, S.L. and R.A. Hall, *Fine-tuning of GPCR activity by receptor-interacting proteins.* Nat Rev Mol Cell Biol, 2009. **10**(12): p. 819-30.
16. Feske, S., *Calcium signalling in lymphocyte activation and disease.* Nat Rev Immunol, 2007. **7**(9): p. 690-702.
17. Fimia, G.M. and P. Sassone-Corsi, *Cyclic AMP signalling.* J Cell Sci, 2001. **114**(Pt 11): p. 1971-2.
18. Lee, H.C., *Cyclic ADP-ribose and NAADP: fraternal twin messengers for calcium signaling.* Sci China Life Sci, 2011. **54**(8): p. 699-711.
19. Almahariq, M., F.C. Mei, and X. Cheng, *Cyclic AMP sensor EPAC proteins and energy homeostasis.* Trends Endocrinol Metab, 2014. **25**(2): p. 60-71.
20. Venturi, E., et al., *From eggs to hearts: what is the link between cyclic ADP-ribose and ryanodine receptors?* Cardiovasc Ther, 2012. **30**(2): p. 109-16.

21. Galione, A. and M. Ruas, *NAADP receptors.* Cell Calcium, 2005. **38**(3-4): p. 273-80.
22. Berridge, M.J., *Inositol trisphosphate and calcium signalling mechanisms.* Biochim Biophys Acta, 2009. **1793**(6): p. 933-40.
23. Kadamur, G. and E.M. Ross, *Mammalian phospholipase C.* Annu Rev Physiol, 2013. **75**: p. 127-54.
24. Pattni, K. and G. Banting, *Ins(1,4,5)P3 metabolism and the family of IP3-3Kinases.* Cell Signal, 2004. **16**(6): p. 643-54.
25. Furuichi, T., et al., *Primary structure and functional expression of the inositol 1,4,5-trisphosphate-binding protein P400.* Nature, 1989. **342**(6245): p. 32-8.
26. Supattapone, S., et al., *Solubilization, purification, and characterization of an inositol trisphosphate receptor.* J Biol Chem, 1988. **263**(3): p. 1530-4.
27. Miyawaki, A., et al., *Expressed cerebellar-type inositol 1,4,5-trisphosphate receptor, P400, has calcium release activity in a fibroblast L cell line.* Neuron, 1990. **5**(1): p. 11-8.
28. Mikoshiba, K., *IP3 receptor/Ca2+ channel: from discovery to new signaling concepts.* J Neurochem, 2007. **102**(5): p. 1426-46.
29. Taylor, C.W. and S.C. Tovey, *IP(3) receptors: toward understanding their activation.* Cold Spring Harb Perspect Biol, 2010. **2**(12): p. a004010.
30. Serysheva, II, et al., *Structure of the type 1 inositol 1,4,5-trisphosphate receptor revealed by electron cryomicroscopy.* J Biol Chem, 2003. **278**(24): p. 21319-22.
31. Bosanac, I., et al., *Structural insights into the regulatory mechanism of IP3 receptor.* Biochim Biophys Acta, 2004. **1742**(1-3): p. 89-102.
32. Bezprozvanny, I., J. Watras, and B.E. Ehrlich, *Bell-shaped calcium-response curves of Ins(1,4,5)P3- and calcium-gated channels from endoplasmic reticulum of cerebellum.* Nature, 1991. **351**(6329): p. 751-4.
33. Mak, D.O., S. McBride, and J.K. Foskett, *Inositol 1,4,5-trisphosphate [correction of tris-phosphate] activation of inositol trisphosphate [correction of tris-phosphate] receptor Ca2+ channel by ligand tuning of Ca2+ inhibition.* Proc Natl Acad Sci U S A, 1998. **95**(26): p. 15821-5.
34. Bosanac, I., et al., *Structure of the inositol 1,4,5-trisphosphate receptor binding core in complex with its ligand.* Nature, 2002. **420**(6916): p. 696-700.
35. Bosanac, I., et al., *Crystal structure of the ligand binding suppressor domain of type 1 inositol 1,4,5-trisphosphate receptor.* Mol Cell, 2005. **17**(2): p. 193-203.
36. Uchida, K., et al., *Critical regions for activation gating of the inositol 1,4,5-trisphosphate receptor.* J Biol Chem, 2003. **278**(19): p. 16551-60.
37. Clapper, D.L., et al., *Pyridine nucleotide metabolites stimulate calcium release from sea urchin egg microsomes desensitized to inositol trisphosphate.* J Biol Chem, 1987. **262**(20): p. 9561-8.
38. Lee, H.C., et al., *Structural determination of a cyclic metabolite of NAD+ with intracellular Ca2+-mobilizing activity.* J Biol Chem, 1989. **264**(3): p. 1608-15.
39. Lee, H.C. and R. Aarhus, *ADP-ribosyl cyclase: an enzyme that cyclizes NAD+ into a calcium-mobilizing metabolite.* Cell Regul, 1991. **2**(3): p. 203-9.
40. Howard, M., et al., *Formation and hydrolysis of cyclic ADP-ribose catalyzed by lymphocyte antigen CD38.* Science, 1993. **262**(5136): p. 1056-9.

41. Yamasaki, M., et al., *Role of NAADP and cADPR in the induction and maintenance of agonist-evoked Ca2+ spiking in mouse pancreatic acinar cells.* Curr Biol, 2005. **15**(9): p. 874-8.
42. Lewis, A.M., et al., *beta-Adrenergic receptor signaling increases NAADP and cADPR levels in the heart.* Biochem Biophys Res Commun, 2012. **427**(2): p. 326-9.
43. Lee, H.C., *Cyclic ADP-ribose and nicotinic acid adenine dinucleotide phosphate (NAADP) as messengers for calcium mobilization.* J Biol Chem, 2012. **287**(38): p. 31633-40.
44. De Flora, A., et al., *The CD38/cyclic ADP-ribose system: a topological paradox.* Int J Biochem Cell Biol, 1997. **29**(10): p. 1149-66.
45. Putney, J.W., *Calcium signaling*. 2nd ed. Methods in signal transduction. 2006, Boca Raton: CRC/Taylor & Francis. 509 p.
46. Galione, A., H.C. Lee, and W.B. Busa, *Ca(2+)-induced Ca2+ release in sea urchin egg homogenates: modulation by cyclic ADP-ribose.* Science, 1991. **253**(5024): p. 1143-6.
47. Lee, H.C., *Potentiation of calcium- and caffeine-induced calcium release by cyclic ADP-ribose.* J Biol Chem, 1993. **268**(1): p. 293-9.
48. Noguchi, N., et al., *Cyclic ADP-ribose binds to FK506-binding protein 12.6 to release Ca2+ from islet microsomes.* J Biol Chem, 1997. **272**(6): p. 3133-6.
49. Zhang, X., et al., *Dissociation of FKBP12.6 from ryanodine receptor type 2 is regulated by cyclic ADP-ribose but not beta-adrenergic stimulation in mouse cardiomyocytes.* Cardiovasc Res, 2009. **84**(2): p. 253-62.
50. Lukyanenko, V., et al., *Potentiation of Ca(2+) release by cADP-ribose in the heart is mediated by enhanced SR Ca(2+) uptake into the sarcoplasmic reticulum.* Circ Res, 2001. **89**(7): p. 614-22.
51. Yamasaki-Mann, M., A. Demuro, and I. Parker, *cADPR stimulates SERCA activity in Xenopus oocytes.* Cell Calcium, 2009. **45**(3): p. 293-9.
52. Macgregor, A.T., et al., *Dual effects of cyclic ADP-ribose on sarcoplasmic reticulum Ca2+ release and storage in cardiac myocytes isolated from guinea-pig and rat ventricle.* Cell Calcium, 2007. **41**(6): p. 537-46.
53. Gyorke, S. and D. Terentyev, *Modulation of ryanodine receptor by luminal calcium and accessory proteins in health and cardiac disease.* Cardiovasc Res, 2008. **77**(2): p. 245-55.
54. Chen, W., et al., *The ryanodine receptor store-sensing gate controls Ca2+ waves and Ca2+-triggered arrhythmias.* Nat Med, 2014. **20**(2): p. 184-92.
55. Kong, H., et al., *Caffeine induces Ca2+ release by reducing the threshold for luminal Ca2+ activation of the ryanodine receptor.* Biochem J, 2008. **414**(3): p. 441-52.
56. Lee, H.C. and R. Aarhus, *A derivative of NADP mobilizes calcium stores insensitive to inositol trisphosphate and cyclic ADP-ribose.* J Biol Chem, 1995. **270**(5): p. 2152-7.
57. Aarhus, R., et al., *Activation and inactivation of Ca2+ release by NAADP+.* J Biol Chem, 1996. **271**(15): p. 8513-6.
58. Billington, R.A. and A.A. Genazzani, *Characterization of NAADP(+) binding in sea urchin eggs.* Biochem Biophys Res Commun, 2000. **276**(1): p. 112-6.
59. Patel, S., G.C. Churchill, and A. Galione, *Unique kinetics of nicotinic acid-adenine dinucleotide phosphate (NAADP) binding enhance the sensitivity of NAADP receptors for their ligand.* Biochem J, 2000. **352 Pt 3**: p. 725-9.
60. Genazzani, A.A., R.M. Empson, and A. Galione, *Unique inactivation properties of NAADP-sensitive Ca2+ release.* J Biol Chem, 1996. **271**(20): p. 11599-602.

61. Genazzani, A.A., et al., *Pharmacological properties of the Ca2+-release mechanism sensitive to NAADP in the sea urchin egg.* Br J Pharmacol, 1997. **121**(7): p. 1489-95.
62. Billington, R.A. and A.A. Genazzani, *PPADS is a reversible competitive antagonist of the NAADP receptor.* Cell Calcium, 2007. **41**(6): p. 505-11.
63. Patel, S., et al., *Widespread distribution of binding sites for the novel Ca2+-mobilizing messenger, nicotinic acid adenine dinucleotide phosphate, in the brain.* J Biol Chem, 2000. **275**(47): p. 36495-7.
64. Bak, J., et al., *NAADP receptors are present and functional in the heart.* Curr Biol, 2001. **11**(12): p. 987-90.
65. Calcraft, P.J., et al., *NAADP mobilizes calcium from acidic organelles through two-pore channels.* Nature, 2009. **459**(7246): p. 596-600.
66. Lin-Moshier, Y., et al., *Photoaffinity labeling of nicotinic acid adenine dinucleotide phosphate (NAADP) targets in mammalian cells.* J Biol Chem, 2012. **287**(4): p. 2296-307.
67. Gambara, G., et al., *NAADP-induced Ca(2+ signaling in response to endothelin is via the receptor subtype B and requires the integrity of lipid rafts/caveolae.* J Cell Physiol, 2008. **216**(2): p. 396-404.
68. Aley, P.K., et al., *Nicotinic acid adenine dinucleotide phosphate (NAADP) is a second messenger in muscarinic receptor-induced contraction of guinea pig trachea.* J Biol Chem, 2013. **288**(16): p. 10986-93.
69. Coxon, C.H., et al., *NAADP regulates human platelet function.* Biochem J, 2012. **441**(1): p. 435-42.
70. Walseth, T.F., et al., *Nicotinic Acid Adenine Dinucleotide 2'-Phosphate (NAADP) Binding Proteins in T-Lymphocytes.* Messenger (Los Angel), 2012. **1**(1): p. 86-94.
71. Masgrau, R., et al., *NAADP: a new second messenger for glucose-induced Ca2+ responses in clonal pancreatic beta cells.* Curr Biol, 2003. **13**(3): p. 247-51.
72. Patterson, G.H., et al., *Separation of the glucose-stimulated cytoplasmic and mitochondrial NAD(P)H responses in pancreatic islet beta cells.* Proc Natl Acad Sci U S A, 2000. **97**(10): p. 5203-7.
73. Kirkman, H.N., G.F. Gaetani, and E.H. Clemons, *NADP-binding proteins causing reduced availability and sigmoid release of NADP+ in human erythrocytes.* J Biol Chem, 1986. **261**(9): p. 4039-45.
74. Preller, A., V. Guixe, and T. Ureta, *In vivo operation of the pentose phosphate pathway in frog oocytes is limited by NADP+ availability.* FEBS Lett, 1999. **446**(1): p. 149-52.
75. Berg, I., et al., *Nicotinic acid adenine dinucleotide phosphate (NAADP(+)) is an essential regulator of T-lymphocyte Ca(2+)-signaling.* J Cell Biol, 2000. **150**(3): p. 581-8.
76. Johnson, J.D. and S. Misler, *Nicotinic acid-adenine dinucleotide phosphate-sensitive calcium stores initiate insulin signaling in human beta cells.* Proc Natl Acad Sci U S A, 2002. **99**(22): p. 14566-71.
77. Yamasaki, M., et al., *Organelle selection determines agonist-specific Ca2+ signals in pancreatic acinar and beta cells.* J Biol Chem, 2004. **279**(8): p. 7234-40.
78. Cancela, J.M., G.C. Churchill, and A. Galione, *Coordination of agonist-induced Ca2+-signalling patterns by NAADP in pancreatic acinar cells.* Nature, 1999. **398**(6722): p. 74-6.
79. Cancela, J.M., et al., *Two different but converging messenger pathways to intracellular Ca(2+) release: the roles of nicotinic acid adenine dinucleotide phosphate, cyclic ADP-ribose and inositol trisphosphate.* EMBO J, 2000. **19**(11): p. 2549-57.

80. Kinnear, N.P., et al., *Lysosome-sarcoplasmic reticulum junctions. A trigger zone for calcium signaling by nicotinic acid adenine dinucleotide phosphate and endothelin-1.* J Biol Chem, 2004. **279**(52): p. 54319-26.
81. Harmer, A.R., D.V. Gallacher, and P.M. Smith, *Role of Ins(1,4,5)P3, cADP-ribose and nicotinic acid-adenine dinucleotide phosphate in Ca2+ signalling in mouse submandibular acinar cells.* Biochem J, 2001. **353**(Pt 3): p. 555-60.
82. Tengholm, A., B. Hellman, and E. Gylfe, *Mobilization of Ca2+ stores in individual pancreatic beta-cells permeabilized or not with digitonin or alpha-toxin.* Cell Calcium, 2000. **27**(1): p. 43-51.
83. Aley, P.K., et al., *A functional role for nicotinic acid adenine dinucleotide phosphate in oxytocin-mediated contraction of uterine smooth muscle from rat.* J Pharmacol Exp Ther, 2010. **333**(3): p. 726-35.
84. Barcelo-Torns, M., et al., *NAADP mediates ATP-induced Ca2+ signals in astrocytes.* FEBS Lett, 2011. **585**(14): p. 2300-6.
85. Nebel, M., et al., *Nicotinic acid adenine dinucleotide phosphate (NAADP)-mediated calcium signaling and arrhythmias in the heart evoked by beta-adrenergic stimulation.* J Biol Chem, 2013. **288**(22): p. 16017-30.
86. Aley, P.K., et al., *Nicotinic acid adenine dinucleotide phosphate regulates skeletal muscle differentiation via action at two-pore channels.* Proc Natl Acad Sci U S A, 2010. **107**(46): p. 19927-32.
87. Tugba Durlu-Kandilci, N., et al., *TPC2 proteins mediate nicotinic acid adenine dinucleotide phosphate (NAADP)- and agonist-evoked contractions of smooth muscle.* J Biol Chem, 2010. **285**(32): p. 24925-32.
88. Pereira, G.J., et al., *NAADP-sensitive two-pore channels are present and functional in gastric smooth muscle cells.* Cell Calcium, 2014. **56**(2): p. 51-8.
89. Jiang, Y.L., et al., *Nicotinic acid adenine dinucleotide phosphate (NAADP) activates global and heterogeneous local Ca2+ signals from NAADP- and ryanodine receptor-gated Ca2+ stores in pulmonary arterial myocytes.* J Biol Chem, 2013. **288**(15): p. 10381-94.
90. Arndt, L., et al., *NAADP and the two-pore channel protein 1 participate in the acrosome reaction in mammalian spermatozoa.* Mol Biol Cell, 2014. **25**(6): p. 948-64.
91. Lee, H.C. and R. Aarhus, *Structural determinants of nicotinic acid adenine dinucleotide phosphate important for its calcium-mobilizing activity.* J Biol Chem, 1997. **272**(33): p. 20378-83.
92. Billington, R.A., et al., *Role of the nicotinic acid group in NAADP receptor selectivity.* Cell Calcium, 2005. **37**(1): p. 81-6.
93. Jain, P., et al., *Nicotinic acid adenine dinucleotide phosphate analogues containing substituted nicotinic acid: effect of modification on Ca(2+) release.* J Med Chem, 2010. **53**(21): p. 7599-612.
94. Naylor, E., et al., *Identification of a chemical probe for NAADP by virtual screening.* Nat Chem Biol, 2009. **5**(4): p. 220-6.
95. Ali, R.A., et al., *Activity of nicotinic acid substituted nicotinic acid adenine dinucleotide phosphate (NAADP) analogs in a human cell line: difference in specificity between human and sea urchin NAADP receptors.* Cell Calcium, 2014. **55**(2): p. 93-103.

96. Favia, A., et al., *VEGF-induced neoangiogenesis is mediated by NAADP and two-pore channel-2-dependent Ca2+ signaling.* Proc Natl Acad Sci U S A, 2014. **111**(44): p. E4706-15.
97. Sanchez-Tusie, A.A., et al., *Characterization of NAADP-mediated calcium signaling in human spermatozoa.* Biochem Biophys Res Commun, 2014. **443**(2): p. 531-6.
98. Davis, L.C., et al., *NAADP activates two-pore channels on T cell cytolytic granules to stimulate exocytosis and killing.* Curr Biol, 2012. **22**(24): p. 2331-7.
99. Brailoiu, E., et al., *Essential requirement for two-pore channel 1 in NAADP-mediated calcium signaling.* J Cell Biol, 2009. **186**(2): p. 201-9.
100. Dammermann, W., et al., *NAADP-mediated Ca2+ signaling via type 1 ryanodine receptor in T cells revealed by a synthetic NAADP antagonist.* Proc Natl Acad Sci U S A, 2009. **106**(26): p. 10678-83.
101. Genazzani, A.A. and A. Galione, *Nicotinic acid-adenine dinucleotide phosphate mobilizes Ca2+ from a thapsigargin-insensitive pool.* Biochem J, 1996. **315 (Pt 3)**: p. 721-5.
102. Lee, H.C. and R. Aarhus, *Functional visualization of the separate but interacting calcium stores sensitive to NAADP and cyclic ADP-ribose.* J Cell Sci, 2000. **113 Pt 24**: p. 4413-20.
103. Churchill, G.C., et al., *NAADP mobilizes Ca(2+) from reserve granules, lysosome-related organelles, in sea urchin eggs.* Cell, 2002. **111**(5): p. 703-8.
104. Morgan, A.J. and A. Galione, *Fertilization and nicotinic acid adenine dinucleotide phosphate induce pH changes in acidic Ca(2+) stores in sea urchin eggs.* J Biol Chem, 2007. **282**(52): p. 37730-7.
105. Morgan, A.J., et al., *Bidirectional Ca(2)(+) signaling occurs between the endoplasmic reticulum and acidic organelles.* J Cell Biol, 2013. **200**(6): p. 789-805.
106. Macgregor, A., et al., *NAADP controls cross-talk between distinct Ca2+ stores in the heart.* J Biol Chem, 2007. **282**(20): p. 15302-11.
107. Gerasimenko, J.V., et al., *NAADP mobilizes Ca2+ from a thapsigargin-sensitive store in the nuclear envelope by activating ryanodine receptors.* J Cell Biol, 2003. **163**(2): p. 271-82.
108. Gerasimenko, J.V., et al., *NAADP, cADPR and IP3 all release Ca2+ from the endoplasmic reticulum and an acidic store in the secretory granule area.* J Cell Sci, 2006. **119**(Pt 2): p. 226-38.
109. Churchill, G.C. and A. Galione, *Spatial control of Ca2+ signaling by nicotinic acid adenine dinucleotide phosphate diffusion and gradients.* J Biol Chem, 2000. **275**(49): p. 38687-92.
110. Churchill, G.C. and A. Galione, *NAADP induces Ca2+ oscillations via a two-pool mechanism by priming IP3- and cADPR-sensitive Ca2+ stores.* EMBO J, 2001. **20**(11): p. 2666-71.
111. Burdakov, D. and A. Galione, *Two neuropeptides recruit different messenger pathways to evoke Ca2+ signals in the same cell.* Curr Biol, 2000. **10**(16): p. 993-6.
112. Pandey, V., et al., *Recruitment of NAADP-sensitive acidic Ca2+ stores by glutamate.* Biochem J, 2009. **422**(3): p. 503-12.
113. Brailoiu, G.C., et al., *Acidic NAADP-sensitive calcium stores in the endothelium: agonist-specific recruitment and role in regulating blood pressure.* J Biol Chem, 2010. **285**(48): p. 37133-7.
114. Esposito, B., et al., *NAADP links histamine H1 receptors to secretion of von Willebrand factor in human endothelial cells.* Blood, 2011. **117**(18): p. 4968-77.

115. Lewis, A.M., et al., *Refinement of a radioreceptor binding assay for nicotinic acid adenine dinucleotide phosphate.* Anal Biochem, 2007. **371**(1): p. 26-36.
116. Graeff, R. and H.C. Lee, *A novel cycling assay for nicotinic acid-adenine dinucleotide phosphate with nanomolar sensitivity.* Biochem J, 2002. **367**(Pt 1): p. 163-8.
117. Churchill, G.C., et al., *Sperm deliver a new second messenger: NAADP.* Curr Biol, 2003. **13**(2): p. 125-8.
118. Vasudevan, S.R., et al., *The calcium-mobilizing messenger nicotinic acid adenine dinucleotide phosphate participates in sperm activation by mediating the acrosome reaction.* J Biol Chem, 2010. **285**(24): p. 18262-9.
119. Walseth, T.F., et al., *Photoaffinity labeling of high affinity nicotinic acid adenine dinucleotide phosphate (NAADP)-binding proteins in sea urchin egg.* J Biol Chem, 2012. **287**(4): p. 2308-15.
120. Christensen, K.A., J.T. Myers, and J.A. Swanson, *pH-dependent regulation of lysosomal calcium in macrophages.* J Cell Sci, 2002. **115**(Pt 3): p. 599-607.
121. Lloyd-Evans, E., et al., *Niemann-Pick disease type C1 is a sphingosine storage disease that causes deregulation of lysosomal calcium.* Nat Med, 2008. **14**(11): p. 1247-55.
122. Kilpatrick, B.S., et al., *Direct mobilisation of lysosomal Ca2+ triggers complex Ca2+ signals.* J Cell Sci, 2013. **126**(Pt 1): p. 60-6.
123. Morgan, A.J. and A. Galione, *NAADP induces pH changes in the lumen of acidic Ca2+ stores.* Biochem J, 2007. **402**(2): p. 301-10.
124. Morgan, A.J., et al., *Molecular mechanisms of endolysosomal Ca2+ signalling in health and disease.* Biochem J, 2011. **439**(3): p. 349-74.
125. Shigaki, T., et al., *Identification of three distinct phylogenetic groups of CAX cation/proton antiporters.* J Mol Evol, 2006. **63**(6): p. 815-25.
126. Pittman, J.K., *Vacuolar Ca(2+) uptake.* Cell Calcium, 2011. **50**(2): p. 139-46.
127. Ishibashi, K., M. Suzuki, and M. Imai, *Molecular cloning of a novel form (two-repeat) protein related to voltage-gated sodium and calcium channels.* Biochem Biophys Res Commun, 2000. **270**(2): p. 370-6.
128. Yu, F.H. and W.A. Catterall, *The VGL-chanome: a protein superfamily specialized for electrical signaling and ionic homeostasis.* Sci STKE, 2004. **2004**(253): p. re15.
129. Brailoiu, E., et al., *An ancestral deuterostome family of two-pore channels mediates nicotinic acid adenine dinucleotide phosphate-dependent calcium release from acidic organelles.* J Biol Chem, 2010. **285**(5): p. 2897-901.
130. Zhu, M.X., et al., *TPCs: Endolysosomal channels for Ca2+ mobilization from acidic organelles triggered by NAADP.* FEBS Lett, 2010. **584**(10): p. 1966-74.
131. Hedrich, R. and I. Marten, *TPC1-SV channels gain shape.* Mol Plant, 2011. **4**(3): p. 428-41.
132. Zong, X., et al., *The two-pore channel TPCN2 mediates NAADP-dependent Ca(2+)-release from lysosomal stores.* Pflugers Arch, 2009. **458**(5): p. 891-9.
133. Ruas, M., et al., *TPC1 has two variant isoforms, and their removal has different effects on endo-lysosomal functions compared to loss of TPC2.* Mol Cell Biol, 2014. **34**(21): p. 3981-92.
134. Cole, C., J.D. Barber, and G.J. Barton, *The Jpred 3 secondary structure prediction server.* Nucleic Acids Res, 2008. **36**(Web Server issue): p. W197-201.

135. Brohawn, S.G., J. del Marmol, and R. MacKinnon, *Crystal structure of the human K2P TRAAK, a lipid- and mechano-sensitive K+ ion channel.* Science, 2012. **335**(6067): p. 436-41.
136. Miller, A.N. and S.B. Long, *Crystal structure of the human two-pore domain potassium channel K2P1.* Science, 2012. **335**(6067): p. 432-6.
137. Nishida, M. and R. MacKinnon, *Structural basis of inward rectification: cytoplasmic pore of the G protein-gated inward rectifier GIRK1 at 1.8 A resolution.* Cell, 2002. **111**(7): p. 957-65.
138. Kuo, A., et al., *Crystal structure of the potassium channel KirBac1.1 in the closed state.* Science, 2003. **300**(5627): p. 1922-6.
139. Pegan, S., et al., *Cytoplasmic domain structures of Kir2.1 and Kir3.1 show sites for modulating gating and rectification.* Nat Neurosci, 2005. **8**(3): p. 279-87.
140. Whorton, M.R. and R. MacKinnon, *X-ray structure of the mammalian GIRK2-betagamma G-protein complex.* Nature, 2013. **498**(7453): p. 190-7.
141. Churamani, D., et al., *Domain assembly of NAADP-gated two-pore channels.* Biochem J, 2012. **441**(1): p. 317-23.
142. Doyle, D.A., et al., *The structure of the potassium channel: molecular basis of K+ conduction and selectivity.* Science, 1998. **280**(5360): p. 69-77.
143. Jiang, Y., et al., *Crystal structure and mechanism of a calcium-gated potassium channel.* Nature, 2002. **417**(6888): p. 515-22.
144. Long, S.B., E.B. Campbell, and R. Mackinnon, *Crystal structure of a mammalian voltage-dependent Shaker family K+ channel.* Science, 2005. **309**(5736): p. 897-903.
145. Shi, N., et al., *Atomic structure of a Na+- and K+-conducting channel.* Nature, 2006. **440**(7083): p. 570-4.
146. Tao, X., et al., *Crystal structure of the eukaryotic strong inward-rectifier K+ channel Kir2.2 at 3.1 A resolution.* Science, 2009. **326**(5960): p. 1668-74.
147. Payandeh, J., et al., *The crystal structure of a voltage-gated sodium channel.* Nature, 2011. **475**(7356): p. 353-8.
148. Zhang, X., et al., *Crystal structure of an orthologue of the NaChBac voltage-gated sodium channel.* Nature, 2012. **486**(7401): p. 130-4.
149. Rietdorf, K., et al., *Two-pore channels form homo- and heterodimers.* J Biol Chem, 2011. **286**(43): p. 37058-62.
150. Boumechache, M., et al., *Analysis of assembly and trafficking of native P2X4 and P2X7 receptor complexes in rodent immune cells.* J Biol Chem, 2009. **284**(20): p. 13446-54.
151. Guo, C., et al., *Evidence for functional P2X4/P2X7 heteromeric receptors.* Mol Pharmacol, 2007. **72**(6): p. 1447-56.
152. Brailoiu, E., et al., *An NAADP-gated two-pore channel targeted to the plasma membrane uncouples triggering from amplifying Ca2+ signals.* J Biol Chem, 2010. **285**(49): p. 38511-6.
153. Kelly, B.T., et al., *A structural explanation for the binding of endocytic dileucine motifs by the AP2 complex.* Nature, 2008. **456**(7224): p. 976-79.
154. Ruas, M., et al., *Purified TPC isoforms form NAADP receptors with distinct roles for Ca(2+) signaling and endolysosomal trafficking.* Curr Biol, 2010. **20**(8): p. 703-9.

155. Cang, C., K. Aranda, and D. Ren, *A non-inactivating high-voltage-activated two-pore Na(+) channel that supports ultra-long action potentials and membrane bistability.* Nat Commun, 2014. **5**: p. 5015.
156. Cang, C., B. Bekele, and D. Ren, *The voltage-gated sodium channel TPC1 confers endolysosomal excitability.* Nat Chem Biol, 2014. **10**(6): p. 463-9.
157. Wang, X., et al., *TPC proteins are phosphoinositide- activated sodium-selective ion channels in endosomes and lysosomes.* Cell, 2012. **151**(2): p. 372-83.
158. Cang, C., et al., *mTOR regulates lysosomal ATP-sensitive two-pore Na(+) channels to adapt to metabolic state.* Cell, 2013. **152**(4): p. 778-90.
159. Jha, A., et al., *Convergent regulation of the lysosomal two-pore channel-2 by Mg(2)(+), NAADP, PI(3,5)P(2) and multiple protein kinases.* EMBO J, 2014. **33**(5): p. 501-11.
160. Boccaccio, A., et al., *The phosphoinositide PI(3,5)P(2) mediates activation of mammalian but not plant TPC proteins: functional expression of endolysosomal channels in yeast and plant cells.* Cell Mol Life Sci, 2014. **71**(21): p. 4275-83.
161. Rybalchenko, V., et al., *Membrane potential regulates nicotinic acid adenine dinucleotide phosphate (NAADP) dependence of the pH- and Ca2+-sensitive organellar two-pore channel TPC1.* J Biol Chem, 2012. **287**(24): p. 20407-16.
162. Pitt, S.J., et al., *Reconstituted human TPC1 is a proton-permeable ion channel and is activated by NAADP or Ca2+.* Sci Signal, 2014. **7**(326): p. ra46.
163. Schieder, M., et al., *Characterization of two-pore channel 2 (TPCN2)-mediated Ca2+ currents in isolated lysosomes.* J Biol Chem, 2010. **285**(28): p. 21219-22.
164. Pitt, S.J., et al., *TPC2 is a novel NAADP-sensitive Ca2+ release channel, operating as a dual sensor of luminal pH and Ca2+.* J Biol Chem, 2010. **285**(45): p. 35039-46.
165. Yamaguchi, S., et al., *Transient receptor potential mucolipin 1 (TRPML1) and two-pore channels are functionally independent organellar ion channels.* J Biol Chem, 2011. **286**(26): p. 22934-42.
166. Lu, Y., et al., *Two pore channel 2 (TPC2) inhibits autophagosomal-lysosomal fusion by alkalinizing lysosomal pH.* J Biol Chem, 2013. **288**(33): p. 24247-63.
167. Zhang, Z.H., Y.Y. Lu, and J. Yue, *Two pore channel 2 differentially modulates neural differentiation of mouse embryonic stem cells.* PLoS One, 2013. **8**(6): p. e66077.
168. Lin-Moshier, Y., et al., *The Two-pore channel (TPC) interactome unmasks isoform-specific roles for TPCs in endolysosomal morphology and cell pigmentation.* Proc Natl Acad Sci U S A, 2014. **111**(36): p. 13087-92.
169. Sancak, Y., et al., *Ragulator-Rag complex targets mTORC1 to the lysosomal surface and is necessary for its activation by amino acids.* Cell, 2010. **141**(2): p. 290-303.
170. Gomez-Suaga, P., et al., *A link between LRRK2, autophagy and NAADP-mediated endolysosomal calcium signalling.* Biochem Soc Trans, 2012. **40**(5): p. 1140-6.
171. Grimm, C., et al., *High susceptibility to fatty liver disease in two-pore channel 2-deficient mice.* Nat Commun, 2014. **5**: p. 4699.
172. Lam, A.K., et al., *Hax-1 identified as a two-pore channel (TPC)-binding protein.* FEBS Lett, 2013. **587**(23): p. 3782-6.
173. Steinberg, B.E., et al., *A cation counterflux supports lysosomal acidification.* J Cell Biol, 2010. **189**(7): p. 1171-86.
174. Hockey, L.N., et al., *Dysregulation of lysosomal morphology by pathogenic LRRK2 is corrected by TPC2 inhibition.* J Cell Sci, 2015. **128**(2): p. 232-8.

175. Pereira, G.J., et al., *Nicotinic acid adenine dinucleotide phosphate (NAADP) regulates autophagy in cultured astrocytes.* J Biol Chem, 2011. **286**(32): p. 27875-81.
176. Ogunbayo, O.A., et al., *Cyclic adenosine diphosphate ribose activates ryanodine receptors, whereas NAADP activates two-pore domain channels.* J Biol Chem, 2011. **286**(11): p. 9136-40.
177. Hille, B., *Ion channels of excitable membranes*. 3rd ed. 2001, Sunderland, Mass.: Sinauer. xviii, 814 p., 8 p. of plates.
178. Jha, A., E. Brailoiu, and S. Muallem, *How does NAADP release lysosomal Ca2+?* Channels (Austin), 2014. **8**(3): p. 174-5.
179. Marchant, J.S. and S. Patel, *Questioning regulation of two-pore channels by NAADP.* Messenger (Los Angel), 2013. **2**(2): p. 113-119.
180. Morgan, A.J. and A. Galione, *Two-pore channels (TPCs): current controversies.* Bioessays, 2014. **36**(2): p. 173-83.
181. Burnashev, N., et al., *Fractional calcium currents through recombinant GluR channels of the NMDA, AMPA and kainate receptor subtypes.* J Physiol, 1995. **485 (Pt 2)**: p. 403-18.
182. Zheng, L., U. Baumann, and J.L. Reymond, *An efficient one-step site-directed and site-saturation mutagenesis protocol.* Nucleic Acids Res, 2004. **32**(14): p. e115.
183. Hamill, O.P., et al., *Improved patch-clamp techniques for high-resolution current recording from cells and cell-free membrane patches.* Pflugers Arch, 1981. **391**(2): p. 85-100.
184. Neher, E., *Correction for liquid junction potentials in patch clamp experiments.* Methods Enzymol, 1992. **207**: p. 123-31.
185. Alvarez, O., C. Gonzalez, and R. Latorre, *Counting channels: a tutorial guide on ion channel fluctuation analysis.* Adv Physiol Educ, 2002. **26**(1-4): p. 327-41.
186. Ogden, D. and Company of Biologists., *Microelectrode techniques : the Plymouth Workshop handbook*. 2nd ed ed. 1994, Cambridge: Company of Biologists. x, 448 p.
187. Schneggenburger, R., et al., *Fractional contribution of calcium to the cation current through glutamate receptor channels.* Neuron, 1993. **11**(1): p. 133-43.
188. Neher, E. and G.J. Augustine, *Calcium gradients and buffers in bovine chromaffin cells.* J Physiol, 1992. **450**: p. 273-301.
189. Helmchen, F., K. Imoto, and B. Sakmann, *Ca2+ buffering and action potential-evoked Ca2+ signaling in dendrites of pyramidal neurons.* Biophys J, 1996. **70**(2): p. 1069-81.
190. Smith, G.D., *Analytical steady-state solution to the rapid buffering approximation near an open Ca2+ channel.* Biophys J, 1996. **71**(6): p. 3064-72.
191. Neher, E., *Usefulness and limitations of linear approximations to the understanding of Ca++ signals.* Cell Calcium, 1998. **24**(5-6): p. 345-57.
192. Dingledine, R., et al., *The glutamate receptor ion channels.* Pharmacol Rev, 1999. **51**(1): p. 7-61.
193. Schwartz, R., *Biological modeling and simulation : a survey of practical models, algorithms, and numerical methods*. Computational molecular biology. 2008, Cambridge, Mass.: MIT Press. xii, 389 p.
194. Pusch, M. and E. Neher, *Rates of diffusional exchange between small cells and a measuring patch pipette.* Pflugers Arch, 1988. **411**(2): p. 204-11.
195. Boittin, F.X., A. Galione, and A.M. Evans, *Nicotinic acid adenine dinucleotide phosphate mediates Ca2+ signals and contraction in arterial smooth muscle via a two-pool mechanism.* Circ Res, 2002. **91**(12): p. 1168-75.

196. Kinnear, N.P., et al., *Lysosomes co-localize with ryanodine receptor subtype 3 to form a trigger zone for calcium signalling by NAADP in rat pulmonary arterial smooth muscle.* Cell Calcium, 2008. **44**(2): p. 190-201.
197. Ruas, M., et al., *Expression of Ca2+-permeable two-pore channels rescues NAADP signalling in TPC-deficient cells.* EMBO J, 2015.
198. Sugita, S., et al., *Synaptotagmins form a hierarchy of exocytotic Ca(2+) sensors with distinct Ca(2+) affinities.* EMBO J, 2002. **21**(3): p. 270-80.
199. Zhang, X., C.R. Solaro, and C.J. Lingle, *Allosteric regulation of BK channel gating by Ca(2+) and Mg(2+) through a nonselective, low affinity divalent cation site.* J Gen Physiol, 2001. **118**(5): p. 607-36.
200. Saucerman, J.J. and D.M. Bers, *Calmodulin binding proteins provide domains of local Ca2+ signaling in cardiac myocytes.* J Mol Cell Cardiol, 2012. **52**(2): p. 312-6.
201. Eisenman, G. and R. Horn, *Ionic selectivity revisited: the role of kinetic and equilibrium processes in ion permeation through channels.* J Membr Biol, 1983. **76**(3): p. 197-225.
202. Lipkind, G.M. and H.A. Fozzard, *Voltage-gated Na channel selectivity: the role of the conserved domain III lysine residue.* J Gen Physiol, 2008. **131**(6): p. 523-9.
203. van Meer, G., D.R. Voelker, and G.W. Feigenson, *Membrane lipids: where they are and how they behave.* Nat Rev Mol Cell Biol, 2008. **9**(2): p. 112-24.
204. Behnia, R. and S. Munro, *Organelle identity and the signposts for membrane traffic.* Nature, 2005. **438**(7068): p. 597-604.
205. Cui, J., H. Yang, and U.S. Lee, *Molecular mechanisms of BK channel activation.* Cell Mol Life Sci, 2009. **66**(5): p. 852-75.
206. Eswar, N., et al., *Comparative protein structure modeling using MODELLER.* Curr Protoc Protein Sci, 2007. **Chapter 2**: p. Unit 2 9.
207. Bagneris, C., et al., *Role of the C-terminal domain in the structure and function of tetrameric sodium channels.* Nat Commun, 2013. **4**: p. 2465.
208. Humphrey, W., A. Dalke, and K. Schulten, *VMD: visual molecular dynamics.* J Mol Graph, 1996. **14**(1): p. 33-8, 27-8.
209. Phillips, J.C., et al., *Scalable molecular dynamics with NAMD.* J Comput Chem, 2005. **26**(16): p. 1781-802.
210. MacKerell, A.D., et al., *All-atom empirical potential for molecular modeling and dynamics studies of proteins.* J Phys Chem B, 1998. **102**(18): p. 3586-616.
211. Trott, O. and A.J. Olson, *AutoDock Vina: improving the speed and accuracy of docking with a new scoring function, efficient optimization, and multithreading.* J Comput Chem, 2010. **31**(2): p. 455-61.
212. Jackson, M.B., *Molecular and cellular biophysics*. 2006, Cambridge: Cambridge University Press. xiii, 512 p.
213. Jiang, Y., et al., *The open pore conformation of potassium channels.* Nature, 2002. **417**(6888): p. 523-6.
214. Jogini, V. and B. Roux, *Electrostatics of the intracellular vestibule of K+ channels.* J Mol Biol, 2005. **354**(2): p. 272-88.
215. Berneche, S. and B. Roux, *A microscopic view of ion conduction through the K+ channel.* Proc Natl Acad Sci U S A, 2003. **100**(15): p. 8644-8.
216. Roux, B., S. Berneche, and W. Im, *Ion channels, permeation, and electrostatics: insight into the function of KcsA.* Biochemistry, 2000. **39**(44): p. 13295-306.

217. Contreras, J.E., et al., *Voltage profile along the permeation pathway of an open channel.* Biophys J, 2010. **99**(9): p. 2863-9.
218. Woodhull, A.M., *Ionic blockage of sodium channels in nerve.* J Gen Physiol, 1973. **61**(6): p. 687-708.
219. Spassova, M. and Z. Lu, *Tuning the voltage dependence of tetraethylammonium block with permeant ions in an inward-rectifier K+ channel.* J Gen Physiol, 1999. **114**(3): p. 415-26.
220. Spassova, M. and Z. Lu, *Coupled ion movement underlies rectification in an inward-rectifier K+ channel.* J Gen Physiol, 1998. **112**(2): p. 211-21.
221. Lu, Z. and R. MacKinnon, *Electrostatic tuning of Mg2+ affinity in an inward-rectifier K+ channel.* Nature, 1994. **371**(6494): p. 243-6.
222. Yang, L., J. Edvinsson, and L.G. Palmer, *Interactions of external K+ and internal blockers in a weak inward-rectifier K+ channel.* J Gen Physiol, 2012. **140**(5): p. 529-40.
223. Yang, L., G. Frindt, and L.G. Palmer, *Magnesium modulates ROMK channel-mediated potassium secretion.* J Am Soc Nephrol, 2010. **21**(12): p. 2109-16.
224. Lockless, S.W., M. Zhou, and R. MacKinnon, *Structural and thermodynamic properties of selective ion binding in a K+ channel.* PLoS Biol, 2007. **5**(5): p. e121.
225. Liu, S., X. Bian, and S.W. Lockless, *Preferential binding of K+ ions in the selectivity filter at equilibrium explains high selectivity of K+ channels.* J Gen Physiol, 2012. **140**(6): p. 671-9.
226. Liu, S. and S.W. Lockless, *Equilibrium selectivity alone does not create K+-selective ion conduction in K+ channels.* Nat Commun, 2013. **4**: p. 2746.
227. Picollo, A., et al., *Synergistic substrate binding determines the stoichiometry of transport of a prokaryotic H(+)/Cl(-) exchanger.* Nat Struct Mol Biol, 2012. **19**(5): p. 525-31, S1.
228. Picollo, A., et al., *Basis of substrate binding and conservation of selectivity in the CLC family of channels and transporters.* Nat Struct Mol Biol, 2009. **16**(12): p. 1294-301.
229. Neyton, J. and C. Miller, *Potassium blocks barium permeation through a calcium-activated potassium channel.* J Gen Physiol, 1988. **92**(5): p. 549-67.
230. Neyton, J. and C. Miller, *Discrete Ba2+ block as a probe of ion occupancy and pore structure in the high-conductance Ca2+ -activated K+ channel.* J Gen Physiol, 1988. **92**(5): p. 569-86.
231. Piasta, K.N., D.L. Theobald, and C. Miller, *Potassium-selective block of barium permeation through single KcsA channels.* J Gen Physiol, 2011. **138**(4): p. 421-36.
232. Payandeh, J., et al., *Crystal structure of a voltage-gated sodium channel in two potentially inactivated states.* Nature, 2012. **486**(7401): p. 135-9.
233. Boiteux, C., I. Vorobyov, and T.W. Allen, *Ion conduction and conformational flexibility of a bacterial voltage-gated sodium channel.* Proc Natl Acad Sci U S A, 2014. **111**(9): p. 3454-9.
234. Stock, L., et al., *Conduction in a biological sodium selective channel.* J Phys Chem B, 2013. **117**(14): p. 3782-9.
235. Furini, S. and C. Domene, *On conduction in a bacterial sodium channel.* PLoS Comput Biol, 2012. **8**(4): p. e1002476.
236. Corry, B. and M. Thomas, *Mechanism of ion permeation and selectivity in a voltage gated sodium channel.* J Am Chem Soc, 2012. **134**(3): p. 1840-6.
237. Chakrabarti, N., et al., *Catalysis of Na+ permeation in the bacterial sodium channel Na(V)Ab.* Proc Natl Acad Sci U S A, 2013. **110**(28): p. 11331-6.

238. Furini, S., P. Barbini, and C. Domene, *Effects of the protonation state of the EEEE motif of a bacterial Na(+)-channel on conduction and pore structure.* Biophys J, 2014. **106**(10): p. 2175-83.
239. Qiu, H., R. Shen, and W. Guo, *Ion solvation and structural stability in a sodium channel investigated by molecular dynamics calculations.* Biochim Biophys Acta, 2012. **1818**(11): p. 2529-35.
240. Ke, S., E.M. Zangerl, and A. Stary-Weinzinger, *Distinct interactions of Na+ and Ca2+ ions with the selectivity filter of the bacterial sodium channel Na(V)Ab.* Biochem Biophys Res Commun, 2013. **430**(4): p. 1272-6.
241. Kulleperuma, K., et al., *Construction and validation of a homology model of the human voltage-gated proton channel hHV1.* J Gen Physiol, 2013. **141**(4): p. 445-65.